

4

DNA-TR-88-44

HIGH-LATITUDE F-REGION IRREGULARITIES

A Review and Synthesis

R. T. Tsunoda
SRI International
333 Ravenswood Avenue
Menlo Park, CA 94025-3434

15 February 1988

Technical Report

CONTRACT No. DNA 001-86-C-0002

Approved for public release;
distribution is unlimited.

THIS WORK WAS SPONSORED BY THE DEFENSE NUCLEAR AGENCY
UNDER RDT&E RMC CODE B3220854693 RB RX 00002 25904D.

DTIC
SEP 19 1988
H

Prepared for
Director
DEFENSE NUCLEAR AGENCY
Washington, DC 20305-1000

AD-A197 698

DISTRIBUTION LIST UPDATE

This mailer is provided to enable DNA to maintain current distribution lists for reports. We would appreciate your providing the requested information.

- Add the individual listed to your distribution list.
- Delete the cited organization./individual.
- Change of address.

NAME:

ORGANIZATION:

OLD ADDRESS

CURRENT ADDRESS

TELEPHONE NUMBER: ()

SUBJECT AREA(S) OF INTEREST:

DNA OR OTHER GOVERNMENT CONTRACT NUMBER:

CERTIFICATION OF NEED TO KNOW BY GOVERNMENT SPONSOR (if other than DNA)

SPONSORING ORGANIZATION

CONTRACTING OFFICER OR REPRESENTATIVE

SIGNATURE

CUT HERE AND RETURN



Director
Defense Nuclear Agency
ATTN: TITL
Washington, DC 20305 1000

Director
Defense Nuclear Agency
ATTN: TITL
Washington, DC 20305 1000

UNCLASSIFIED

SECURITY CLASSIFICATION OF THIS PAGE

REPORT DOCUMENTATION PAGE

1a. REPORT SECURITY CLASSIFICATION UNCLASSIFIED			1b. RESTRICTIVE MARKINGS	
2a. SECURITY CLASSIFICATION AUTHORITY N/A since Unclassified			3. DISTRIBUTION/AVAILABILITY OF REPORT Approved for public release; distribution is unlimited.	
2b. DECLASSIFICATION/DOWNGRADING SCHEDULE N/A since Unclassified				
4. PERFORMING ORGANIZATION REPORT NUMBER(S) SRI Project 1700			5. MONITORING ORGANIZATION REPORT NUMBER(S) DNA-TR-88-44	
6a. NAME OF PERFORMING ORGANIZATION SRI International		6b. OFFICE SYMBOL (if applicable)	7a. NAME OF MONITORING ORGANIZATION Director Defense Nuclear Agency	
6c. ADDRESS (City, State, and ZIP Code) 333 Ravenswood Avenue Menlo Park, California 94025-3434			7b. ADDRESS (City, State, and ZIP Code) Washington, DC 20305-1000	
8a. NAME OF FUNDING/SPONSORING ORGANIZATION		8b. OFFICE SYMBOL (if applicable) RAAE/Wittwer	9. PROCUREMENT INSTRUMENT IDENTIFICATION NUMBER DNA 001-86-C-0002	
8c. ADDRESS (City, State, and ZIP Code)			10. SOURCE OF FUNDING NUMBERS	
			PROGRAM ELEMENT NO. 62715H	PROJECT NO. RB
11. TITLE (Include Security Classification) HIGH-LATITUDE F-REGION IRREGULARITIES A Review and Synthesis				
12. PERSONAL AUTHOR(S) Tsunoda, Roland T.				
13a. TYPE OF REPORT Technical		13b. TIME COVERED FROM 860101 TO 870701		14. DATE OF REPORT (Year, Month, Day) 880215
15. PAGE COUNT 880215				
16. SUPPLEMENTARY NOTATION This work was sponsored by the Defense Nuclear Agency under RDT&E RMC Code B3220854693 RB RX 00002 25904D.				
17. COSATI CODES			18. SUBJECT TERMS (Continue on reverse if necessary and identify by block number)	
FIELD	GROUP	SUB-GROUP		
17	02	1	Irregularities E x B instability	
20	09		Polar F layer Gradient-drift instability	
19. ABSTRACT (Continue on reverse if necessary and identify by block number)				
<p>The most intense, F-region irregularities in the high-latitude ionosphere appear to be produced by convective plasma processes, and in particular, the fluid $E \times B$ (gradient-drift) interchange instability. Irregularities are produced by convectively mixing plasma across a mean plasma-density gradient. The transport of higher-density plasma into regions of lower-density plasma (and vice versa) leads to the development of an irregularity spectrum that extends in scale from about 10 km down to the ion gyroradius. Because irregularities with this range of scales are not independent from larger-scale plasma structures that are produced by other means, we review the characteristics and processes of > 10 km plasma structure and relate them to those of smaller-scale irregularities. From this review, we synthesize a descriptive model of plasma structures in the high-latitude F layer</p>				
20. DISTRIBUTION/AVAILABILITY OF ABSTRACT <input type="checkbox"/> UNCLASSIFIED/UNLIMITED <input checked="" type="checkbox"/> SAME AS RPT. <input type="checkbox"/> DTIC USERS			21. ABSTRACT SECURITY CLASSIFICATION UNCLASSIFIED	
22a. NAME OF RESPONSIBLE INDIVIDUAL Sandra E. Young			22b. TELEPHONE (Include Area Code) (202) 325-7042	22c. OFFICE SYMBOL DNA/CSTI

UNCLASSIFIED

SECURITY CLASSIFICATION OF THIS PAGE (When Data Entered)

19. ABSTRACT (Continued)

that unifies most of the diverse and independent observations. For the large-scale plasma processes, the model includes (1) the formation of 1000-km-scale "patches" in the polar cap from solar-produced plasma that is transported poleward from lower latitudes; (2) the reconfiguration of patches as they convect into the auroral region and become the latitudinally confined but longitudinally extended, plasma-density enhancements near the equatorward auroral boundary; and (3) the production of localized enhancements and depletions along the poleward auroral boundary by soft-particle precipitation and large but localized electric fields. In the model, the most intense, smaller-scale irregularities are in spatial proximity to these large-scale plasma features, the implication being that the presence of the latter allows formation of the former. The irregularity characteristics are consistent with production by the $\underline{E} \times \underline{B}$ instability and a morphology controlled by (1) a "slip" velocity (i.e., ion drift relative to the neutral gas) that is moderately small except in regions of nonuniform plasma convection or under time-varying conditions (e.g., substorms, pulsation events), and (2) a highly conducting auroral E layer that damps irregularity growth and enhances decay. The final irregularity spectrum appears to be produced by (1) global convective processes acting on solar-produced plasma at the largest scales (> 50 km), (2) particle precipitation at scales greater than 10 km, (3) perhaps some form of wave activity around 10 km, and (4) the $\underline{E} \times \underline{B}$ instability at the smaller scales (< 10 km).

Accession For	
NTIS	<input checked="" type="checkbox"/>
DTIC TAB	<input type="checkbox"/>
Unannounced	<input type="checkbox"/>
Justification	
By	
Distribution/	
Availability Codes	
Avail and/or	
Dist	
A-1	

2
1000
1000

UNCLASSIFIED

SECURITY CLASSIFICATION OF THIS PAGE (When Data Entered)

EXECUTIVE SUMMARY

The topic of high-latitude F-region irregularities is of considerable interest to the Defense Nuclear Agency (DNA). Geographically, the polar ionosphere occupies a large percentage of the strategically critical area between the Soviet Union and the United States. If only for this reason, we must understand the nature and characteristics of high-latitude ionospheric irregularities because they impact the success of strategic defense systems. Moreover, the dominant source mechanism for high-latitude F-region irregularities appears to be the $\underline{E} \times \underline{B}$ (gradient-drift) instability, the same plasma process that produces F-region structure in the late-time nuclear environment. The polar ionosphere therefore provides another natural testbed, together with barium ion clouds and the nighttime equatorial ionosphere, which can be used in the absence of above ground nuclear tests, to improve our understanding of this ubiquitous instability process. The high-latitude ionosphere is of further interest because it involves physical processes that are not well understood and sources of free energy not found at lower latitudes that may couple into nuclear plumes. Such coupling is not considered in present nuclear predictive codes.

Surprisingly little is known about high-latitude F-region irregularities despite research that has spanned several decades. A major obstacle to progress has been the fact that irregularity measurements made locally at a given time cannot be simply interpreted in terms of background conditions that prevailed during and in the vicinity of those measurements. The irregularities of interest here, those with spatial scales greater than a few hundred meters, have long lifetimes and hence are convectively transported over great distances by large electric fields in the polar ionosphere. Consequently, their characteristics are molded by effects accumulated during their journey from origin to point of measurement. Because of this difficulty, results from past analyses of data must be questioned with regard to the identified irregularity source mechanisms if any, and the interpretation of irregularity characteristics.

Given the DNA relevance of high-latitude F-region irregularities and the question raised regarding correct interpretation of past results, it seems a propitious time to review and reinterpret past measurements from our present perspective and understanding. This report does not simply reinterpret past measurements in isolation; the intent instead is to synthesize a descriptive working model from all available measurements. By using this approach, it becomes possible to evaluate the importance of various physical parameters that may contribute to irregularity growth and decay. The resultant descriptive model represents our working knowledge of processes associated with high-latitude F-region irregularities and provides a unified framework from which new theories can be formulated and critical experiments can be designed and conducted. The need for such a model is evidenced by (1) the existence of numerous theories that attempt to model the various competing processes that might influence the behavior of the $\underline{E} \times \underline{B}$ instability, and (2) the glaring absence of experimental verification of those models.

Herein, we demonstrate the existence of a close relationship between gradients associated with large-scale ($> 10k$ km) irregularities of interest to DNA. The results of this review strongly support the hypothesis that the $\underline{E} \times \underline{B}$ instability plays a dominant role in controlling the spectral characteristics of irregularities with spatial scales less than a few kilometers. (The evidence also indicates the relative unimportance of other mechanisms, e.g., the current-convective instability.) At the same time, we have found that processes other than the $\underline{E} \times \underline{B}$ instability are responsible for the large-scale structures and that the characteristics at larger spectral scales cannot be interpreted solely in terms of the interchange process. These results imply that an experimental estimate of an outer scale associated with the $\underline{E} \times \underline{B}$ instability, if larger than a few kilometers, is not determinable from measurements in the polar ionosphere where particle precipitation and wave activity contribute substantially to irregularity strength at those scales.

The morphologies of large-scale structures and smaller-scale irregularities in the polar F layer are constructed and compared for the first time in this report. Although still rudimentary, the morphologies are described in relation to auroral boundaries and streamlines of convective flow rather than in terms of latitude and local time. By doing so, this phenomenological construction can be used (1) to understand the underlying physical processes that produce the large-scale structure, and (2) to predict the distribution of the most intense irregularities which can differ significantly from the statistical average during the course of a polar disturbance, e.g., a substorm. A physical model of this kind is more amenable to continued improvements in predictive capability than those based on statistical averages.

The prototype working model described in this report also includes the first realistic estimates of the principal parameters controlling the $\underline{E} \times \underline{B}$ instability in the polar ionosphere, namely the "slip" velocity and the M factor. The slip velocity (the difference velocity between ions and neutrals) in the auroral ionosphere is shown to be small in comparison to the electron drift velocity (that is often assumed to be identical to the slip velocity). This analysis also points out the need to consider time constants of ion-drag forces so that the space and time variations of the slip velocity can be realistically modeled. These variations must also be compared to time scales of auroral events, e.g., substorms and pulsations.

The M factor (defined in the report) is a measure of the polarizability of F-region plasma structure. The M factor directly affects the $\underline{E} \times \underline{B}$ instability through polarization shorting effects. Because it suppresses irregularity growth and enhances irregularity decay, plasma structures can usefully be classified in terms of the M factor. For example, "patches" in the polar cap are high-M plasma clouds but become low-M clouds upon entering the midnight auroral oval where the background E-region Pedersen conductance is high. After convecting through the auroral zone, they can once again become high-M clouds if they enter subauroral regions. The morphology of the M factor together with that

for the slip velocity therefore provides a realistic description of the effective driver strength. Conducting experiments in these various locales and campaign results allows the M dependence of DNA structure codes to be tested experimentally.

The results derived from this review and synthesis provides a unified framework from which reasonable theoretical models can be constructed. We now have some idea of realistic plasma geometries and driver strengths. We are also aware of their proximity to auroral boundaries where other processes such as velocity shear must be considered. Much more, however, remains to be done. Topics such as scale-size-dependent mapping of the electric potential mapping and the phenomenon of "freezing" have only been briefly considered. Inclusion of these and other processes into the descriptive working model remains as a future effort.

PREFACE

Preparation of this review was supported by DNA Contract DNA001-86-C-0002. The author thanks L. Wittwer for reading the original manuscript and providing insightful comments that have significantly improved both content and presentation. The author also thanks O. de la Beaujardiere, R. C. Livingston, C. L. Rino, R. M. Robinson, J. F. Vickrey, J.-P. Villain, E. J. Weber, V. B. Wickwar, and S. T. Zalesak for helpful discussions.

CONVERSION TABLE

Conversion factors for U.S. Customary to metric (SI) units of measurement

MULTIPLY \longrightarrow BY \longrightarrow TO GET
TO GET \longleftarrow BY \longleftarrow DIVIDE

angstrom	$1.000000 \times E - 10$	meters (m)
atmosphere (normal)	$1.01325 \times E + 2$	kilo pascal (kPa)
bar	$1.000000 \times E + 2$	kilo pascal (kPa)
barn	$1.000000 \times E - 28$	meter ² (m ²)
British thermal unit (thermochemical)	$1.054350 \times E + 3$	joule (J)
calorie (thermochemical)	4.184000	joule (J)
cal (thermochemical) / cm ²	$4.184000 \times E - 2$	mega joule/m ² (MJ/m ²)
curie	$3.700000 \times E + 1$	*giga becquerel (GBq)
degree (angle)	$1.745329 \times E - 2$	radian (rad)
degree Fahrenheit	$t_K \approx (t_F + 459.67)/1.8$	degree kelvin (K)
electron volt	$1.60219 \times E - 19$	joule (J)
erg	$1.000000 \times E - 7$	joule (J)
erg/second	$1.000000 \times E - 7$	watt (W)
foot	$3.048000 \times E - 1$	meter (m)
foot-pound-force	1.355818	joule (J)
gallon (U.S. liquid)	$3.785412 \times E - 3$	meter ³ (m ³)
inch	$2.540000 \times E - 2$	meter (m)
jerk	$1.000000 \times E + 9$	joule (J)
joule/kilogram (J/kg) (radiation dose absorbed)	1.000000	Gray (Gy)
kilotons	4.183	terajoules
kip (1000 lbf)	$4.448222 \times E + 3$	newton (N)
kip/inch ² (ksi)	$6.894757 \times E + 3$	kilo pascal (kPa)
ktap	$1.000000 \times E + 2$	newton-second/m ² (N s/m ²)
micron	$1.000000 \times E - 6$	meter (m)
mil	$2.540000 \times E - 5$	meter (m)
mile (international)	$1.609344 \times E + 3$	meter (m)
ounce	$2.834952 \times E - 2$	kilogram (kg)
pound-force (lbs avoirdupois)	4.448222	newton (N)
pound force inch	$1.129848 \times E - 1$	newton-meter (N m)
pound-force/inch	$1.751268 \times E + 2$	newton/meter (N/m)
pound-force/foot ²	$4.788026 \times E - 2$	kilo pascal (kPa)
pound-force/inch ² (psi)	6.894757	kilo pascal (kPa)
pound-mass (lbm avoirdupois)	$4.535924 \times E - 1$	kilogram (kg)
pound-mass-foot ² (moment of inertia)	$4.214011 \times E - 2$	kilogram-meter ² (kg m ²)
pound-mass/foot ³	$1.601846 \times E + 1$	kilogram/meter ³ (kg/m ³)
rad (radiation dose absorbed)	$1.000000 \times E - 2$	**Gray (Gy)
roentgen	$2.579760 \times E - 4$	coulomb/kilogram (C/kg)
shake	$1.000000 \times E - 8$	second (s)
slug	$1.459390 \times E + 1$	kilogram (kg)
torr (mm Hg, 0° C)	$1.333220 \times E - 1$	kilo pascal (kPa)

*The becquerel (Bq) is the SI unit of radioactivity; 1 Bq = 1 event/s.

**The Gray (Gy) is the SI unit of absorbed radiation.

TABLE OF CONTENTS

Section	Page
SUMMARY	iii
PREFACE	vii
CONVERSION TABLE	viii
LIST OF ILLUSTRATIONS	xi
1 INTRODUCTION	1
2 IRREGULARITY CHARACTERISTICS	5
2.1 Spectral Characteristics	6
2.2 Irregularity Source Regions	10
2.3 Convective Distribution	14
3 LARGE-SCALE PLASMA STRUCTURE ($\lambda > 10$ km)	21
3.1 Polar Cap Patches	21
3.1.1 Observations	21
3.1.2 Patch Generation Mechanism	27
3.2 Boundary (and Subauroral) Blobs	32
3.2.1 General Properties	32
3.2.2 Source Mechanisms	34
3.3 Sun-Aligned Arcs, Auroral Blobs, and Localized Depletions	43
3.4 Particle Source	46
3.5 Relationship to Smaller-Scale Irregularities	53
4 INTERCHANGE INSTABILITIES	55
4.1 Basic Theory	55
4.1.1 $\underline{E} \times \underline{B}$ Instability	55
4.1.2 Current-Convective Instability	60
4.2 Effects of Background Plasma	62
4.2.1 Basic Considerations	62
4.2.2 Incompressible Background	64
4.2.3 Compressible Background	67
4.3 Other Considerations	68

TABLE OF CONTENTS (concluded)

Section	Page
4.4 Evidence for Interchange Processes	70
4.4.1 Large-Scale Plasma Structure	70
4.4.2 Smaller-Scale Irregularities	76
4.4.3 Spectral Characteristics	85
4.5 Role of Neutral Dynamics	89
5 DESCRIPTIVE WORKING MODEL	96
5.1 Phenomenology	97
5.1.1 Large-Scale Plasma Structure	97
5.1.2 Smaller-Scale Irregularities	99
5.2 Irregularity Generation and Decay	100
5.2.1 MFTI Processes	100
5.2.2 Interchange Instabilities	101
5.3 Spectral Characteristics	104
5.4 Other Processes	105
5.5 Outstanding Questions	106
6 LIST OF REFERENCES	108

LIST OF ILLUSTRATIONS

Figure		Page
1	Examples of One- and Two-Component Irregularity Spectra Measured in situ by the AUREOL-3 Satellite [52]	7
2	Variations in in situ Irregularity Spectral Index ($\lambda < 1$ km) and Their Relationship to Bulk Plasma Velocity (Eastward Component), Energy Deposition Rate, and Fractional Fluctuations in Plasma Density [59]	9
3	Morphology of two HF Backscatter Curtains for Three (Local) Levels of Geomagnetic Activity [60] and Comparison with Morphologies of the Equatorward Diffuse-Auroral Boundary [69] and in situ Irregularity ($\lambda > 2$ km) Boundaries	11
4	Variations in Invariant Latitude (L Shell) of the Lower HF Backscatter Curtain in Winter (L_{BW}) and Summer (L_{BS}), the Ionospheric Trough (L_T), and Plasmapause (L_{PP}), as a Function of Local Time	13
5	Comparison of the Scintillation Boundary [93] to the in situ Irregularity Boundaries [87], and the Ionospheric Trough [104]	16
6	Comparison of Contours of Fractional Fluctuations in Plasma Density [105] Measured in situ ($\lambda > 1.5$ km) at Altitudes Between 400 and 600 km, to Irregularity Boundaries ($\lambda > 2$ km) Derived by Dyson [87]	19
7	Sequence of Contour Maps of foF2 Values Showing the Development of a Polar-Cap Patch	23

LIST OF ILLUSTRATIONS (continued)

Figure		Page
8	Scintillation Intensity Index (S_4) and TEC Variations Associated with Polar-Cap Patches Observed Over Thule, Greenland [42]	25
9	Evidence that F-Region Plasma Enhancements Observed Over Thule, Greenland are Consistent with Solar- Produced Ionization from the Dayside Subauroral Ionosphere [40]	26
10	Evidence that a Reservoir of Solar-Produced Plasma Exists at Subauroral Latitudes in the Day Sector	29
11	Plasma-Density Contours Measured on 11 November 1981 that Show Solar-Produced F Layer, Ionospheric Trough, Boundary Blob, Auroral Blob, and Underlying Auroral E Layer [3]	33
12	Locations of Boundary Blob and Auroral Blobs Observed on 11 November 1981 [3]	35
13	Latitudinal Relationship of the Boundary and Subauroral Blobs to the Equatorward Edge of the Auroral E Layer 29 January 1979	36
14	Latitudinal Relationships Between Subauroral Blob, Boundary Blob, and Scintillation, 29 January 1979 [6]	37
15	Computer Simulation of Convection Distortion of a Circular Patch (Shaded Region in Upper Left Panel) in the Polar Cap into a Form Resembling the Boundary (or Subauroral) Blob [4]	39

LIST OF ILLUSTRATIONS (continued)

Figure		Page
16	Example of an Auroral Blob Situated Along the Polar-Cap Boundary, 9 September 1983 [54]	45
17	Rocket Measurements in the Dayside Cusp Showing High Correlation Between Electron Precipitation and Associated F-Region Plasma Density [36]	47
18	Typical Electron Spectra for Different Auroral Precipitation Events	49
19	Computer Simulation of the Ionospheric Response to the Soft/Night Model Electron Flux shown in Figure 18	50
20	Evidence for Rapid Ionization in the F Region by Discrete Electron Precipitation	52
21	Simplified Schematic Diagram Showing the Basic Mechanics of the $\underline{E} \times \underline{B}$ Instability	56
22	Contour Maps of Plasma-Density Distribution (at 360, 400 and 440 km Altitudes) that Reveal East-West Blob Structure at Large-Scale Sizes, 10 November 1981	71
23	Latitudinal Distribution of Plasma Density Associated with East-West Structure in Figure 22	72
24	Contour Map of the Northward Velocity Component Associated with East-West Structure in Figure 22	74
25	Contour Maps of Plasma Density at 300-km Altitude, Ion Velocity Vector, and Slip Velocity Vector, Showing the Spatial Interrelationships, 25 February 1984 [5]	75

LIST OF ILLUSTRATIONS (continued)

Figure		Page
26	Examples of Asymmetric Irregularity Distributions in Relation to Mean Plasma-Density Gradients, and the Occurrence of 10-km-Scale Wavelike Structures	79
27	Morphology of Irregularity Anisotropy Determined from Spaced-Receiver Scintillation Measurements Using the Wideband-Satellite-Beacon Transmissions [202]	81
28	Enlarged Illustration of Asymmetric Irregularity Distribution	87
29	Diurnal Variation in the Meridional Neutral Wind Determined from Chataniks Incoherent-Scatter Measurements and Associated Convection Velocity Components	90
30	Average Neutral-Wind Components (in Geomagnetic Coordinates) for High Geomagnetic Activity [229]	92
31	Asymmetry in Ion Temperatures in the Evening and Morning Sectors as a Function of Zonal Convection Velocity	95

SECTION 1

INTRODUCTION

Recent progress on the topic of high-latitude F-region irregularities follows largely from discoveries (1) that irregularities responsible for radio-wave scintillation and radar backscatter frequently occur in latitudinally confined regions with widths ≤ 100 km, and (2) that those irregularity regions are often spatially correlated with 100-km-scale enhancements in plasma density (called "blobs"). Perhaps most thought provoking have been the two- and three-dimensional spatial descriptions of blobs by incoherent-scatter radar [1, 2-6], at least for identifying irregularity source mechanisms. These descriptions indicate that blobs are characterized by steep gradients transverse to the geomagnetic field.

Because blobs often dominate the structural properties of the polar F layer, particularly during years of high solar activity, it is not surprising that earlier reports describe blob-related effects. Scintillations in signal transmissions from radio stars [7] and polar-orbiting satellites [8-10] were often found to be highly localized in time and space. Their burstlike appearances have been known for some time [11, 12]. Puzzling dropouts of satellite transmissions at 20 MHz [13, 14] might now be interpreted in terms of blob-related effects. Similarly, many of the variations in total electron content (TEC) observed in the past [15] are likely to have been produced by blobs. More recently, plasma-density characteristics measured in situ by satellites [16] appear to include those of blobs. But other than results from a single rocket measurement [17], the spatial collocation of intense, smaller-scale irregularities with larger-scale gradients in plasma density has not been appreciated until recently [2, 6, 18-21].

This recent recognition that there is high spatial correlation between intense, small-scale irregularities and steep transverse gradients that characterize the walls of large-scale plasma structure has

led naturally to the consideration of convective plasma processes such as fluid interchange instabilities [22-24] and other means of magnetic-flux-tube interchange (MFTI) as dominant sources of irregularities. Consideration of irregularity production at high latitudes by interchange instabilities follows historically from past successes in interpreting barium ion-cloud irregularities in terms of the gradient-drift ($\underline{E} \times \underline{B}$) instability [25, 26], and equatorial F-region irregularities in terms of the collisional Rayleigh-Taylor and gradient-drift instabilities [27-30]. The recent suggestion that the current-convective instability might be a source mechanism for high-latitude F-region irregularities [22, 31], however, is new in the sense that field-aligned currents have not been considered previously as a source of free energy within the context of interchange instabilities.

The view that convective plasma processes dominate polar irregularity production may be contrasted with earlier suggestions that kilometer-scale irregularities are produced primarily by particle precipitation [11, 32-35]. The analysis presented in this review indicates that particle precipitation can contribute significantly to the formation of plasma structure with scale sizes > 10 km near the F-layer peak (perhaps together with other processes). Its contribution to irregularity formation at scale sizes less than a few kilometers, however, is probably small compared to that from an interchange instability. Similar conclusions were drawn by Kelley et al. [36]. Structured particle precipitation is believed to become increasingly important as a source of kilometer-scale irregularities at lower F-region altitudes [37, 38], but its absolute fluctuation intensity is much weaker than found near the peak of the F layer.

Because walls of large-scale structure seem to play an integral role in irregularity production, interest has grown in the phenomenology of large-scale F-region structure, i.e., blobs in the auroral zone [4, 6], and the more recently discovered "patches" in the polar cap [39-42]. Patches appear to be solar-produced plasma transported from lower latitudes in the dayside ionosphere through the polar cap into the nightside

auroral region. Both patches and blobs are envisioned as potentially active regions for MFTI processes. Hence, an understanding of high-latitude irregularities now requires knowledge of processes that control the appearance of solar-produced plasma in polar regions and blobs in the auroral zone. Attention, therefore, has been diverted from particle precipitation to processes such as global electrodynamics and control by the interplanetary magnetic field (IMF).

On the basis of the above discussion, we focus this review on convective plasma processes and interchange instabilities as sources of high-latitude F-region irregularities. To keep the review manageable, we have not considered other promising, irregularity-source mechanisms. Most other irregularity-production mechanisms, however, have been described in earlier review papers [43-47]. In Section 2, we begin by identifying auroral regions where irregularities are actively generated. We do so by arguing that meter-scale irregularities must be spatially coincident with the dominant irregularity-source regions. This interpretation follows because meter-scale irregularities dissipate in seconds through cross-field diffusion, and hence, can exist only in regions where strong irregularity growth counteracts rapid decay. We further demonstrate that the morphology of kilometer-scale irregularities resembles the identified irregularity-source regions, lending support to the concept that related physical processes are acting to produce irregularities with scales from meters to few kilometers. Differences in morphology are attributed to convective distribution or the presence of weaker sources.

In Section 3, we review the phenomenology of large-scale plasma structure ($\lambda > 10$ km) and find it consistent with that for smaller-scale irregularities ($\lambda < 10$ km); i.e., irregularity-source regions seem to occur in the vicinity of large-scale structure and the associated gradients required for irregularity generation by convective plasma processes. To provide a broader perspective, we develop a scenario for the underlying processes responsible for the large-scale structure.

In Section 4, we review fluid interchange instabilities and factors that influence their effectiveness in irregularity production. We find

that the $\underline{E} \times \underline{B}$ (gradient-drift) instability is the dominant mechanism in the polar ionosphere, and is strongly modulated by (1) the plasma drift relative to the neutral gas, and (2) the highly-conducting and compressible, auroral E layer. We again find that consideration of these factors leads to an irregularity morphology that is consistent with the identified irregularity-source regions.

Finally, in Section 5, we present a descriptive model for high-latitude F-region irregularities. Except for patches of solar-produced plasma and blobs produced by soft-particle precipitation, most observed plasma structures can be accounted for by MFTI that is driven by irregular electric fields applied onto the F layer from other altitudes (E layer, magnetosphere) or by the $\underline{E} \times \underline{B}$ instability. The basic irregularity ($\lambda < 10$ km) model is one controlled by (1) irregular or unsteady convection, (2) thermospheric dynamics, and (3) polarization shorting effects from a highly-conducting auroral E layer.

SECTION 2

IRREGULARITY CHARACTERISTICS

A major obstacle underlying most investigations of high-latitude F-region irregularities is the need to consider the history of the irregularities in question. This need is dictated by long lifetimes of kilometer-scale irregularities and by rapid convection in the polar ionosphere. Irregularity characteristics determined at any given time and location, therefore, can be strongly colored by processes that affect irregularities during their journey from source to point of measurement. Because the most intense features are imposed on irregularities while in source regions, it would be extremely useful to identify those regions. With this knowledge and a suitable convection model, it would then be possible to investigate the history of the irregularities in question.

We, therefore, begin this review by considering irregularity characteristics that are useful for identifying the most persistent irregularity-source regions. The approach taken here is to recognize that meter-scale irregularities (in contrast to kilometer-scale irregularities) are dissipated within seconds by cross-field diffusion and, consequently, cannot convect to great distances from their generation region. The morphology of meter-scale irregularities, therefore, can be interpreted as that of irregularity-source regions. Because various source and dissipation mechanisms can operate independently at different irregularity wavelengths (λ), the pivotal question is whether kilometer-scale irregularities also are produced in those regions. We use irregularity spectral characteristics to argue that related physical processes are operating from around 10 km down to a few m. With this as a basis, we can use observations of meter-scale irregularities to identify active regions of strong irregularity production. Differences in the morphology

of long-lived, kilometer-scale irregularities with that of irregularity-source regions are interpreted in terms of convective distribution (or presence of weaker source regions).

2.1 SPECTRAL CHARACTERISTICS.

Most in situ satellite measurements of irregularity spectra are well approximated by a power-law form characterized by a single spectral index, p , i.e., value of the exponent. The most commonly reported value for p is 1.9 [38, 48-50] with other values ranging from 1.5 to 2.5 [51, 52]. These spectral indices were derived from measurements covering various wavelength regimes (up to 100 km), but most appear to refer to $\lambda < 10$ km. Villain et al. [52] found that 75 percent of their processed spectra ($40 \text{ m} < \lambda < 1 \text{ km}$) could be approximated by a single spectral index. Irregularity spectra derived from in situ rocket measurements also have $p < 2$ [36, 53].

Irregularity spectra also are inferred from scintillation measurements. If irregularities produce only weak scatter, phase-screen models dictate that irregularities with a power-law spectrum will produce a signal phase spectrum with a spectral index that is steeper by unity than p , the one-dimensional in situ spectral index [54, 55]. Using this conversion, spectral indices derived from scintillation measurements appear similar but slightly lower than the above-described results. Basu et al. [56] reported p to be 1.4 in the auroral zone and 1.3 in the polar cap. Fremouw et al. [57] found values between 1.1 and 1.5 for $300 \text{ m} < \lambda < 6 \text{ km}$.

Occasionally, irregularity spectra are better fit by two power-law segments having different spectral indices [49, 52, 57, 58]. Examples of one- and two-component spectra derived from in situ measurements are presented in Figure 1 [52]. In the two-component spectrum, the spectral index at long wavelengths, p_1 , is usually smaller than that at short wavelengths, p_2 . The value of p_1 is closer to p found in one-component spectra. The knee in the two-component spectrum (λ_f) is seen in this example to be around 300 meters. Fremouw et al. [57] also reported a

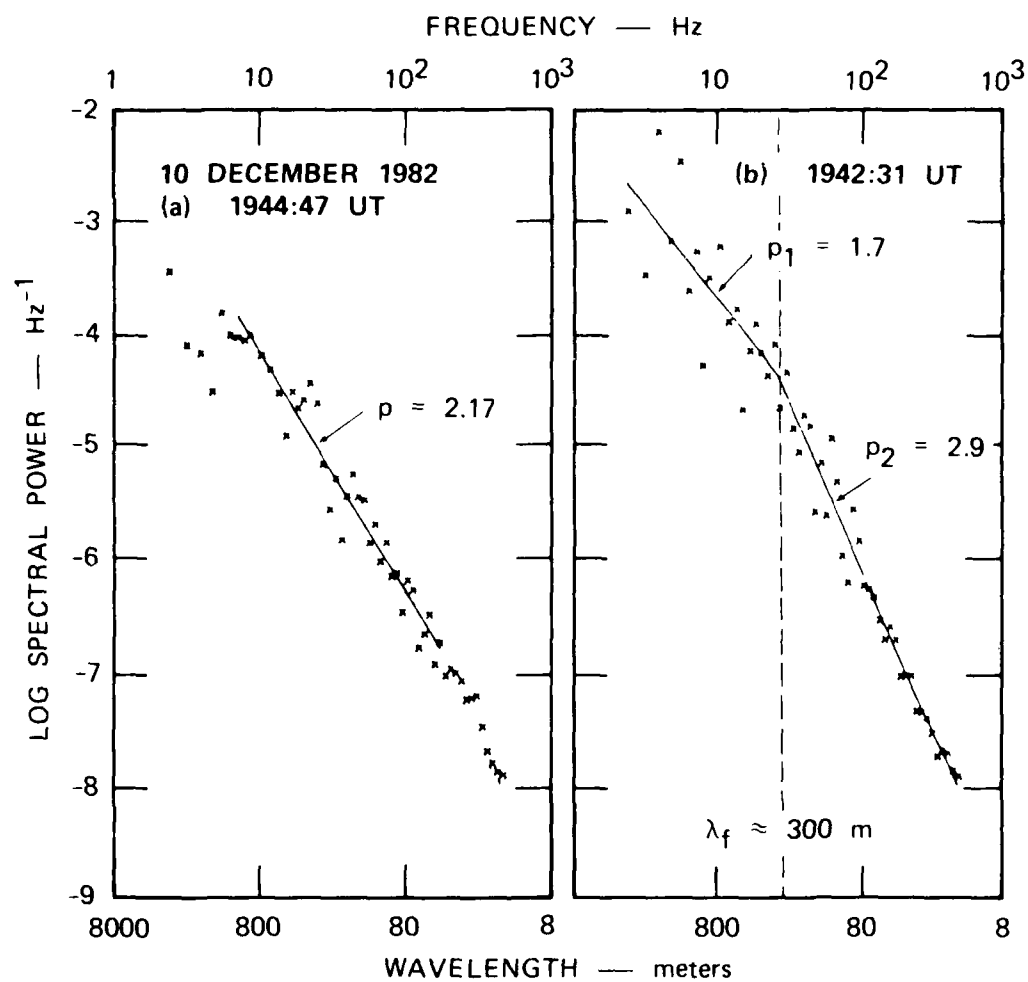


Figure 1. Examples of one- and two-component irregularity spectra measured in situ by the AUREOL-3 satellite [52].

spectral break around 300 m using scintillation measurements. (Note, however, that there is a shallowing of the spectral slope in the left panel of Figure 1 that was not fit by the power-law curve. The break-point seems to occur around 800 m.) Both Fremouw et al. [57] and Villain et al. [52] reported the occurrence of two-component spectra in about 25 percent of their data sets; Phelps and Sagalyn [49] also reported such spectra in 10 percent of their data.

There is some evidence that the variability in p ($\lambda < 1$ km) is associated with irregularity production and decay. Basu et al. [59] analyzed in situ data obtained with the Atmospheric Explorer-D satellite and found that p varied systematically with auroral parameters. The largest fractional fluctuations in plasma density were found in regions in which p approached unity and in which electric fields were large and structured. Values of p near 3 were found in regions of auroral particle precipitation. They concluded that regions of small p corresponded with irregularity production and regions of large p with irregularity decay. One of their data sets is reproduced in Figure 2. The variation in p between unity and 3 seems consistent with the development of two-component spectra (in which p_1 in Figure 2 corresponds to p_2 in Figure 1). These results differ, however, from those reported by Villain et al. [52]. They showed that the spectral index ($40 \text{ m} < \lambda < 1 \text{ km}$) increases with irregularity strength, reaching a value of 3 under exceptional cases.

In summary, spectral characteristics support the hypothesis that related physical processes operate at all irregularity wavelengths of interest. There is no obvious evidence for the presence of a strong, independently operating source mechanism at any preferred wavelength. This conclusion is supported by Villain et al. [52] who showed that irregularity strengths deduced from HF backscatter are comparable to those from in situ measurements. If an independent irregularity source did exist at short wavelengths, we would expect either a decrease in p_1 or p_2 , or the appearance of a peak in the spectrum. From the statistical absence of such features, we conclude that meter-scale irregularities are

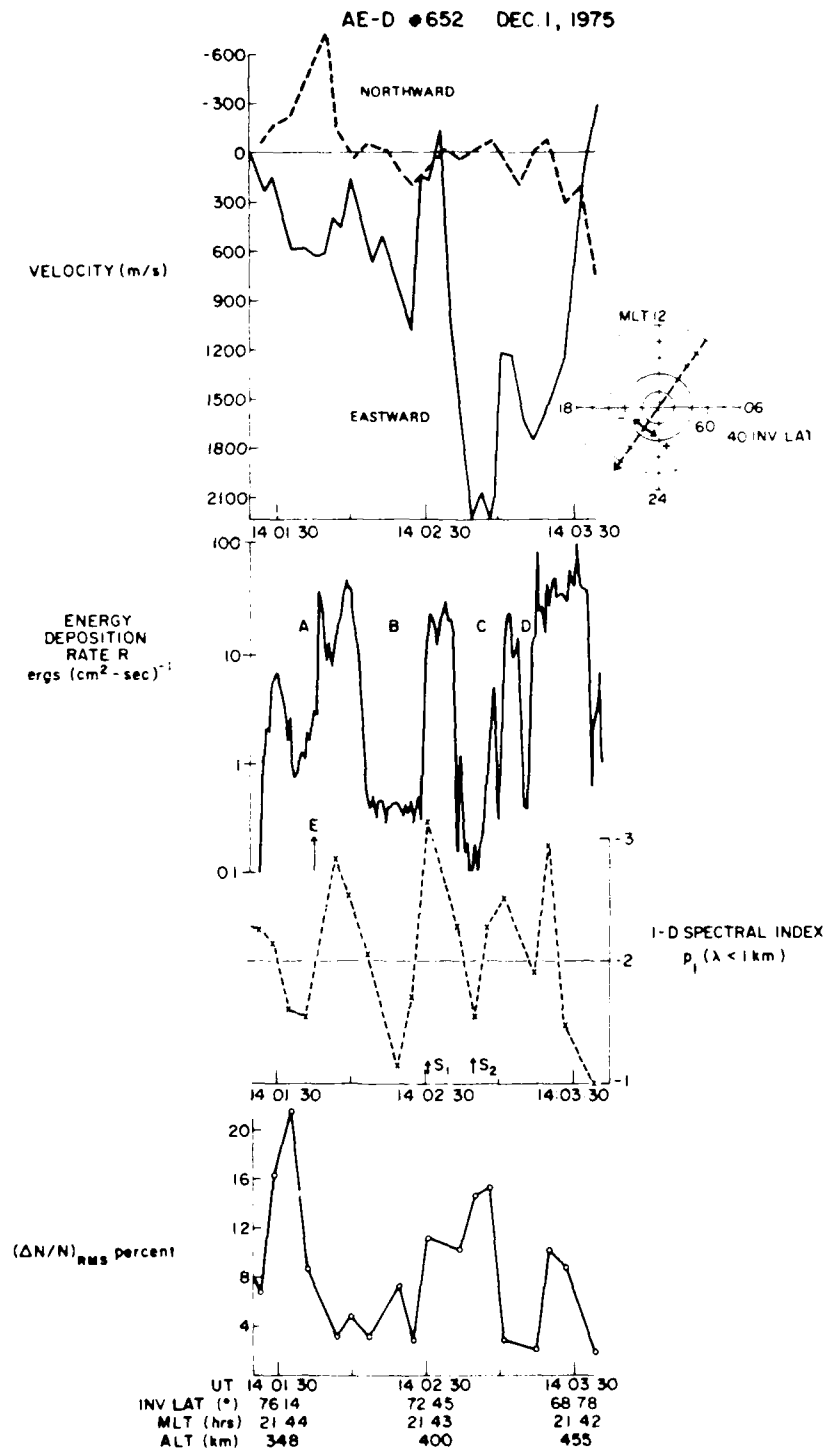


Figure 2. Variations in in situ irregularity spectral index ($\lambda < 1$ km) and their relationship to bulk plasma velocity (eastward component), energy deposition rate, and fractional fluctuations in plasma density [59].

generated by processes intimately related to the source mechanism that generates km-scale irregularities and that its morphology also represents source regions for kilometer-scale irregularities.

2.2 IRREGULARITY SOURCE REGIONS.

From the foregoing, we seem justified in identifying irregularity-source regions from the morphology of meter-scale irregularities, e.g., that derived from HF backscatter measurements. Möller [60], using a swept-frequency backscatter radar operated in the HF band (3 to 30 MHz), showed that there are two latitudinally-narrow regions of intense backscatter, or HF "curtains". The two backscatter curtains derived from solar-maximum data [60] are replotted in polar geomagnetic coordinates in Figure 3. Three curves for each backscatter curtain are shown, representing different levels of geomagnetic activity.

The poleward HF curtain, shown by triangles and circles connected by lines, forms a circle indicating occurrence at all local times. The radius (15.5°) and latitudinal displacement (3.5°) of the circle towards midnight are similar to parameters of the best-fit circle (radius = 14.6° , displacement = 6.1°) that represents the location of the most-poleward and extended quiet arcs [61], and the poleward boundary of the quiet auroral oval [62]. The poleward HF curtain also seems to be collocated with (1) the poleward trapping boundary for > 40 -keV electrons [63], (2) a polar ring of strong topside spread F_λ [64], and (3) the F-layer irregularity zone (FLIZ) detected in the day sector with ionosondes [65-67]. Doppler measurements associated with the poleward HF curtain in the premidnight sector indicate sunward plasma drift [68]. These results suggest that the poleward HF curtain is situated near the poleward portion of the auroral oval and not in the polar cap.

The occurrence of the equatorward HF curtain is seen in Figure 3 to favor the night sector with a local-time distribution that is asymmetric relative to the noon-midnight meridian. The asymmetry depends on geomagnetic activity with the HF curtain shifting to lower latitudes and earlier local times with increasing geomagnetic activity. By super-

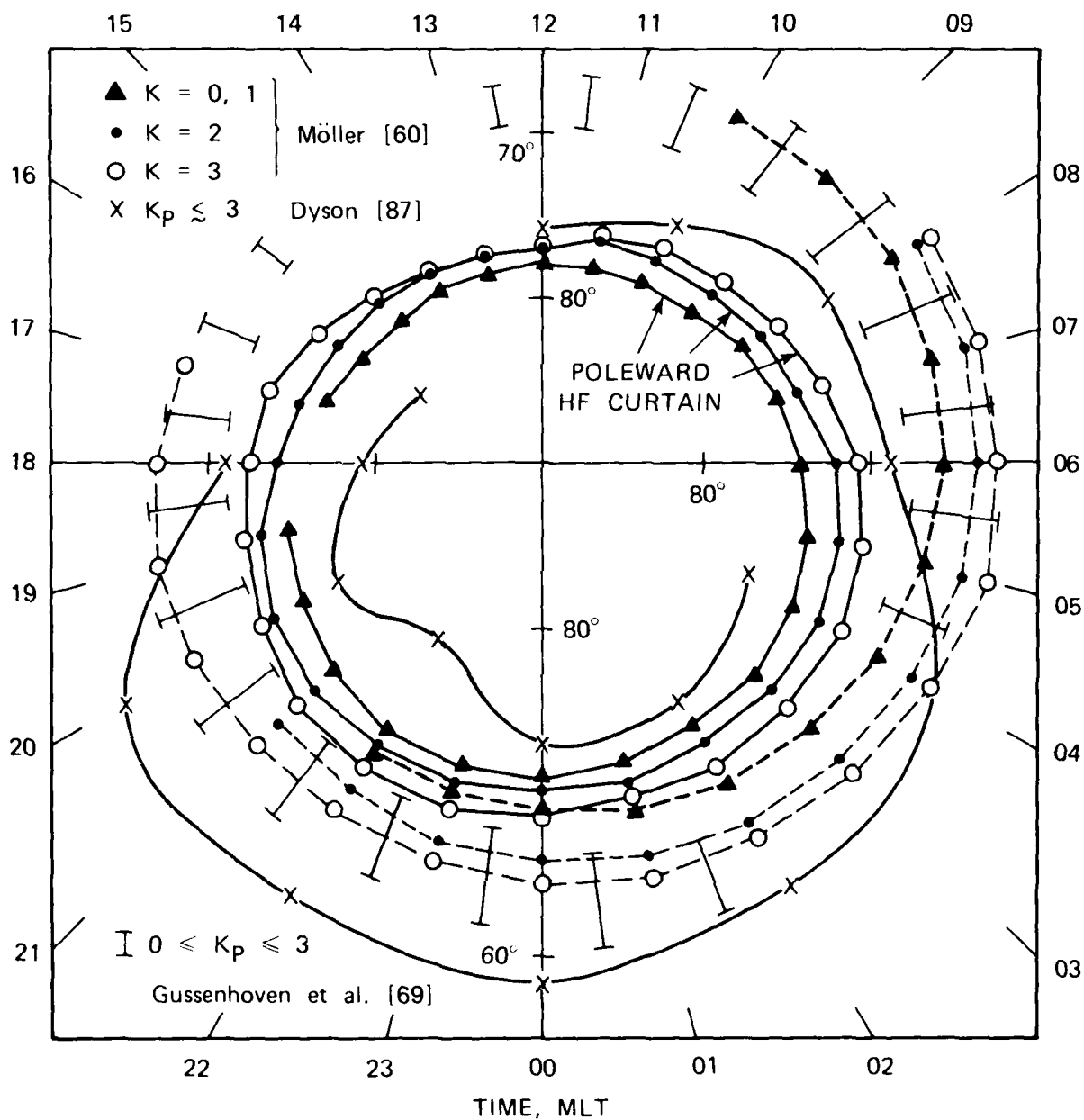


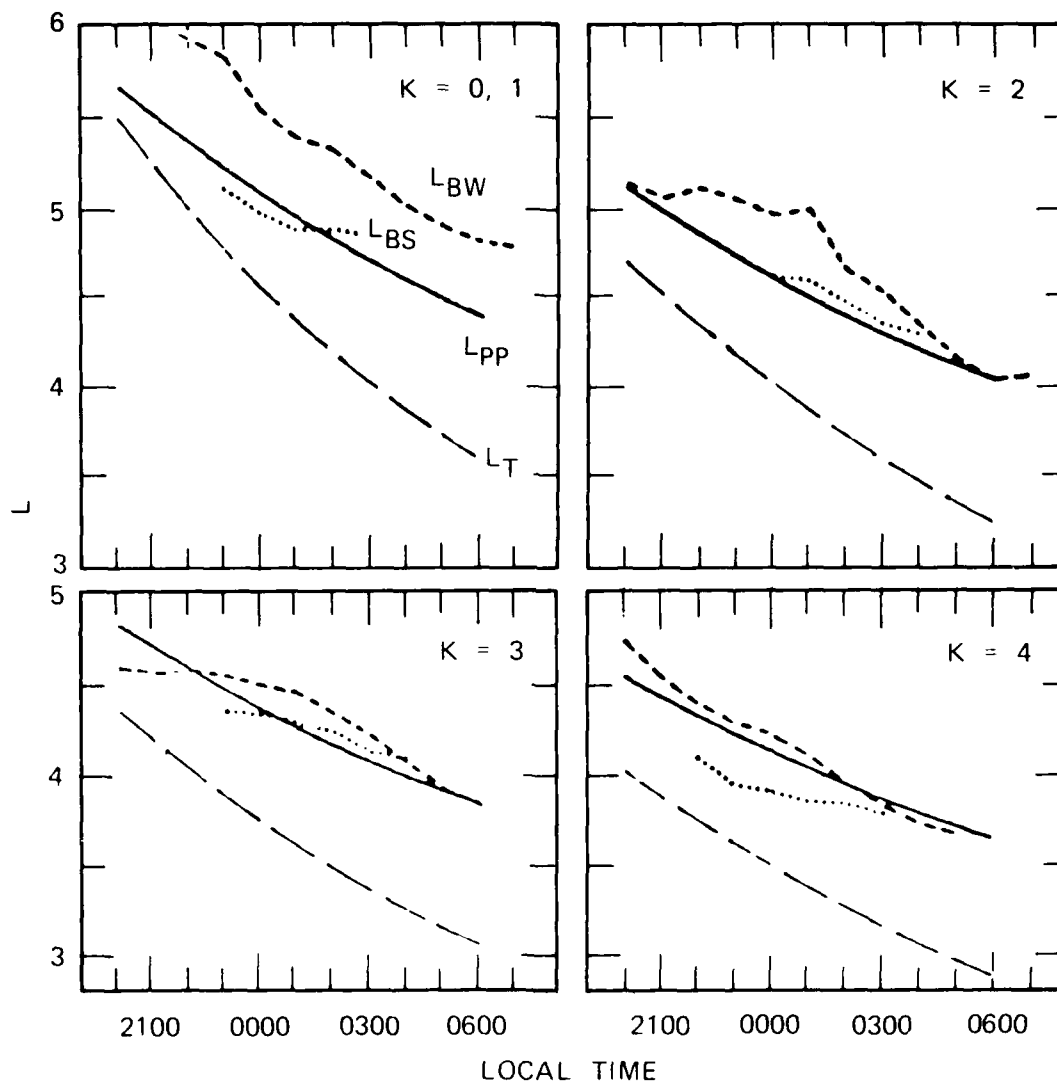
Figure 3. Morphology of two HF backscatter curtains for three (local) levels of geomagnetic activity [60] and comparison with morphologies of the equatorward diffuse-auroral boundary [69] and in situ irregularity ($\lambda > 2$ km) boundaries.

imposing the location of the equatorward boundary of the diffuse aurora over those of the HF curtains, we find that the equatorward HF curtain is situated close to that auroral boundary. The radial line segments in Figure 3 [69] represent the range of latitudes of the diffuse auroral boundary for $0 \leq K_p \leq 3$. There is excellent agreement for the $K_p \approx 3$ case in the dawn and dusk sectors, with some differences in the midnight sector. (Differences in the midnight sector can be attributed to westward electric fields that develop there during substorm activity.) Although the agreement is not as good for the $K_p = 0$ case, it seems reasonable to conclude that the equatorward HF curtain is probably associated with equatorward auroral boundary. The correlation is particularly impressive in the prenoon sector where few other auroral features are found at such low latitudes ($< 70^\circ$).

Other observations support this conclusion. Möller [60] showed statistically that the equatorward HF curtain was situated near the plasmopause, just poleward of the ionospheric trough, and that the latitudinal locations of these features moved in unison as a function of local time. His results are reproduced in Figure 4. All three curves are seen to have similar form, shifting to lower latitudes with increasing local time. Similar relationships were obtained in case studies using HF backscatter and satellite measurements [63, 70], and using HF backscatter and whistler measurements [71].

Nekrasov et al. [72] also reported two maxima in backscatter intensity. The poleward maximum in backscatter strength was observed to be situated around 68° geomagnetic latitude at all local times. The equatorward maximum was located around 60° geomagnetic latitude and observed only in the night sector. While their local-time distributions resemble those of Möller [60], they differ in that (1) there is not latitudinal variation as a function of local time, and (2) there is a large latitudinal difference between the two sets of measurements in the day sector.

We have thus identified two irregularity-source regions in the auroral zone; however, the distribution of meter-scale irregularities has yet to be determined for the polar cap region. We hope HF backscatter



[Source: Møller (1974)]

Figure 4. Variations in invariant latitude (L shell) of the lower HF backscatter curtain in winter (L_{BW}) and summer (L_{BS}), the ionospheric trough (L_T), and plasmopause (L_{PP}), as a function of local time.

radars operated with viewing geometries over the polar cap will be useful for this purpose [68, 73-77]. Earlier experiments using HF backscatter radars to view polar regions have demonstrated that meterscale irregularities are often visible in auroral regions but information on their existence or distribution in the polar cap was not published [78, 79].

2.3 CONVECTIVE DISTRIBUTION.

We now proceed to compare the locations of the irregularity-source regions with those of kilometer-scale irregularities. By doing so, we verify our initial assertion from spectral characteristics that similar physical processes operate over the entire wavelength range of interest, and interpret differences in the morphologies to convective distribution of the larger-scale irregularities and continued structuring at much weaker growth rates. On this basis, we expect the most-intense kilometer-scale irregularities to be generated in the two irregularity-source-regions; and because plasma transport is largely zonal in the auroral zone, the most-intense kilometer-scale irregularities are likely to be observed in the vicinity of those source regions.

There is considerable evidence, both statistical and from case studies, that intense kilometer-scale irregularities are found near the equatorward auroral boundary. Möller and Tauriainen [80] found that the equatorward HF curtain and enhanced scintillation occurred along the poleward wall of the ionospheric trough; moreover, both were found to have the same latitudinal dependences on local time and season. Because the measurements were made 1000 km apart in longitude, they concluded that the irregularity source region must closely follow lines of constant geomagnetic latitude. Other scintillation measurements made at night also have shown that the scintillation boundary is situated just poleward of the ionospheric trough [6, 18, 81, 82]. There also exists a sub-auroral region of F-region irregularities that lies equatorward of the trough minimum. The distinct presence of subauroral (kilometer-scale) irregularities has been seen in in-situ satellite measurements [83, 84] and in scintillation data [85]. Scintillation is weak or nonexistent in

the central trough [85, 86]. (Although processes similar to those for high-latitude irregularities may be responsible for subauroral irregularities, a review of such results is beyond the scope of this paper.)

To review the statistical evidence relating kilometer-scale irregularities and the equatorward auroral boundary, we return to Figure 3 where we have superimposed the in situ irregularity boundaries ($\lambda > 2$ km) from Dyson [87] onto the morphology of HF curtains. Dyson's boundaries, for $K_p \leq 3$ conditions, are seen to enclose both HF curtains, except in the morning and dusk sectors. The equatorward HF curtain extends in those sectors to latitudes lower than Dyson's irregularity boundary. We interpret these differences to indicate that the equatorward irregularity-source region is most active in the night sector [72], and perhaps extends into the day sector during solar maximum years. (Möller's backscatter data were obtained during solar maximum while Dyson's in situ data were obtained during solar minimum.)

Another useful comparison is between Dyson's equatorward irregularity boundary and a similar boundary determined from scintillation measurements [88-93]. Sketches of the scintillation boundary [93], for geomagnetically quiet ($K_p = 0,1$) and disturbed ($K_p = 5$) conditions, are presented in Figure 5 together with Dyson's boundaries. Dyson's equatorward boundary ($K_p \leq 3$) compares favorably with the quiet scintillation boundary in the night sector, between 2000 and 0900 MLT. There is, however, a clear difference in the dusk sector, with Dyson's equatorward boundary situated more than 10° poleward of the scintillation boundary. The scintillation boundary in the dusk sector is more consistent with the concept of convective distribution if compared with the location of the HF curtain shown in Figure 3. The quiet scintillation boundary, however, is not consistent with the HF curtains in the morning sector. On the other hand, the disturbed scintillation boundary encloses the curtains in that sector. Other irregularity boundaries, including that for electrostatic turbulence, have been compared by Fejer and Kelley [43]. All show generally good agreement with smallest latitudinal differences in the midnight sector.

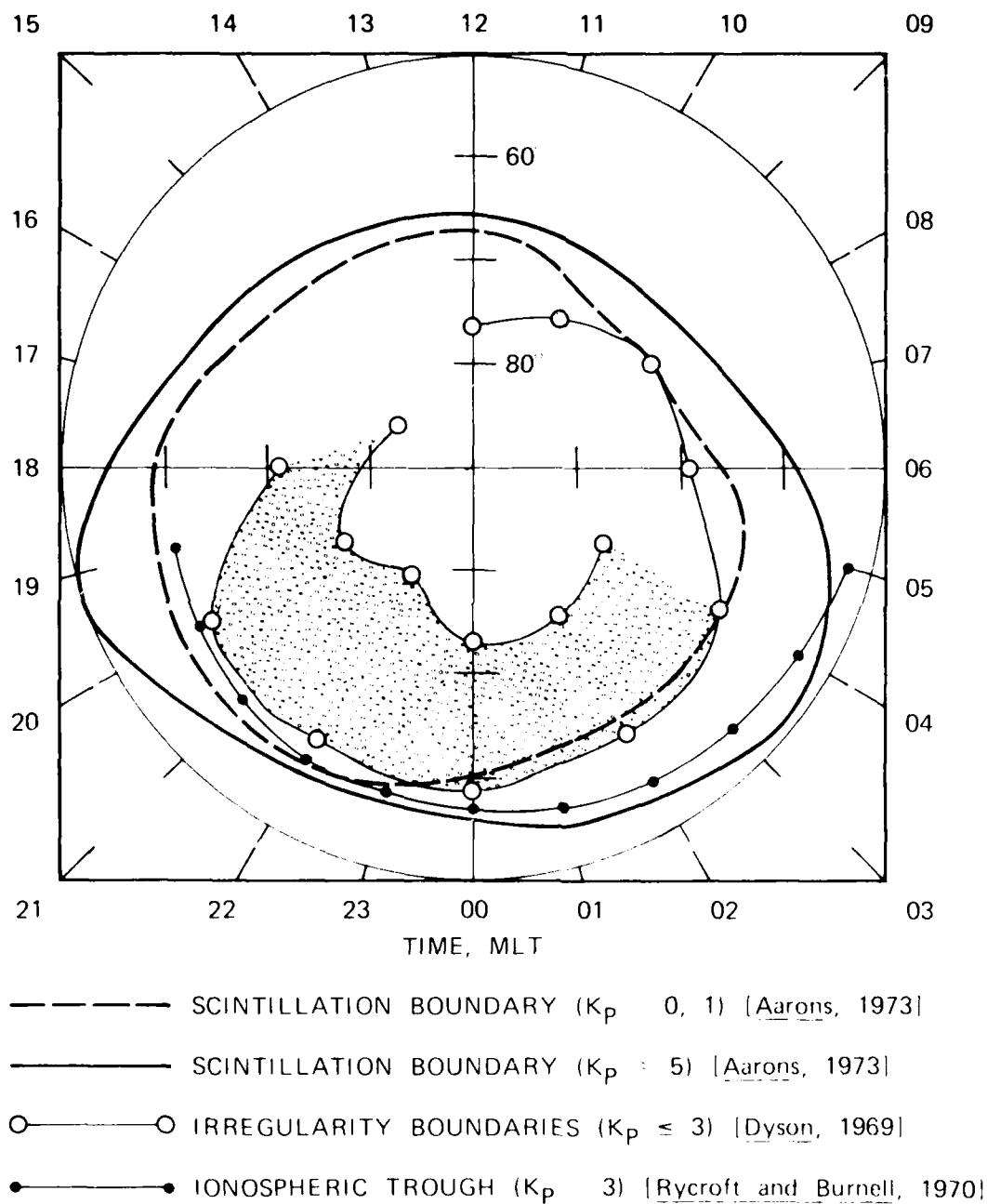


Figure 5. Comparison of the scintillation boundary [93] to the in situ irregularity boundaries [87], and the ionospheric trough [104].

Because the kilometer-scale irregularity boundary derived from in situ measurements is more or less contained within the scintillation boundaries, the differences may reflect measurement sensitivity. Scintillations, being an integrated measurement, may be more sensitive (particularly at lower frequencies) to the distribution of weaker irregularities than in situ measurements. We speculate that the equatorward bulge in the scintillation boundary around 1900 MLT might be associated with the sunset enhancement of F-region irregularities reported in the HF backscatter literature [94-97]. (A sunset scintillation enhancement in the Antarctic also has been reported [98].) We note that the dusk sector is characterized by large subauroral electric fields [99-103] that must be reckoned with when considering irregularity production mechanisms.

The scintillation boundary also can be compared to the trough location shown in Figure 5. The trough curve represents the statistical location of minimum ionization derived from topside ionograms for Summer 1963 and $K_p = 3$ [104]. The trough minimum follows the quiet scintillation boundary closely in the premidnight sector, but diverges from that boundary in the postmidnight sector. The divergence of the trough minimum from the scintillation boundary may indicate the softening of the gradient associated with the equatorward boundary of the auroral F layer or a generally weaker pattern of irregularities in the postmidnight sector. The effect of a change in latitudinal gradient in F-region plasma density is to displace the trough minimum equatorward relative to the latitude of the background plasma density value required to produce significant scintillations. A possibly related softening of the gradient at the scintillation boundary in the postmidnight sector has been reported by Aarons et al. [89]. A general weakening of kilometer-scale irregularities in the postmidnight sector has also been reported [105].

A more quantitative morphology of kilometer-scale irregularities was reported by Clark and Raitt [83, 105]. Using in situ measurements from the ESRO-4 satellite during a period of declining solar activity, Clark and Raitt [83] presented contour plots of plasma-density fluctuations ($\lambda > 1.5$ km) for different altitude ranges. The Northern Hemisphere

portion of their results for the altitude range from 400 to 600 km are sketched in polar coordinates in Figure 6. The shaded areas represent regions of fractional fluctuations in plasma density that exceeded 8 and 10 percent. Note that local solar time is used; conversion to geomagnetic coordinates is difficult because data collected at five different ground stations are intermixed. Nevertheless, the contours do reveal fluctuation intensity characteristics not available in earlier boundary descriptions of the polar irregularity zone.

We find generally good agreement with the ten percent contour regions falling within Dyson's boundaries. The eight percent contours, however, are seen to extend well into the polar cap. Perhaps most interesting is the asymmetric local-time distribution of irregularity strength. The irregularities appear strongest in the afternoon to midnight sector, weaker in the prenoon sector, and weakest in the early morning sector (0200 to 0500 LST).

The occurrence of enhanced irregularities in the premidnight sector has also been reported by Basu and Aarons [34]. They examined the diurnal and seasonal dependence of auroral scintillations using a geostationary satellite. They found a scintillation maximum that occurred in the premidnight sector during the period, March to May. They suggested that the seasonal control of scintillations is related to the variation of the tilt angle of the geomagnetic dipole axis and consequent modulation of particle precipitation in that longitude sector. The hypothesis is thought to be supported by the absence of a seasonal dependence in the Alaskan sector [106]. The Alaskan morphology, however, also contained slightly stronger scintillations in the premidnight sector. Therefore, whether there is a longitudinal dependence in the seasonal control of scintillation, or not, the occurrence of enhanced scintillations in the premidnight sector seems real.

Little is known about kilometer-scale irregularities near the poleward auroral boundary but available evidence seems consistent with the local production of kilometer-scale irregularities. Frihagen and Jacobsen [17] found that the most intense patch of irregularities

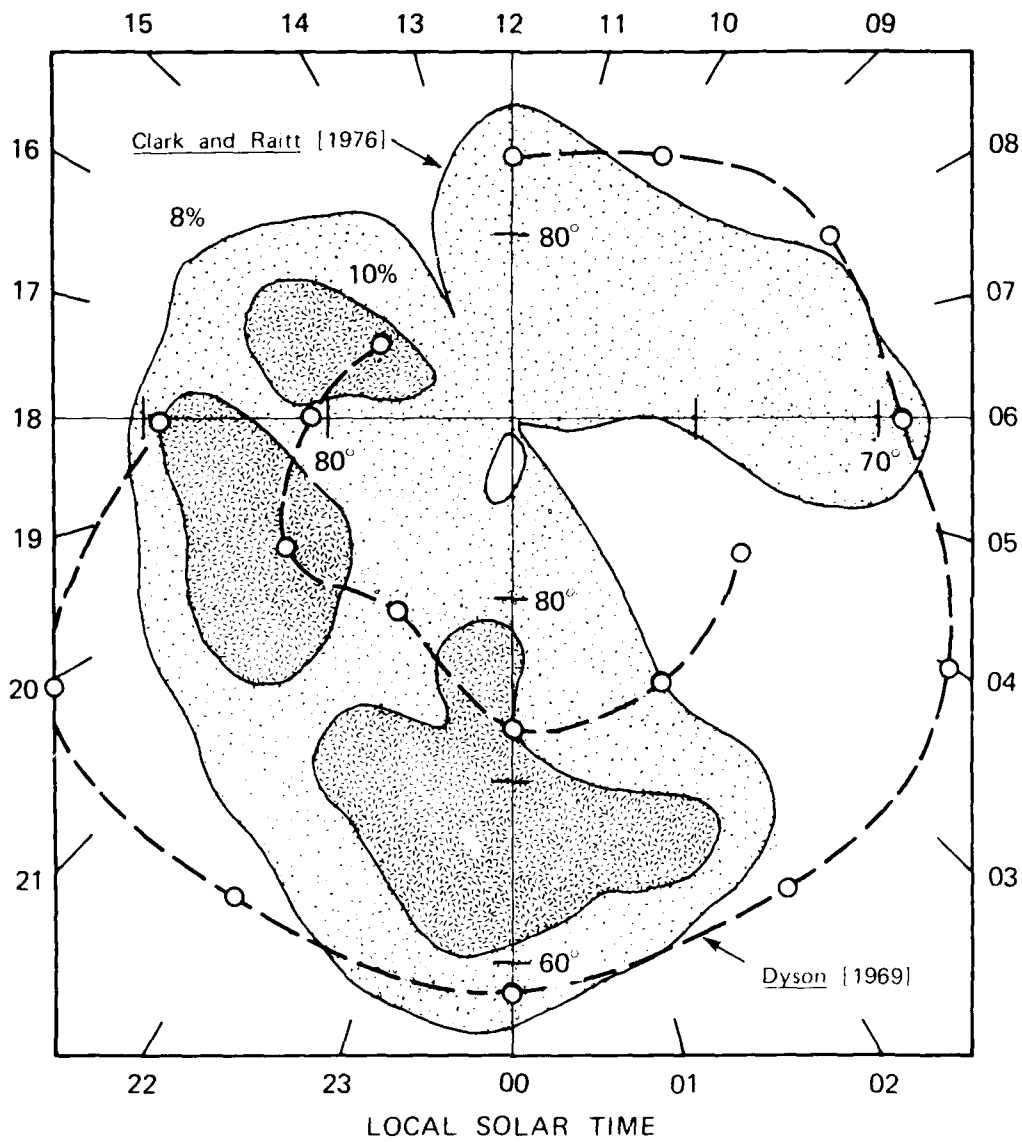


Figure 6. Comparison of contours of fractional fluctuations in plasma density [105] measured in situ ($\lambda > 1.5$ km) at altitudes between 400 and 600 km, to irregularity boundaries ($\lambda > 2$ km) derived by Dyson [87]. The measurements were made during the declining phase of solar activity and during solar minimum, respectively.

detected during a rocket flight which covered 66.9° to 72.4° invariant latitude occurred poleward of the visual aurora. That irregularity patch was also found to be associated with a large-scale gradient in plasma density. Basu et al. [59] presented an unambiguous example for the premidnight sector of enhanced kilometer-scale irregularities along the poleward auroral boundary. The percentage fluctuations in plasma density (for $\lambda < 1$ km) reached 20 percent (a fivefold increase above the background level) in a narrow latitudinal region of sunward convection (> 1.8 km/s). This enhanced irregularity region was situated just equatorward of the velocity reversal boundary that often marks the polar-cap boundary. A preliminary analysis of beacon data from the HILAT satellite also have revealed the persistent occurrence of scintillation patches in this vicinity.

In addition to the auroral zone, kilometer-scale irregularities are found in the polar cap. (Although there is no information on irregularity-source regions in the polar cap to compare to, we include their description here for reference in later sections.) Irregularity strength there appears to be extremely variable, with maximum intensities occurring during solar maximum, winter and nighttime periods [56, 107]. During periods of maximum solar activity, intense irregularities are observed continuously for 24 hours a day. Basu et al. [56], for example, showed that the median (50th percentile) value for the scintillation S_4 index at 250 MHz varied between 0.4 and 0.6 at Thule, Greenland (polar cap station), while corresponding estimates at Goose Bay, Labrador (auroral-zone station) varied between 0.1 and 0.5. On the other hand, scintillation virtually disappears in the polar cap during periods of minimum solar activity while they continue to be seen in the auroral zone with only slightly weaker intensities [108]. Decreases in irregularity strength within the central polar cap reported by various researchers therefore correspond to observations made during periods of minimum or declining solar activity [87, 109, 110].

SECTION 3

LARGE-SCALE PLASMA STRUCTURE ($\lambda > 10$ KM)

Large-scale plasma structure has been observed in four distinct forms: (1) polar-cap patches, (2) boundary (and subauroral) blobs, (3) sun-aligned arcs, and (4) auroral blobs. (The term "blob" [9, 36, 111] is used to describe 100-km-scale enhancements in F-layer plasma density seen in maps of ionospheric plasma measured in the magnetic meridian plane.) All four types are of interest because they have been found to be spatially collocated with enhanced kilometer-scale irregularities. We, therefore, review their characteristics and consider their source mechanisms.

3.1 POLAR CAP PATCHES.

Patches are localized enhancements in F-layer plasma density that (1) have horizontal dimensions ranging from a few hundred kilometers to 1000 km, (2) are observed in the polar cap, and (3) represent the largest-scale structure that is associated with kilometer-scale irregularities [39-42].

3.1.1 Observations.

The first definitive observations of patches were reported by Hill [112]. He mentioned a likely association of his class of ionospheric disturbances (i.e., patches) with "sporadic F" events seen in high-latitude ionograms [113-115]. From an analysis of ionograms taken at a large number of stations, Hill [112] described his event type as having the following characteristics: (1) the transient appearance in the polar cap of regions of enhanced plasma density the horizontal dimensions of which are about 2000 km, (2) a peak plasma density in those regions that is virtually identical to that found in the dayside, midlatitude

ionosphere, (3) an event duration of two to three hours, and (4) a close association with the development of auroral currents.

An outstanding patch event, from Hill [112], has been redrawn and is presented (using polar coordinates) in Figure 7. Contours of constant foF2 value describe the geographical distribution (latitude versus longitude) of peak plasma density in the F layer. The three contour plots, constructed from ionograms taken at hourly intervals from a number of stations, reveal the temporal development of a polar-cap patch in the northern polar region. The contour pattern in Figure 7(a) could be interpreted as representative of ambient conditions in the polar F layer. The slight bulge in the > 10 MHz contours and the poleward protrusion of lower-valued foF2 contours from the day sector [local time (LT) at 90° W longitude is 1100 LT] resemble quasi-steady-state features produced by solar- and particle-produced ionization and antisunward convection [116-118].

Figure 7(b) illustrates the penetration phase of the patch formation process. There is strong poleward intrusion of higher-valued foF2 contours that originally were seen only at midlatitudes (e.g., shaded region of > 10 -MHz contours); the enhancement in the polar cap is a factor of four in plasma density (factor of two in foF2 value). The rate of poleward transport of midlatitude plasma, estimated from contour displacements between the top two panels, is about 1 km/s, a value comparable to convection speeds found in polar regions. Penetration of dayside plasma into the nightside is indicated by the crossing of the foF2 contours past the solar terminator at 300-km altitude (dashed curve).

Rapid appearance of enhanced plasma densities in the polar cap that exceed 10^6 el/cm³ cannot be explained in terms of production by enhanced particle precipitation in the polar cleft, particularly when the convection speed is high. Modelling results [117, 118] indicate that enhanced antisunward convection acts to reduce the time spent by a given magnetic flux tube in the latitudinally-restricted cleft region resulting in significantly smaller ionization buildup.

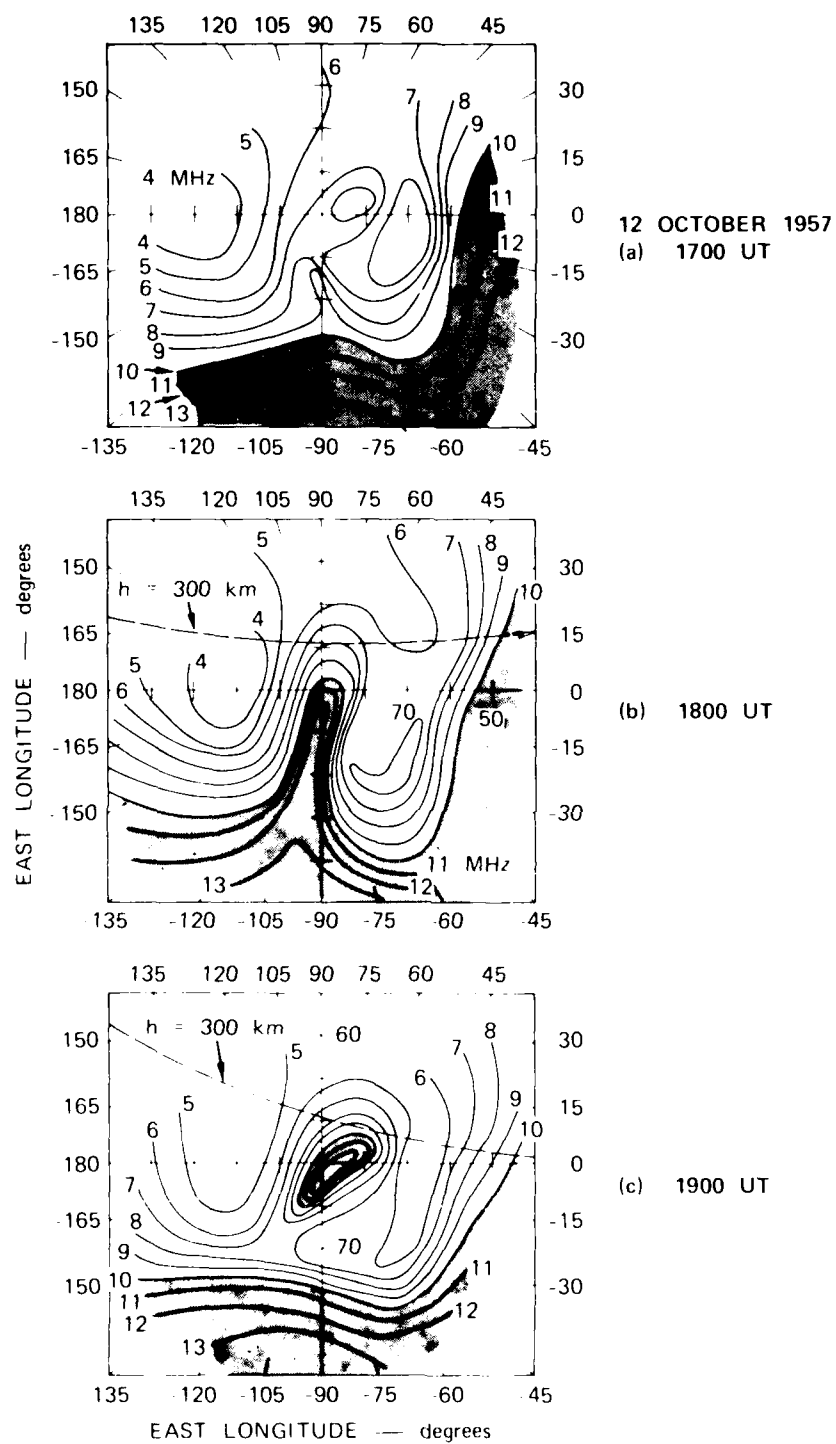


Figure 7. Sequence of contour maps of foF2 values showing the development of a polar-cap patch [isolated shaded region in (c)]. Geographic polar coordinates are used with the solar terminator line at 300-km altitude shown by dashed line segments.

Figure 7(c) illustrates the detachment phase when a patch forms in the polar cap because high-density plasma from midlatitudes is no longer being transported poleward. The apparent change in convection pattern can be inferred from midlatitude contours which have receded to lower latitudes in the day sector. In fact, except for the presence of a patch near the geographic pole, Figure 7(c) closely resembles Figure 7(a). The details of the detachment process, however, are not yet clear.

Progress has been made on the nature of patches. Most patch observations have been made recently in the winter polar cap using various diagnostic sensors at Thule, Greenland and on the Air Force Geophysics Laboratory (AFGL) aircraft [39-42, 119]. The instrumentation have included a 630.0-nm all-sky imaging photometer, an ionosonde, and scintillation receivers. Examples of patches viewed from Thule are presented in Figure 8 [42]. Measurements of variations in TEC using dual-frequency transmissions from the Global Positioning satellite (GPS) are presented in the lower panel. (The upper panel is discussed in Section 3.5.) Unlike the, perhaps stylized, representation of a single patch in Figure 7(c), multiple patches are seen during a 5-hr period with considerable structure within each patch. The largest TEC variations exceed 20 TEC units (1 TEC unit = 10^{16} el/m²). Weber et al. [42] showed that peak plasma densities in these patches were about 8×10^5 el/cm³, enhanced eightfold above the background F layer.

The patch characteristics derived by the AFGL group are similar to those by Hill [112]. They found that patches (1) range in size up to about 1000 km in diameter, (2) occur when the B_z component of the IMF is southward or when $K_p > 4$, (3) appear to originate from a region just equatorward of the dayside cusp region and drift antisunward through the polar cap with speeds of 250 to 700 m/s [42, 119], and (4) appear to be produced by solar radiation and not by soft particle precipitation. Buchau et al. [40] presented a persuasive demonstration of the last feature using Figure 9. They show in the center panel that all peak plasma densities measured in the winter polar cap were consistent with

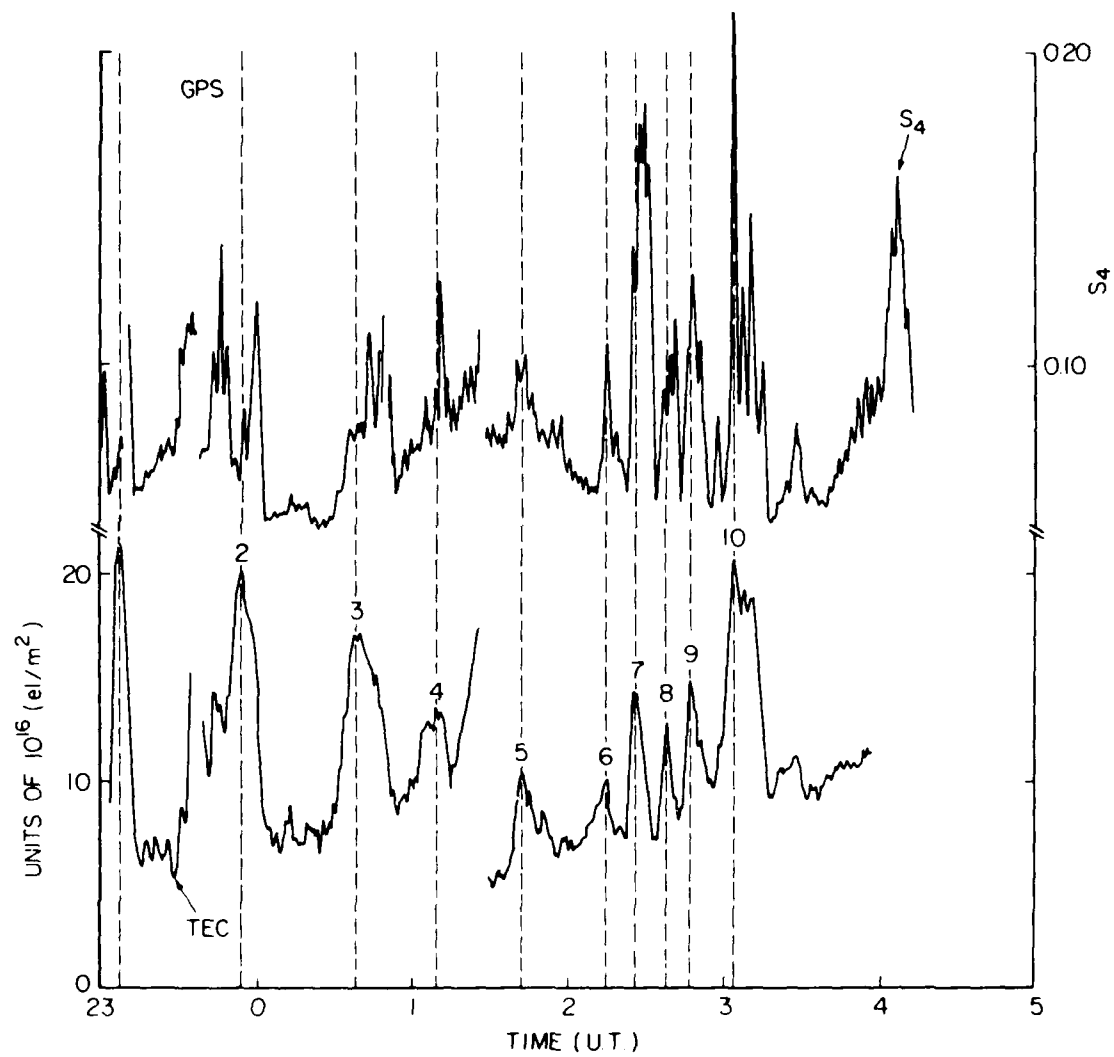


Figure 8. Scintillation intensity index (S_4) and TEC variations associated with polar-cap patches observed over Thule, Greenland [42].

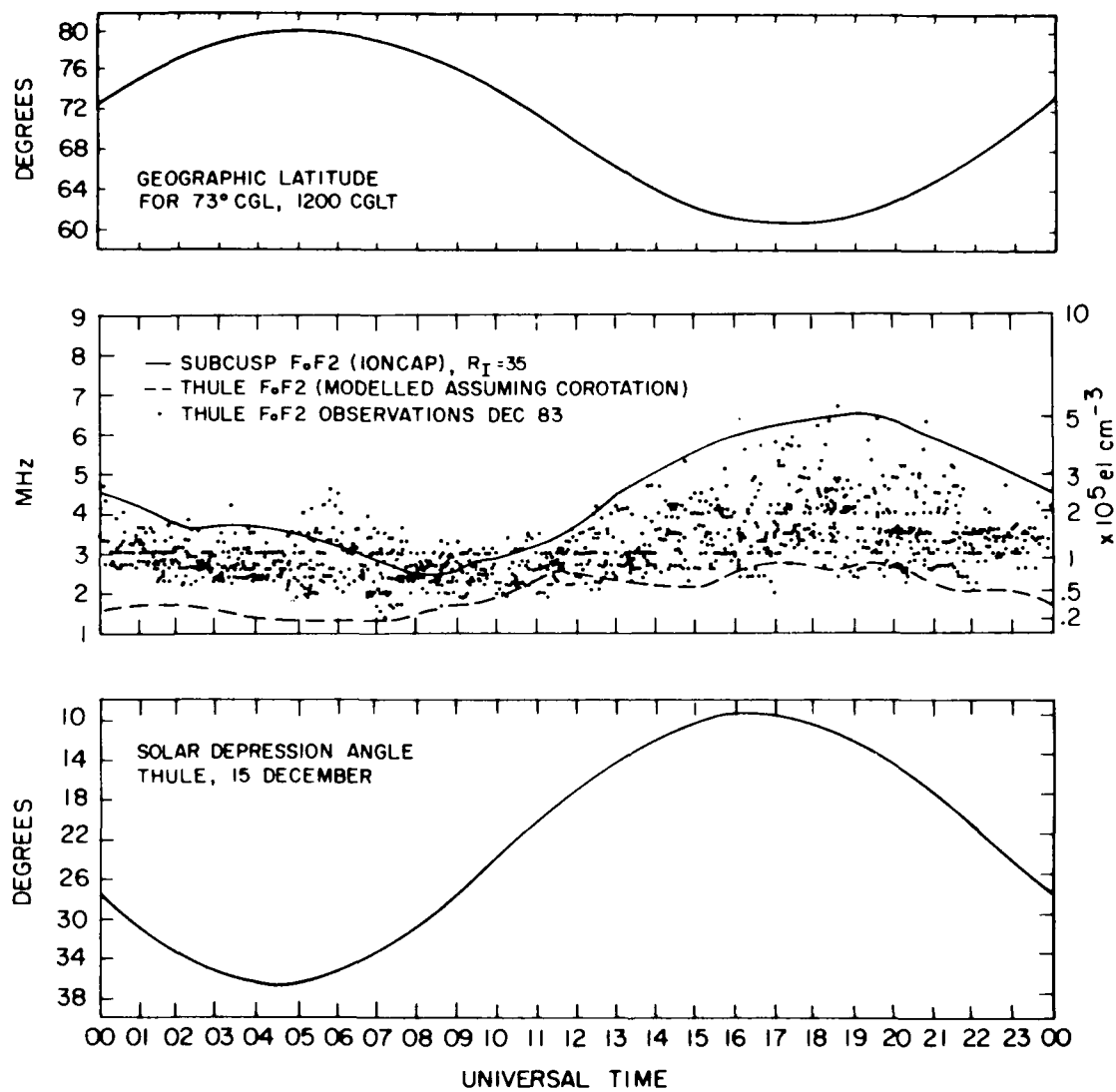


Figure 9. Evidence that F-region plasma enhancements observed over Thule, Greenland are consistent with solar-produced ionization from the dayside subauroral ionosphere (see text) [40].

that expected from solar production. The universal time (UT) variation of solar-produced plasma density at a subcusp latitude that results from the nonalignment of geomagnetic and geographic poles is shown by the line curve. The measured plasma densities (shown by dots) are seen to fall within the envelope created by the line curve but are significantly larger than those expected over Thule from direct solar radiation (dashed curve). A similar UT dependence of the nighttime F layer at high latitude was found by comparing plasma densities measured by incoherent-scatter radars located at different longitudes [120]. High-latitude ionospheric effects of the displaced poles have been modelled by Sojka et al. [121].

3.1.2 Patch Generation Mechanism.

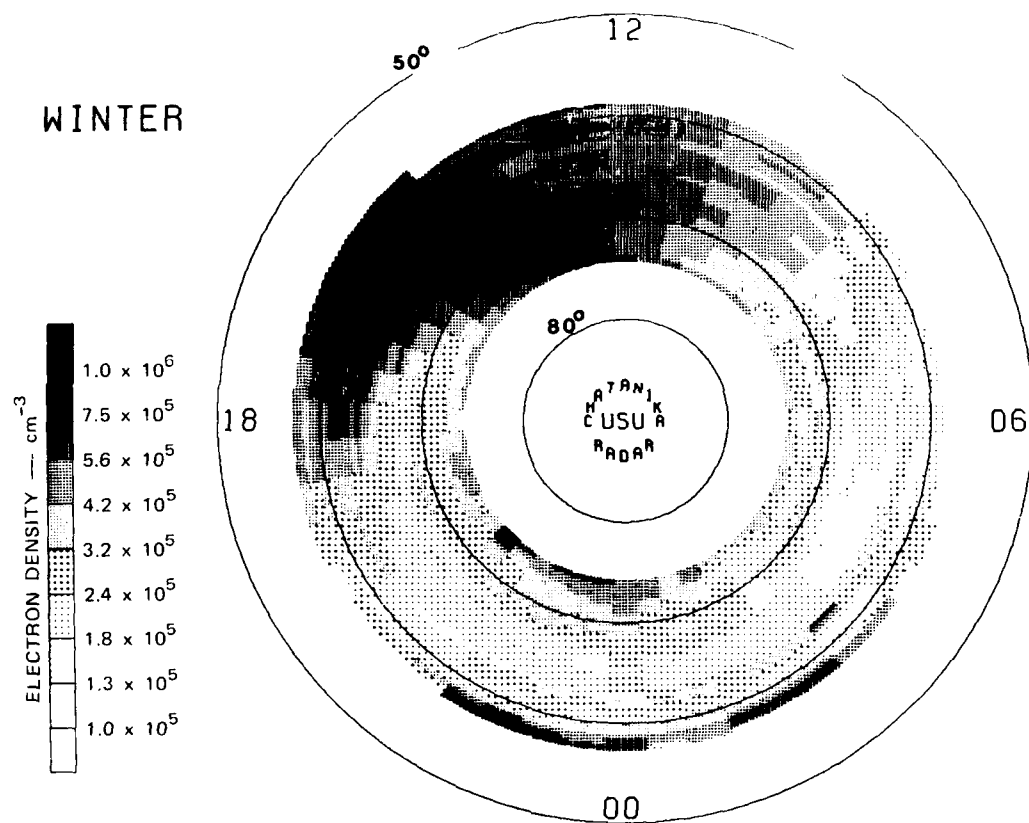
The foregoing discussion suggests that 1000-km parcels of solar-produced plasma, on occasion, are detached from the dayside subauroral ionosphere by imposition of a large, eastward electric field at those latitudes. Those occasions seem likely to correspond to times when the B_z or B_y component of the IMF undergoes large variations. The southward turning of B_z is known to be rapidly followed by (1) expansion of the auroral oval (and associated electric fields) to lower latitudes, (2) development of a two-cell convection pattern (with a region of antisunward flow into the polar cap), and (3) a sizeable increase in convection speed. Once subauroral plasma is drawn into the polar cap, it can be detached from following midlatitude plasma by retracting the eastward electric field imposed at low latitudes; e.g., by a northward turning of B_z . Equatorward (poleward) cleft movement with a southward (northward) turning of B_z has been reported [67, 122, 123]. Other scenarios such as changes in B_y can be envisioned in which variations in electric field pattern also lead to the transport and detachment of subauroral plasma in the polar cap.

The plausibility of the above hypothesis is investigated in following paragraphs. We begin by summarizing the evidence that regions in the lower latitude, dayside ionosphere could become patches in the

polar cap. There have been early reports on the existence of a tongue of enhanced F-layer plasma density extending into the polar cap from the noon sector [116]. But it is not clear from these averaged results whether the tongue represented a steady-state feature, or effects of sporadic-F events. Theoretical and numerical models also have shown that such a tongue could be produced [117, 118, 124]. Although the extent of poleward protrusion and associated plasma densities strongly depend on assumed convection pattern and speeds, most of the modeled plasma in the tongue was solar produced. Particle precipitation in the cusp accounts for ~ 10 percent of the tongue ionization [118].

Incoherent-scatter radar measurements have shed some light on the nature of plasma flow through the cusp region and on whether a plasma tongue is a persistent feature in the polar cap. Foster [125] constructed average morphological patterns of the peak F-region plasma density for winter conditions (10 data sets from December 1978, November 1979, and October 1981) and showed a protracted wedge at latitudes just below the nominal latitude of the cusp region in the postnoon sector. The average winter distribution from Foster [125] is presented in Figure 10. (The average Kp index for the 10 days is 3-.) The wedge of high plasma density ($> 10^6$ el/cm³) seen in the afternoon sector results from prolonged exposure to solar radiation. The magnetic field lines containing the enhanced plasma in Figure 10 were shown by Foster [125] to have convected in sunlight from the morning sector into the afternoon sector, reversing its direction towards the morning sector, before passing through the cusp region. The longitudinal width of the solar-enhanced plasma is on the order of 1000 km, comparable to that of patches. Plasma-density distributions similar to Figure 10 also have been observed by Evans et al. [126] and reproduced in model simulations by Sojka et al. [127]. Kelly and Vickrey [128], using higher-latitude incoherent-scatter radar measurements, showed in a case study that the wedge of enhanced subauroral plasma extends to latitudes slightly more poleward than the field of view of the Chatanika radar (Figure 10), but that it does not protrude as a tongue into the polar cap.

F-REGION PEAK DENSITY



(a) Peak F-region plasma density measured by Chatanika radar.

Figure 10. Evidence that a reservoir or solar-produced plasma exists at subauroral latitudes in the day sector.

Figure 10. Evidence that a reservoir or solar-produced plasma exists at subauroral latitudes in the day sector (concluded).

The usual absence of a plasma tongue seems to be a consequence of a corresponding absence of a localized region of poleward plasma flow into the polar cap around noon (i.e., "throat" region). Foster and Doupnik [129] analyzed Chatanika incoherent-scatter radar measurements to show that the eastward electric field between 70° and 74° invariant latitudes was very weak near noon, increasing to about 15 mV/m in time sectors 2 to 4 hours away from noon. Sondrestrom incoherent-scatter radar measurements also have shown that the convection pattern is predominantly zonal in that sector [130], without evidence of a throat region [131]. The formation of a throat region in the noon sector is now thought to occur only when the B_y component of the IMF is close to zero. Foster and Doupnik [129] showed that under disturbed conditions, the eastward electric field can increase to about 25 mV/m in a two-hour sector near noon. A plasma tongue formed under these conditions. These observations support the hypothesis that the plasma tongue is not a steady-state feature.

The asymmetric distribution of subauroral plasma density about magnetic local noon in Figure 10 also suggests that patch generation might occur as a result of changes in B_y . For example, if B_y changes such that the polar-cap entry region is shifted from the prenoon sector to the postnoon sector, and back again, it is conceivable that the enhanced plasma in the postnoon, subauroral ionosphere would be transported into the polar cap. Whether the throat actually shifts into the postnoon sector is not known. Heelis [131] has drawn a schematic representation of dayside convection as a function of the IMF. In that representation, the throat remains in the prenoon sector regardless of the sign of B_y .

If sporadic-F events, plasma tongues, and patches are not steady-state features, their occurrence is likely to be correlated with the onset of enhanced electric fields, auroral currents, and magnetic activity. Similarly, correlations may also be expected with changes in the B_z and B_y components of the IMF. Hill [112] noted the association of sporadic-F events with the development of auroral currents. Sato and

Rourke [132] derived electric field patterns from ground-based magnetometer data to show that the shape of the plasma tongue was consistent with the presence of antisunward flow over the polar cap. The evidence therefore supports the hypothesis that a patch is indeed solar-produced plasma that has been detached from the dayside subauroral ionosphere by a changing convection pattern and transported into the polar cap.

3.2 BOUNDARY (AND SUBAURORAL) BLOBS.

Boundary blobs are identified by their proximity to the equatorward auroral boundary, and often is interpreted as the poleward wall of the ionospheric trough. Boundary blobs are characterized by their extreme longitudinal extent and temporal persistence. Subauroral blobs resemble boundary blobs but are found in the ionospheric trough region, equatorward of the auroral E layer.

3.2.1 General Properties.

The boundary blob was recently noticed in TEC variations that accompanied scintillation patches. Fremouw et al. [18] noted that a persistent burst of scintillation often occurred at low auroral latitudes, and that it was almost always collocated with a gradient in TEC. (Lizka [8] reported these same features but proposed a different interpretation.) Rino and Owen [20] modelled TEC variations to show that they could be interpreted as latitudinally-narrow (and altitude extended) slabs of enhanced F-region plasma density.

The first unambiguous descriptions of boundary blobs were obtained with incoherent-scatter radars [133, 134]. Examples of boundary blobs observed during radar elevation scans in the magnetic meridian are shown in Figure 11 [3]. Ionospheric features are illustrated by contours of constant plasma density plotted as a function of altitude and north-south distance from the radar. The boundary blob, shown by a shaded region with contours $> 4 \times 10^5 \text{ el/cm}^3$ is situated above the equatorward edge of the auroral E layer. Both boundary blob and auroral E layer are displaced equatorward with time. The persistence of the boundary blob

11 NOVEMBER 1981

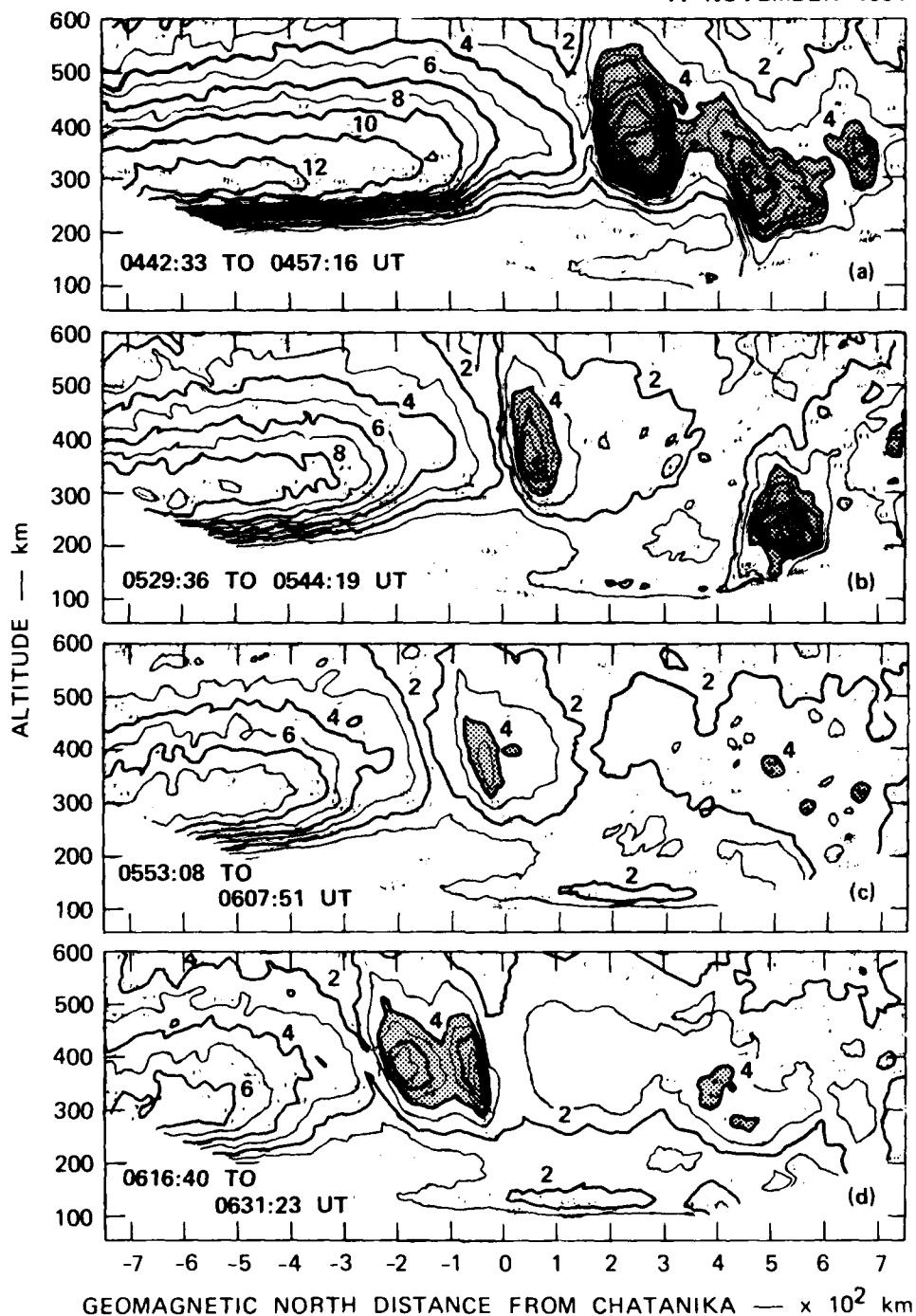


Figure 11. Plasma-density contours measured on 11 November 1981 that show solar-produced F layer, ionospheric trough, boundary blob, and underlying auroral E layer (in order of increasing latitude) [3].

may be contrasted with another shaded region (auroral blob) located about 500 km north of the radar that is no longer apparent after the second radar scan. The stratified F layer equatorward of the boundary blob is produced by solar radiation. (An excellent example of a boundary blob observed in the postmidnight sector was presented by de la Beaujardiere and Heelis [135].)

The remarkable temporal persistence and longitudinal extent of the boundary blob in Figure 11 are illustrated in Figure 12 [3]. The boundary blob was seen in successive elevation scans over a local-time period that spanned more than 12 hours. In contrast, auroral blobs appear intermittently, and because they occur in regions of zonal convection, they are clearly not as extended in east-west direction as boundary blobs. Senior et al. [136] also analyzed this event and showed that the boundary blob and trough were imbedded in a region of a uniform 0 mV/m northward electric field.

The existence of subauroral blobs is clearly evident from Figure 13 [6]. The subauroral blob was observed for more than three hours in local time and was situated as much as four degrees equatorward of the auroral E layer. The subauroral blob also can coexist with a boundary blob. A contour map constructed from plasma densities measured during a radar elevation scan in the midnight sector is presented in Figure 14 [6]. It shows two blobs: the boundary blob at the equatorward edge of the auroral E layer and the subauroral blob 350 km south of the radar.

3.2.2 Source Mechanisms.

The origin of boundary and subauroral blobs can be inferred from topological similarities between patches, boundary blobs, and subauroral blobs; and the unique relationship of the boundary blob to the equatorward auroral boundary. Consider the cross-sectional area (transverse to the geomagnetic field) occupied by boundary and subauroral blobs. If we approximate the dimensions of the boundary blob in Figure 12 to be (1) 100 km in latitudinal width and (2) about 12 hr of local

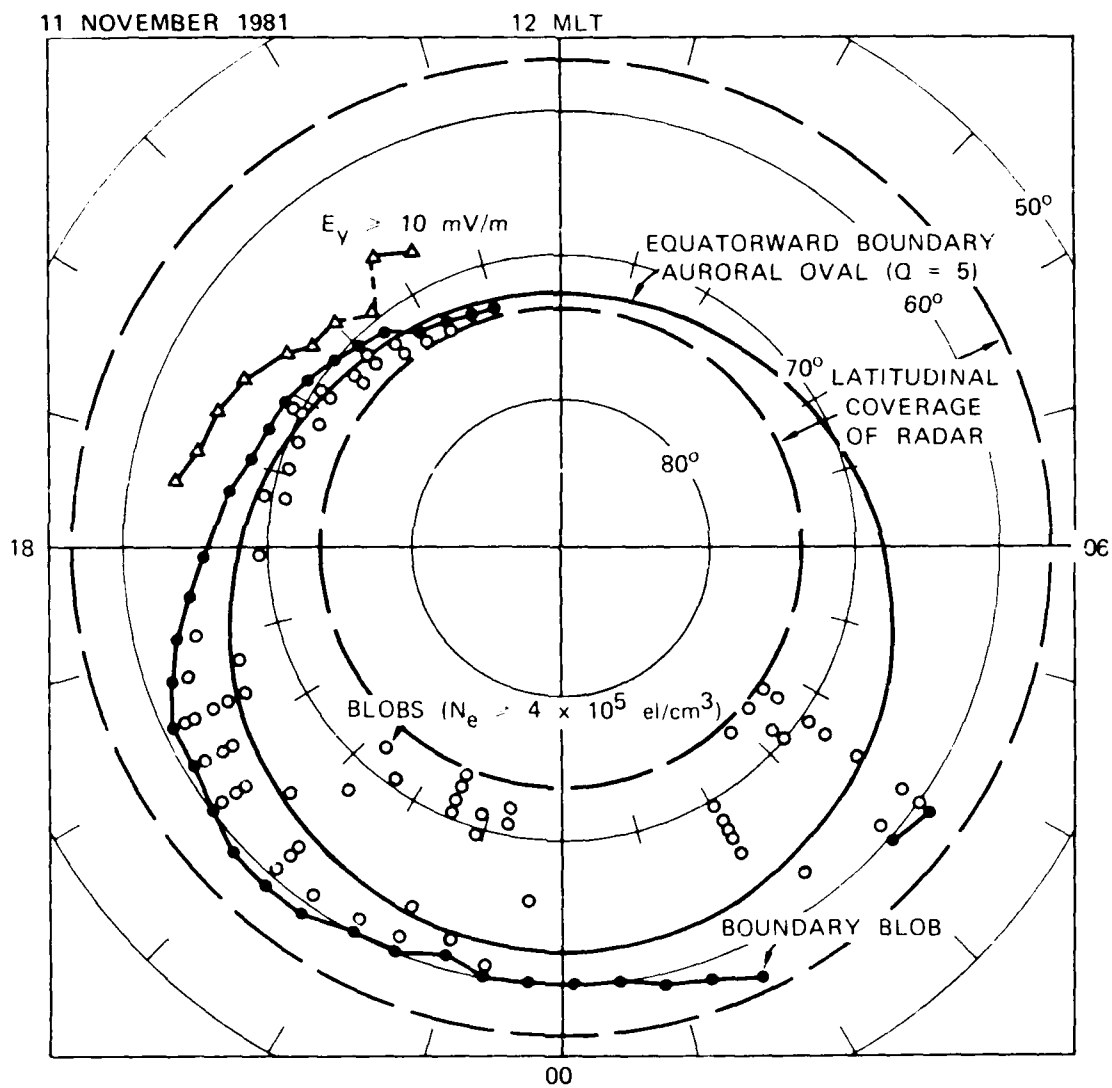


Figure 12. Locations of boundary blob and auroral blobs observed on 11 November 1981 [3].

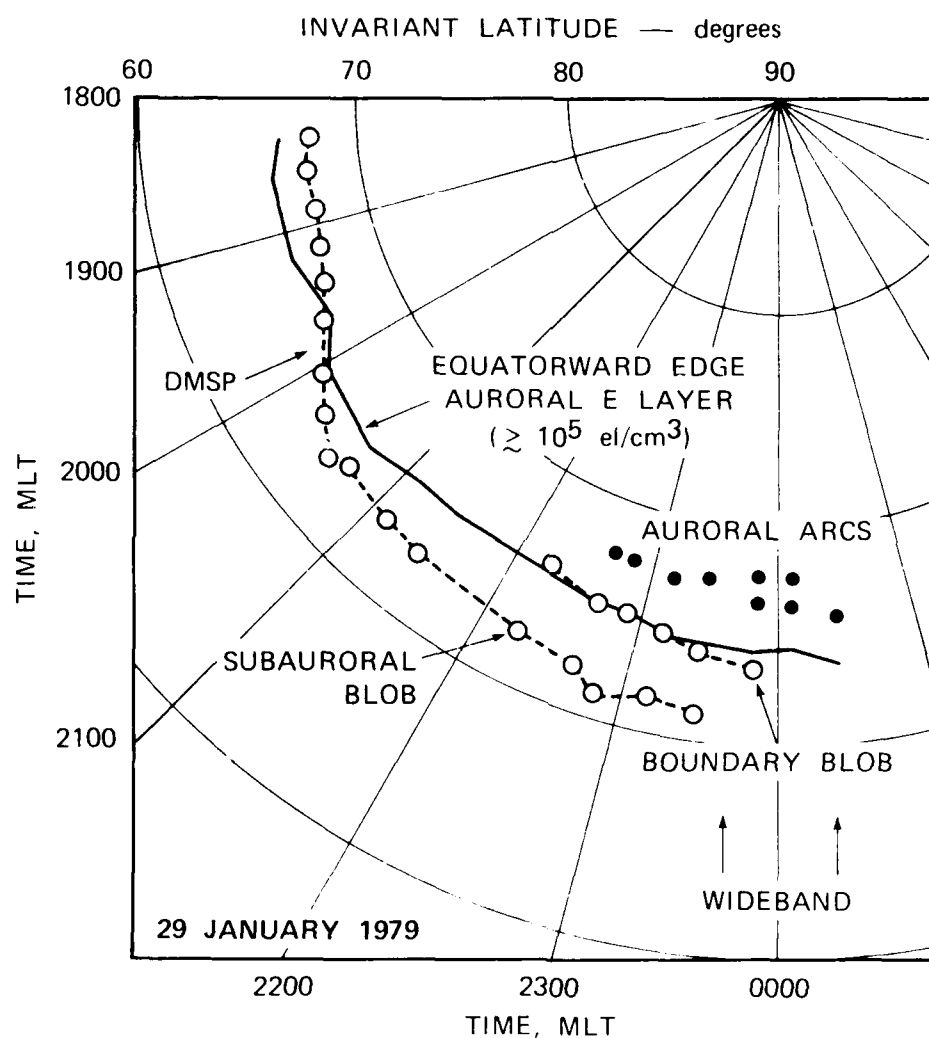


Figure 13. Latitudinal relationship of the boundary and subauroral blobs to the equatorward edge of the auroral E layer 29 January 1979.

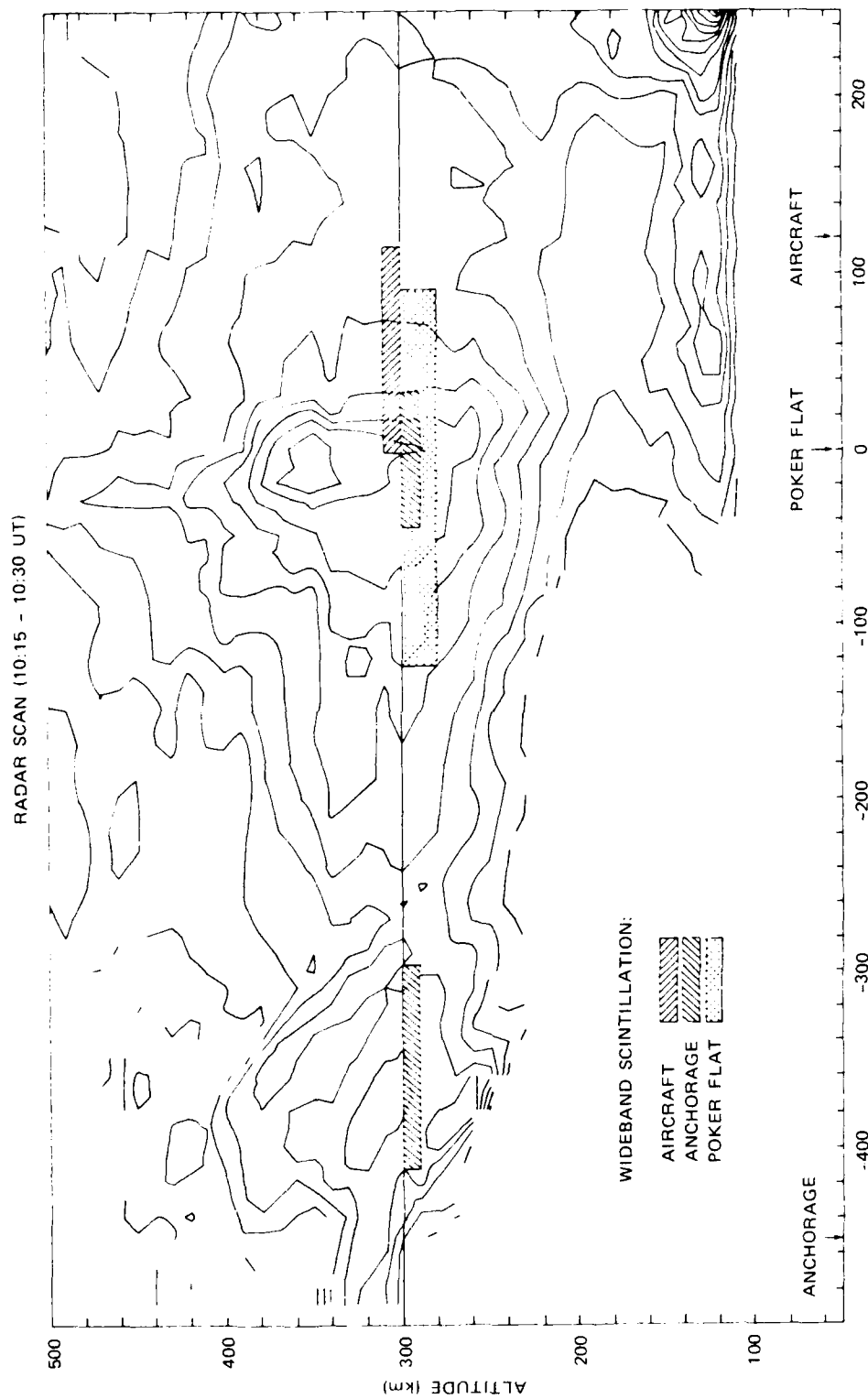


Figure 14. Latitudinal relationships between subauroral blob, boundary blob, and scintillations, 29 January 1979 [6]. Scintillations were measured from three different locations, using beacon transmissions from the polar-orbiting Wideband satellite.

time with a geographical radius equivalent to 25° in latitude, the cross-sectional area of the boundary blob is $8.6 \times 10^5 \text{ km}^2$. In comparison, a polar cap patch described by a circle with 500-km radius has a cross-sectional area of $7.9 \times 10^5 \text{ km}^2$. The surprising similarity of their areas strongly suggests that boundary blobs are simply reconfigured patches. This hypothesis is consistent with the transport of patches from the central polar cap into the midnight auroral sector, and sunward along the equatorward portion of the auroral zone.

Because F-region plasma is virtually incompressible and large-scale structures decay with a time scale of many hours, it is possible to model the patch reconfiguration assuming no plasma loss. Using a two-cell convection model [137], Robinson et al. [4] showed that a circular patch in the polar cap, similar to those observed by Weber et al. [41], convects into the nightside auroral zone and distorts into a latitudinally-confined blob that extends over many degrees of longitude. This reconfiguration process is shown in Figure 15 [4]. The patch (shaded region) is shown at hourly intervals, changing in shape as it enters the midnight sector and becoming highly elongated as it settles into a location of very weak (or zero) east-west electric field.

Experimental evidence supports this concept. Examining the ion-drift velocity measurements made by the Atmospheric Explorer-C satellite as it passed through a boundary blob [135], we find that the east-west electric field was indeed very small equatorward of the boundary blob. This result also is consistent with observations of a uniform northward electric field equatorward of the boundary blob [136]. Only the westward electric-field component must be zero to prevent further equatorward transport of the boundary blob. Another feature associated with patch reconfiguration is the nonalignment of the boundary blob with the convective streamlines. This feature of nonalignment has been verified experimentally [136].

It is important to notice that the patch in Figure 15(a) straddles geomagnetic field lines that circulate in both convection cells. This placement is consistent with the capture of high-density,

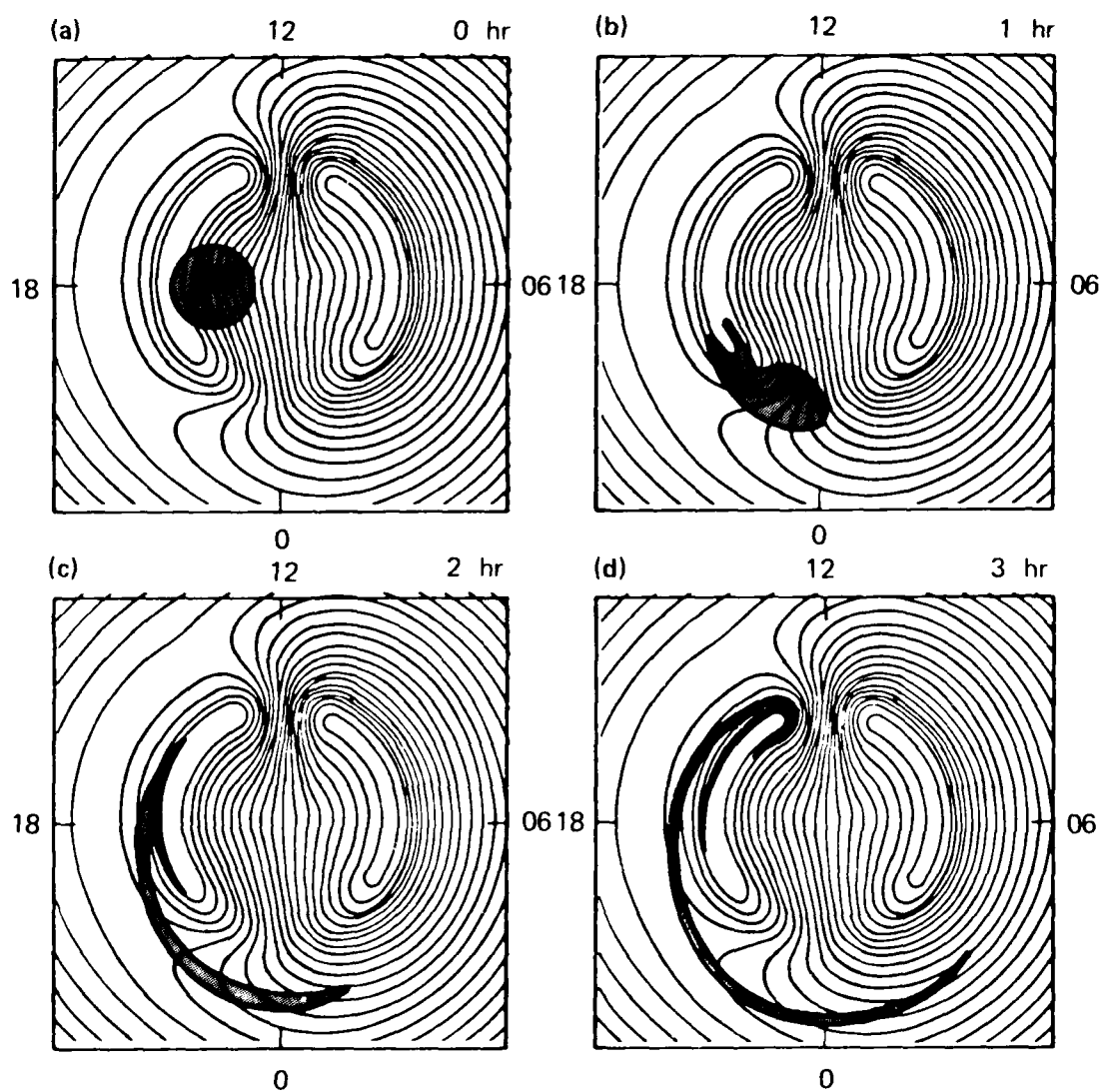


Figure 15. Computer simulation of convective distortion of a circular patch (shaded region in upper left panel) in the polar cap into a form resembling the boundary (or subauroral) blob [4]. The contours are equipotential lines representing magnetospheric convection as seen in the nonrotating frame. The panels represent the time evolution of patch reconfiguration at hourly intervals.

solar-produced plasma (Figure 10) by an expanded convection pattern and transport of that plasma through the cusp region. Also, this placement produces substantial elongation because a portion of the patch plasma is "held" in the premidnight stagnation region while the remainder of the patch is transported sunward in both evening and morning sectors. In this sense, Figure 15(d) is consistent with Figure 12. With the convection pattern in Figure 15, we can envision other forms of patch reconfiguration. A circular patch placed on geomagnetic field lines contained entirely in the morning convection cell, for example, will not become as elongated as that in Figure 15(d). Other shapes therefore seem possible from the patch reconfiguration process.

There also is evidence that soft-particle precipitation contributes to ionization in boundary blobs; how much is less clear. Leitingner et al. [138] showed that TEC enhancements often occurred along the equatorward edge of the diffuse aurora and presented an example (taken during the recovery phase of a magnetic storm) in which 100-eV electron precipitation appeared intense enough ($> 10^{10}$ el/cm²/sr/s/keV) to produce the TEC enhancement. Tanskanen et al. [139] analyzed three events, all occurring during substorm activity, that showed the presence of precipitating electrons with energies ≤ 100 eV and fluxes $> 10^{10}$ el/cm²/sr/keV. Slater et al. [140] showed that the equatorward boundary of the diffuse aurora, as viewed at 630.0 nm, is spatially correlated with low-energy ($E < 1$ keV) electron precipitation and the poleward edge of the ionospheric trough. On the other hand, Weber et al. [6] analyzed near-simultaneous measurements of electron (and proton) precipitation and the plasma density in a boundary blob and concluded that the precipitation was too weak to account for the observed ionization. These results suggest that precipitation along the equatorward auroral boundary may be intermittent.

In another investigation, Robinson et al. [4] used a simple model to estimate distributions of F-region plasma that might result from several (hypothetical) precipitation patterns, including (1) uniform auroral precipitation, (2) precipitation along the equatorward auroral

boundary, and (3) precipitation in the Harang discontinuity region. They showed that convection speed through precipitation regions determined the final distribution, and that all three patterns mentioned resulted in enhanced plasma densities near the equatorward portion of the auroral zone. Because convection speed is slowest in the Harang discontinuity region, they found that largest enhancements occur there. To support their hypothesis, they presented four data sets that contained large-scale plasma enhancements in the Harang discontinuity region.

Although F-region plasma may be enhanced by particle precipitation in the Harang discontinuity region, the dominant plasma enhancements found in the midnight sector seems to be reconfigured patches rather than precipitation-produced structures. Given that patches enter the auroral region in the midnight sector, their intermittent presence is expected in that vicinity. The differentiating feature between the two interpretations is that the first calls for semipermanent "standing" plasma structures [4] while the second suggests transient, convecting features. That is, if precipitation is the dominant source, plasma structures in the Harang discontinuity region should become more evident with increasing geomagnetic activity. On the other hand, convecting features should occur independently of ongoing geomagnetic activity. We note that enhanced plasma densities are not seen in the midnight sector in Figure 10 when the average Kp index was 3-. In comparison, the average Kp index for the four data sets presented in Robinson et al. [4] is 2+. Although the evidence is not totally convincing, it seems to favor patch reconfiguration as the dominant source of boundary and sub-auroral blobs.

Boundary blobs therefore are convection dominated, and their common occurrence along the equatorward auroral boundary is consistent with the presence of a negligible westward electric field equatorward of the diffuse aurora under ambient nighttime conditions. If the latitudinal gradient of the westward electric field is steep poleward of the equatorward auroral boundary, we might expect multiple boundary blobs to

stack up near the equatorward electric field limit. (An example of two boundary blobs is seen in the bottom panel of Figure 11.)

The existence of subauroral blobs is consistent with the convective nature of boundary blobs and the enhancement of the westward electric field in the midnight sector following the southward turning of B_z and during subsequent substorm activity [141-145]. The region of enhanced westward electric field expands with the auroral oval during substorm growth and expansive phases, resulting in the equatorward transport of the boundary blob. During substorm recovery phase, the auroral oval retreats poleward toward its ambient latitude. The boundary blob, however, remains at the lowest latitude reached during substorm penetration because an eastward electric field does not develop during the recovery phase. In other words, the equatorward transport of F-region plasma in the midnight sector is irreversible.

This hypothesis of subauroral blob "production" by the transient appearance of a substorm-related westward electric field can be tested by using the dependence of the equatorward edge of the diffuse aurora on geomagnetic Kp index [69]. Using the midnight-sector data in Figure 13 as an example, we find that the boundary blob was situated around 64° invariant latitude and the subauroral blob around 62° invariant latitude. The latter location is assumed to represent the latitude of the equatorward auroral boundary during past substorm activity. Using the empirical formula derived by Gussenhoven et al. [69], we compute corresponding Kp indices of 2- and 3-, respectively. On 29 January 1979, the Kp index was 2+ in the midnight sector and ranged from 3 to 3 during the previous six hours. This example, therefore, is in excellent agreement with the proposed mechanism.

Similar conclusions were drawn by Bates et al. [133] about the location of the poleward wall of the ionospheric trough (i.e., boundary blob) relative to discrete visual aurora. They found that the poleward trough wall was located a couple of degrees equatorward of the most equatorward position reached by discrete arcs within the past few hours. (The slight equatorward displacement placed the trough wall near the

diffuse auroral boundary.) Mikkelsen [146] also found that the poleward trough wall moves equatorward with the auroral E layer during substorm expansion, but that the F-layer plasma does not retreat poleward during recovery phase. The "fossil" theory of F-region troughs, proposed by Evans et al. [126], also is based on a similar concept.

3.3 SUN-ALIGNED ARCS, AURORAL BLOBS, AND LOCALIZED DEPLETIONS.

Little is known about sun-aligned arcs. They are usually aligned with the noon-midnight meridian and are found in the polar cap under quiet geomagnetic conditions ($B_z > 0$). Coordinated particle measurements from the DMSP-F4 satellite with optical measurements from Thule, Greenland have shown that subvisual arcs viewed at 630.0 nm are spatially coincident with precipitating fluxes of low-energy (< 500 eV) electrons [147]. These intense fluxes (often approaching 10^{10} el/cm²/s/sr) appear to be identical with "polar showers" [148], which also occur in the polar cap when $B_z > 0$ [149-151]. Enhanced plasma densities are associated with these sun-aligned arcs, suggesting direct production by the soft-particle precipitation. Buchau et al. [39] reported peak plasma densities in sun-aligned arcs of $\leq 10^6$ el/cm³, a fourfold increase above the background F layer. Carlson et al. [152] found that plasma densities in sun-aligned arcs were enhanced above the background by about a factor of three, from 0.5 to 1.5×10^5 el/cm³. The maximum plasma densities appear to have a solar cycle dependence. They also found that sun-aligned arcs are associated with velocity shears.

Little is also known about auroral blobs. They are observed in the auroral oval (Figure 11) and appear to be restricted in longitudinal extent (Figure 12), at least compared to the boundary blob [3]. The distribution shown in Figure 12 suggests that they might favor the night sector. As with the large-scale plasma structures found in the midnight sector by Robinson et al. [4], we cannot ignore the likelihood that sun-aligned arcs also enter the midnight auroral oval with the development of antisunward convection. Sun-aligned arcs, being polar-cap features, are likely to pass through the Harang discontinuity region and settle near

the equatorward auroral boundary. Whether auroral blobs and sun-aligned arcs are related is not known.

Besides sun-aligned arcs, there is evidence for other sources of auroral blobs. Case studies have been reported of auroral blobs occurring near the poleward auroral boundary as well within the auroral oval [123, 153, 154]. Figure 16 is an example of a blob found along the poleward auroral boundary in the postnoon sector [154]. The top panel displays contours of plasma density constructed from Sondrestrom incoherent-scatter radar measurements. The plasma-density enhancement, defined here by the shaded region ($> 2 \times 10^5$ el/cm³), is seen to be skewed, being situated 20 km north of the radar (74° invariant latitude) at 250-km altitude and perhaps 60 km north of the radar at 200-km altitude. (The skew is real; the plasma density measurements have been rearranged so that the geomagnetic field lines are vertical in the figure.) The downward protrusion of the blob below 200 km altitude can be interpreted in terms of ongoing (and localized) particle precipitation. The bottom panel shows that the localized precipitation was associated with the gradient in the northward electric field component (i.e., where $\nabla \cdot \underline{E}_1 < 0$), at the velocity reversal region usually associated with the polar cap boundary. Although overhead radar measurements of the electric field are extremely error sensitive, the apparent presence of a weak westward electric field component is consistent with plasma production at the velocity reversal and a slow equatorward transport of the new ionization to the location of the observed blob (at > 200 km altitude). Because plasma drift is predominantly zonal, ionization buildup continues on a given magnetic flux tube until it leaves the $\nabla \cdot \underline{E}_1 < 0$ (or precipitation) region. Upward transport implied by the shape of the blob in Figure 16 is also expected in this region of both frictional and particle heating [153]. (Related blob observations by Foster et al. [123] and Kofman and Wickwar [153] also were made in the postnoon sector.)

Although auroral blobs have been observed in the nightside auroral zone, the systematics of their occurrence have yet to be determined. When derived, it is possible that their morphology will be consistent

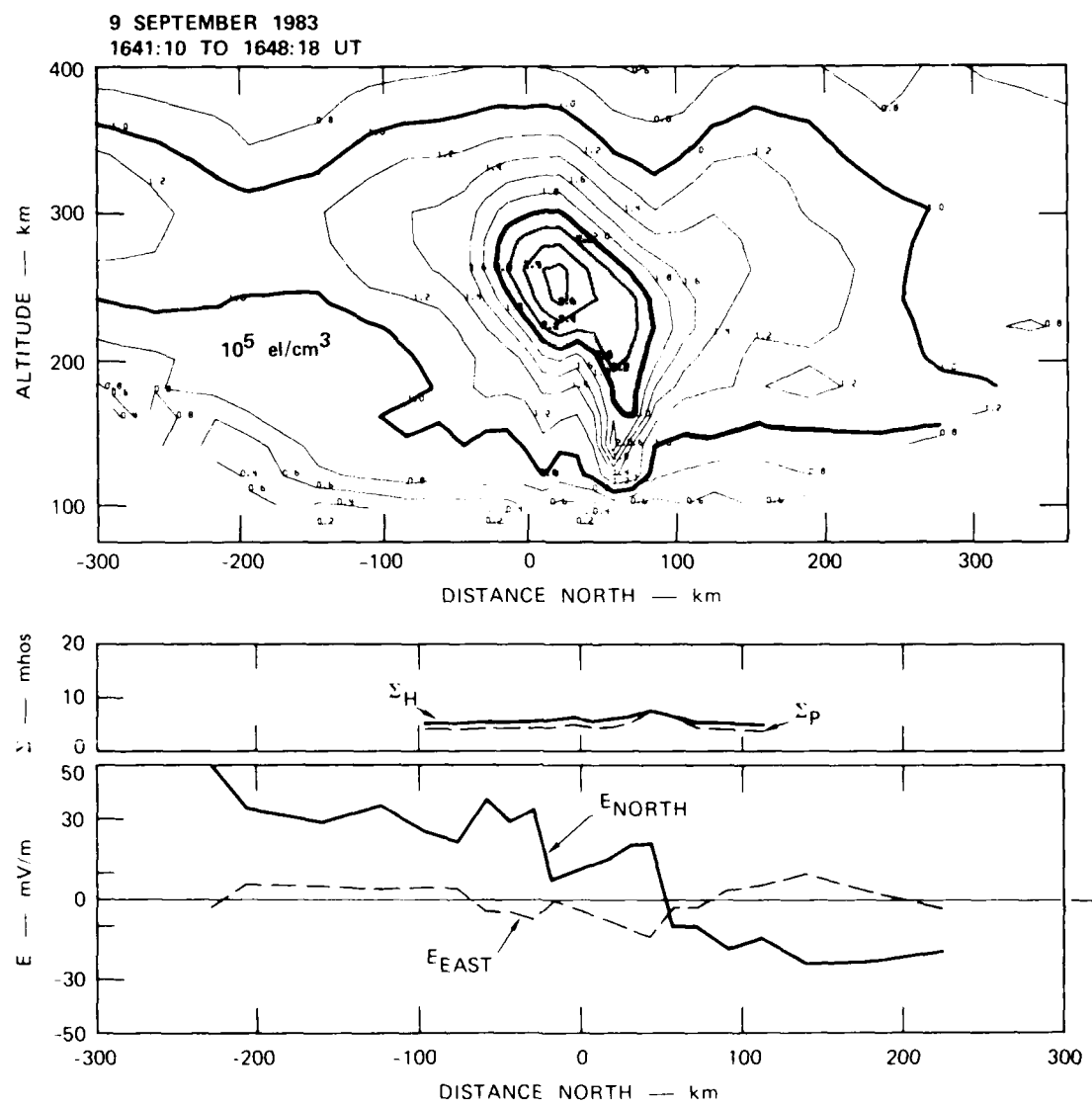


Figure 16. Example of an auroral blob situated along the polar-cap boundary, 9 September 1983 [54]. The corresponding latitudinal distributions of ionospheric conductances and the electric field are shown in the bottom panels.

with that for suprathermal electron bursts reported by Johnstone and Winningham [155]. These events are characterized by intense fluxes ($\sim 10^{10}$ el/cm²/sr/keV/s) of low-energy (≤ 100 eV) electrons. (The primary question is whether their observed duration of several seconds is long enough to produce detectable ionization.) Suprathermal electron bursts are found on either side of the region of discrete auroral arcs and, hence, in the poleward portion of the auroral oval. East-west electric fields, of course, would redistribute in latitude any blobs that might be produced.

Case studies also have shown that the F-layer plasma density can be locally depleted near the poleward auroral boundary, probably as a result of aeronomical changes produced by large electric fields [59]. Large, localized electric fields along the polar cap boundary have been reported [135, 156, 157].

3.4 PARTICLE SOURCE.

There seems to be some disagreement in the open literature about whether soft-particle precipitation is capable of producing blobs. Kelley et al. [36] presented a convincing example in which in situ measured variations in plasma density (by rocket) in the F region closely tracked variations in total energy flux associated with precipitating electrons. Those results are presented in Figure 17. Sojka and Schunk [158] concluded from numerical computations using a theoretical model that a blob with a few times 10^5 el/cm³ peak plasma density could be produced readily in the auroral F layer; therefore, blobs should be frequently observed in the auroral ionosphere. Other results supporting this thesis have been presented [48, 59]. On the other hand, Weber et al. [6] in a case study concluded that electron precipitation did not appear responsible for direct production of the observed blobs. Other theoretical computer models of the polar ionosphere showed that typical soft precipitation events do not rapidly produce F-region ionization [159, 160].

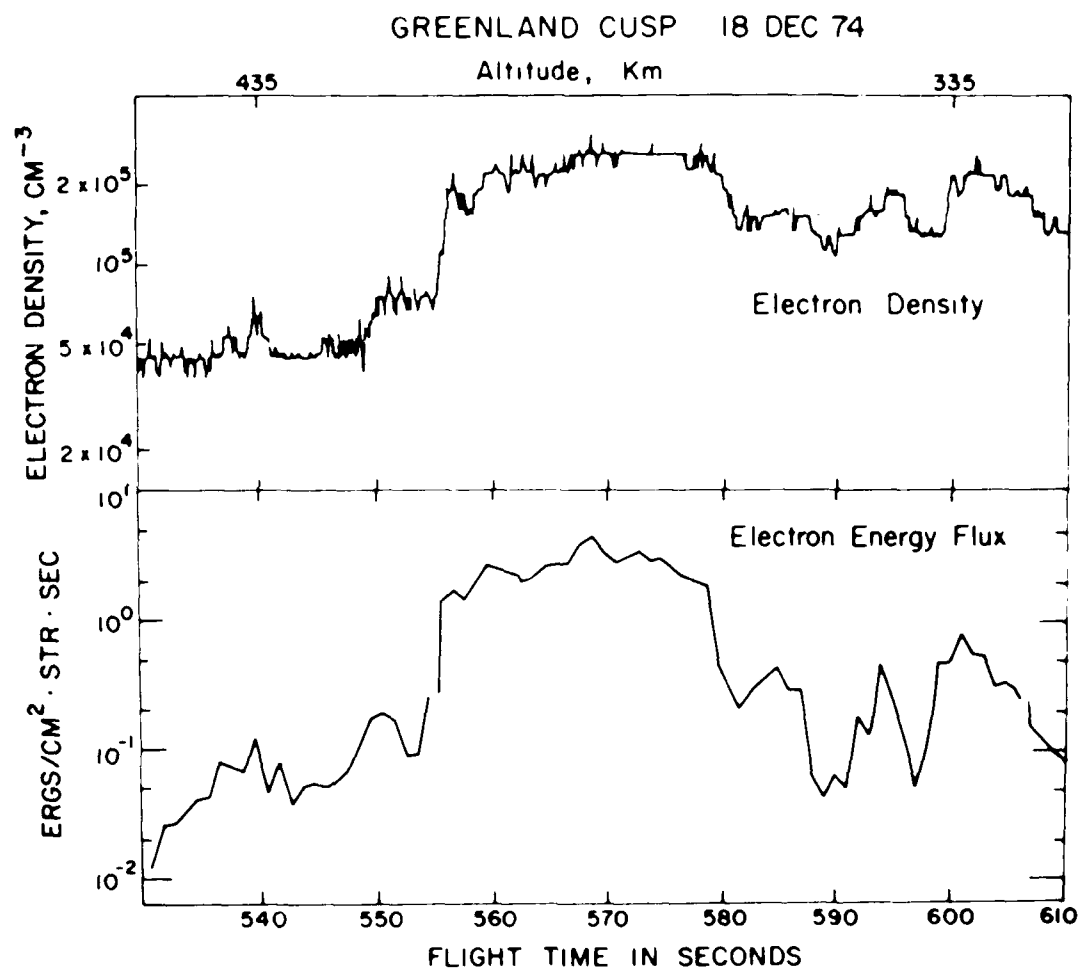


Figure 17. Rocket measurements in the dayside cusp showing high correlation between electron precipitation and associated F-region plasma density [36].

In an attempt to clarify some of the disagreement, we have plotted in Figure 18 various electron spectra that are representative of auroral precipitation events. As a reference, we have included the electron spectrum from Reasoner and Chappell [161] which has been used by several investigators in their model ionization computations [160, 162]. That spectrum is representative of the center of inverted-V events, and as seen in Figure 18, is similar to that for the diffuse aurora [163]. (Numerous other examples of plasma-sheet particle spectra have been compiled by Hones et al. [164].) The differential number flux is about 10^8 el/cm²/s/sr/keV at 100 eV for that reference spectrum.

There are at least three types of precipitation events with low-energy electron fluxes that are more than two orders of magnitude greater than the reference spectrum. Two types are shown in Figure 18. Fairly well known are cusp electrons whose range of spectral shapes are contained within the shaded region [165]. The differential fluxes around 100 eV approach 10^{10} el/cm²/s/sr/keV. The other type is localized precipitation found in the poleward portion of the auroral oval during substorm activity [139]. (Similar spectra are found in suprathermal electron precipitation events [155].) A third type is localized precipitation along the equatorward boundary of the auroral oval, also occurring during substorm activity [139]. This last type is not unlike cusp electrons, with peak differential fluxes near 100 eV of about 10^{10} el/cm²/s/sr/keV.

We note that the model spectrum used by Roble and Rees [159], labeled soft/night in Figure 18, is similar to that for cusp electrons. The results of their calculations are presented in Figure 19. The ionization rate is seen to reach a steady state within 10 s. The plasma-density buildup, however, is very slow at F-region altitudes. While the plasma density at 200-km altitude reaches equilibrium in 20 min, the plasma-density buildup at 300 km begins to become noticeable at 100 s and is still increasing at 1000 s. From Figure 19, we estimate an increase of about 1.5×10^5 el/cm³ in about 20 min. These results are consistent with the measurements presented in Figure 17 but cannot explain peak plasma densities in excess of 10^6 el/cm³.

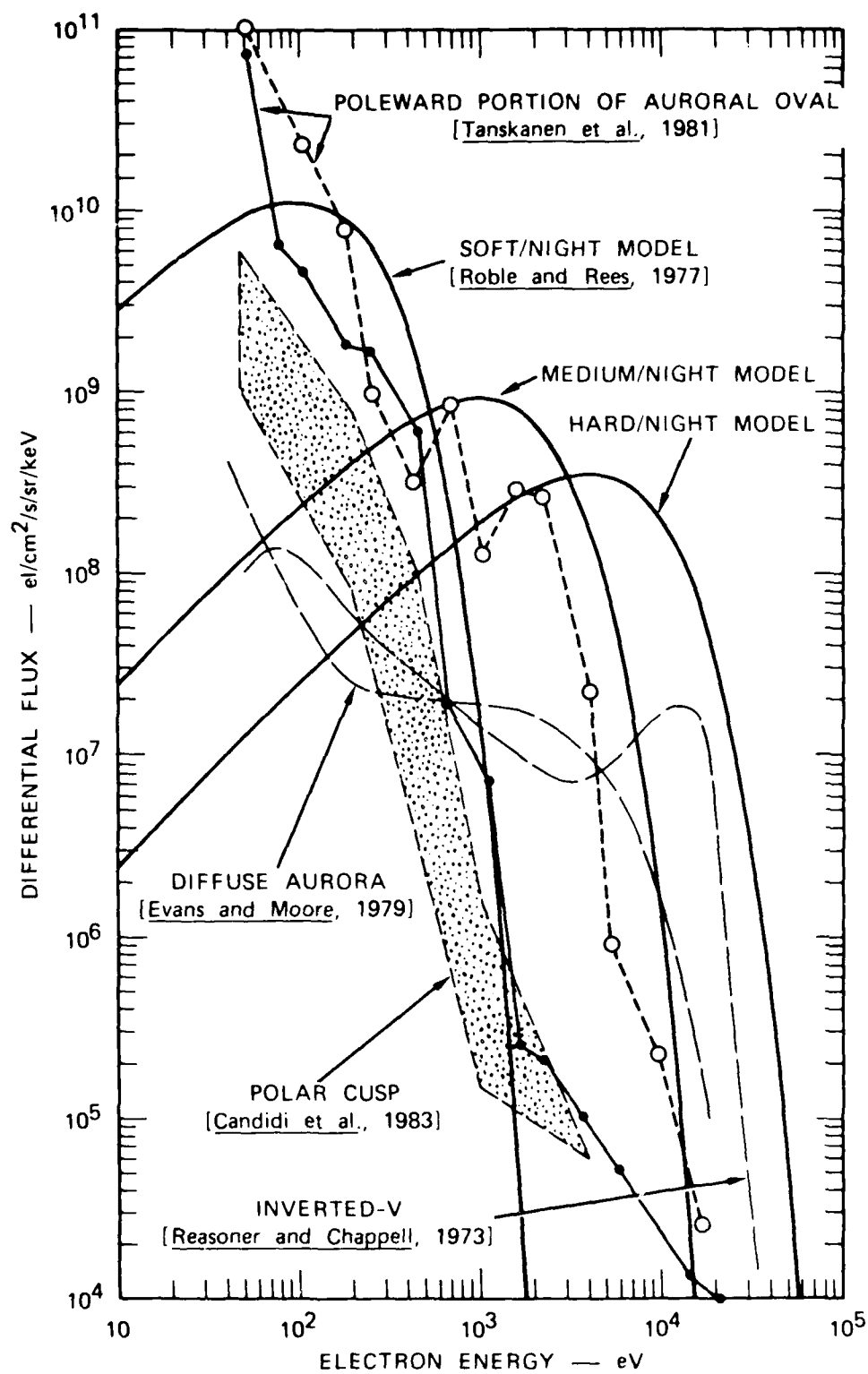
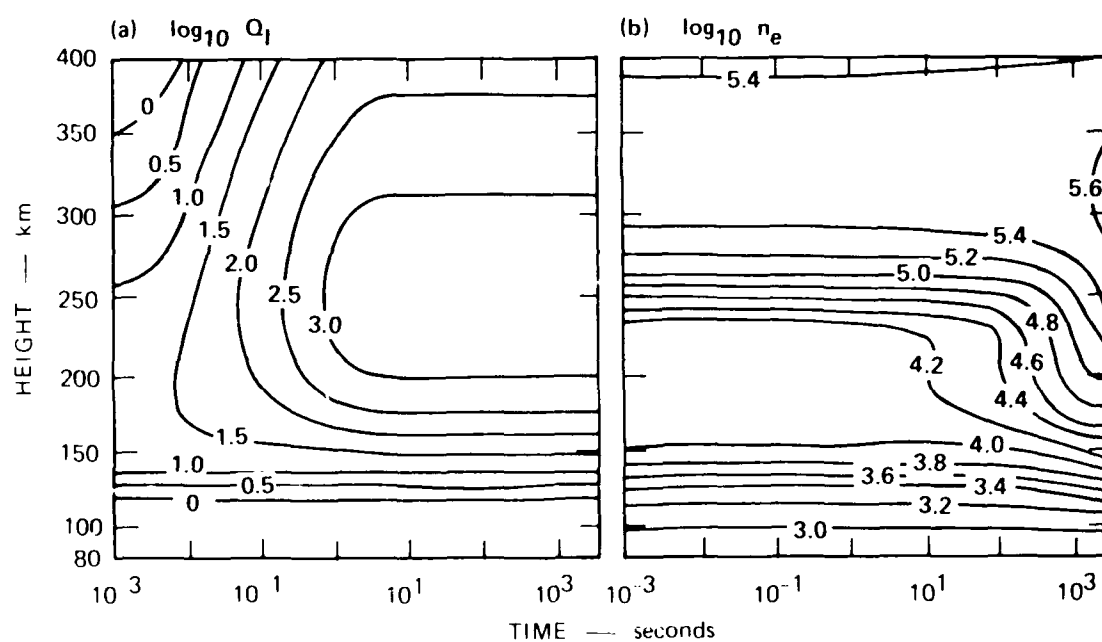


Figure 18. Typical electron spectra for different auroral precipitation events.



[Source: Roble and Rees, (1977)]

Figure 19. Computer simulation of the ionospheric response to the soft/night model electron flux shown in Figure 18. The ionization rate ($\text{cm}^{-3}\text{s}^{-1}$) is shown in the left panel, and the plasma density (el/cm^3) is shown in the right panel [159].

Additional evidence exists in incoherent-scatter radar data that suggests particle-produced ionization rates in the F region can be a few times faster than predicted by the model computations of Roble and Rees [159]. (Observations of faster ionization rates, of course, are consistent with observations of larger soft-particle fluxes [139]. Examples of auroral blobs obtained with the Chatanika incoherent-scatter radar are presented in Figure 20. First, note that all blobs in the two panels extend upward from the E layer into the F layer. The presence of enhanced plasma density below 200-km altitude indicates ongoing precipitation. The blobs are seen to extend up to altitudes in excess of 350 km suggesting either rapid upward transport of ionization produced below, or in situ production. The feature of interest is that some of the blobs are not aligned with the magnetic field lines while others are. Those that are not aligned with magnetic field line (dotted lines) are closely aligned with a radar line of sight. (The best example is seen in the left panel.) This alignment with the radar line of sight can be interpreted in terms of an ionization production rate that is more rapid than the radar-beam scan time. In other words, blobs are being produced more rapidly than the scan time of the radar. If this interpretation is correct, particle precipitation events of this kind appear capable of producing auroral blobs with peak plasma densities of $3 \times 10^5 \text{ el/cm}^3$ in less than a minute.

In cases in which direct blob production does not appear possible from the associated particle flux, we suggest the possibility of "spatial resonance." That is, if the plasma convects with the speed and direction of the particle source, it is possible to continue ionization production on a magnetic field line longer than if the field line convected through the source region. An example of such a situation is presented in Figure 16.

The result of this evaluation is that blobs with peak plasma densities of up to $3 \times 10^5 \text{ el/cm}^3$ can be produced within a few minutes by observed levels of soft-particle precipitation. Further ionization enhancement is possible through a spatial resonance mechanism.

1 MARCH 1982

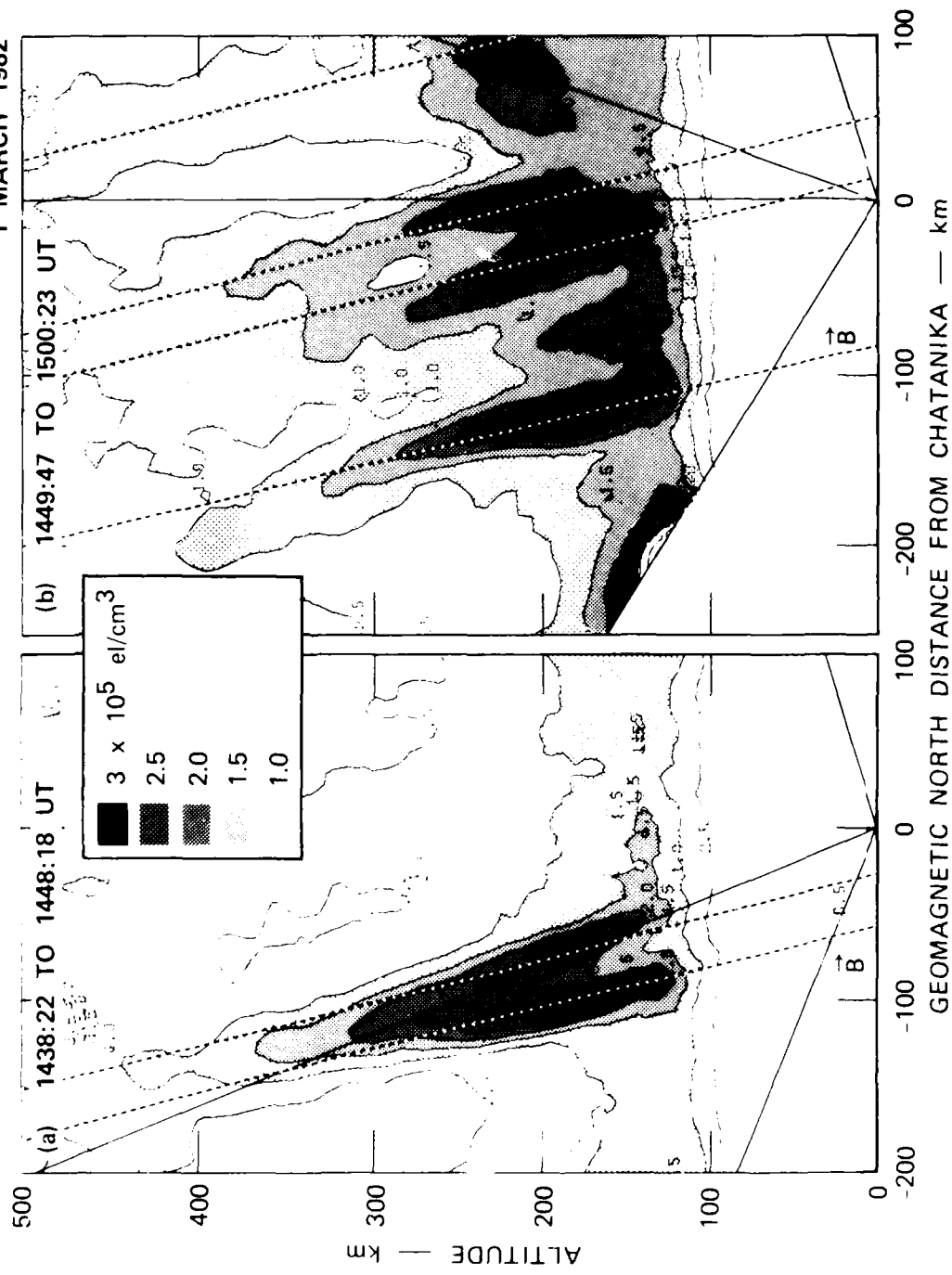


Figure 20. Evidence for rapid ionization in the F region by discrete electron precipitation.

Part of the confusion and disagreement appears to have originated in attempts to account for plasma densities within boundary (and subauroral) blobs. These blobs appear to be solar produced and, therefore, should be compared to peak plasma densities in the dayside subauroral ionosphere. With this distinction, we arrive at a unified framework describing sources of large-scale plasma structure.

3.5 RELATIONSHIP TO SMALLER-SCALE IRREGULARITIES.

The phenomenology of large-scale plasma structure resembles that of smaller-scale irregularities. The winter polar cap appears to be populated with two types of structures, sun-aligned arcs ($B_z > 0$) and patches ($B_z < 0$). Strong scintillations are associated with sun-aligned arcs during solar maximum [147], but not during solar minimum [40].

Strong scintillation is also associated with polar cap patches, as seen in Figure 8. Variations in TEC (lower panel) closely follow those in scintillation intensity (S_4) measured at 1.2 GHz using GPS satellite transmissions (upper panel). Most measurements of this kind indicate that km-scale irregularities populate the entire patch structure during solar maximum, with a tendency for enhanced irregularities to occur along trailing edges of patches [41]. Much weaker scintillations are found during solar minimum, again occurring throughout the entire patch with stronger irregularities near the trailing edge [40, 42].

A similar correspondence between smaller-scale irregularities and large-scale plasma structure is found in the auroral oval: (1) the equatorward irregularity-source region with boundary blobs (and perhaps, subauroral blobs), and (2) the poleward irregularity-source region with auroral blobs and localized plasma depletions. The spatial collocation of scintillation patches with both a boundary blob and a subauroral blob is seen in Figure 14. Although a similar example is not available to illustrate the spatial collocation along the poleward auroral boundary, we have shown that both the poleward HF curtain (Figure 3) and the auroral blob (Figure 16) occur in a region of sunward convection, i.e., in the auroral oval, not the polar cap. We speculate that the slightly

enhanced irregularities found in the Harang discontinuity region by Clark and Raitt [105] (see Figure 6) and by Basu and Aarons [34] might actually represent the passage of polar-cap structure into the auroral region.

From the foregoing, there is good reason to expect fluid interchange instabilities to play a dominant role in irregularity production by MFTI across a mean horizontal gradient associated with the large-scale plasma structure. We also might argue that the similar morphologies simply indicate the fractional fluctuation in plasma density is actually distributed throughout the polar regions and that the absolute fluctuations in plasma density are determined by the mean plasma density (i.e., the large-scale structure). That this is not the case is demonstrated by additional evidence presented in Section 4.4.

SECTION 4

INTERCHANGE INSTABILITIES

In this section, we review the basic properties of interchange instabilities; then, using experimental evidence, we evaluate their effectiveness in the polar ionosphere. Being interested in the underlying physics, we present analytic forms of the linear growth rate of irregularities to illustrate explicit dependences on physical parameters. All forms have been derived using small-amplitude perturbation analysis. We also discuss results from nonlinear numerical computations to assess whether predictions from linear instability theory remains valid under more realistic conditions. (Readers interested in a more detailed mathematical description are referred to Keskinen and Ossakow [45] and references therein.)

4.1 BASIC THEORY.

4.1.1 $\underline{E} \times \underline{B}$ (Gradient-Drift) Instability.

The $\underline{E} \times \underline{B}$ instability is schematically described in Figure 21. With a plasma density gradient directed in the x direction and an applied electric field in the y direction, the geometry is unstable to development of polarization electric fields. The positive feedback loop operates as follows. When a perturbation pattern is imposed on the plasma-density contours, the pattern associated with the ions drift to the right in the "Pedersen" direction (represented by the solid curve) leaving the highly-magnetized electrons (dashed curve) behind. The resulting charge separation is accompanied by a polarization electric field, \underline{E}_p . The $\underline{E}_p \times \underline{B}$ motion is in a direction such that the initial perturbation is amplified by moving less-dense plasma further into regions of more-dense plasma, and vice versa. Irregularities, therefore, grow as a result of

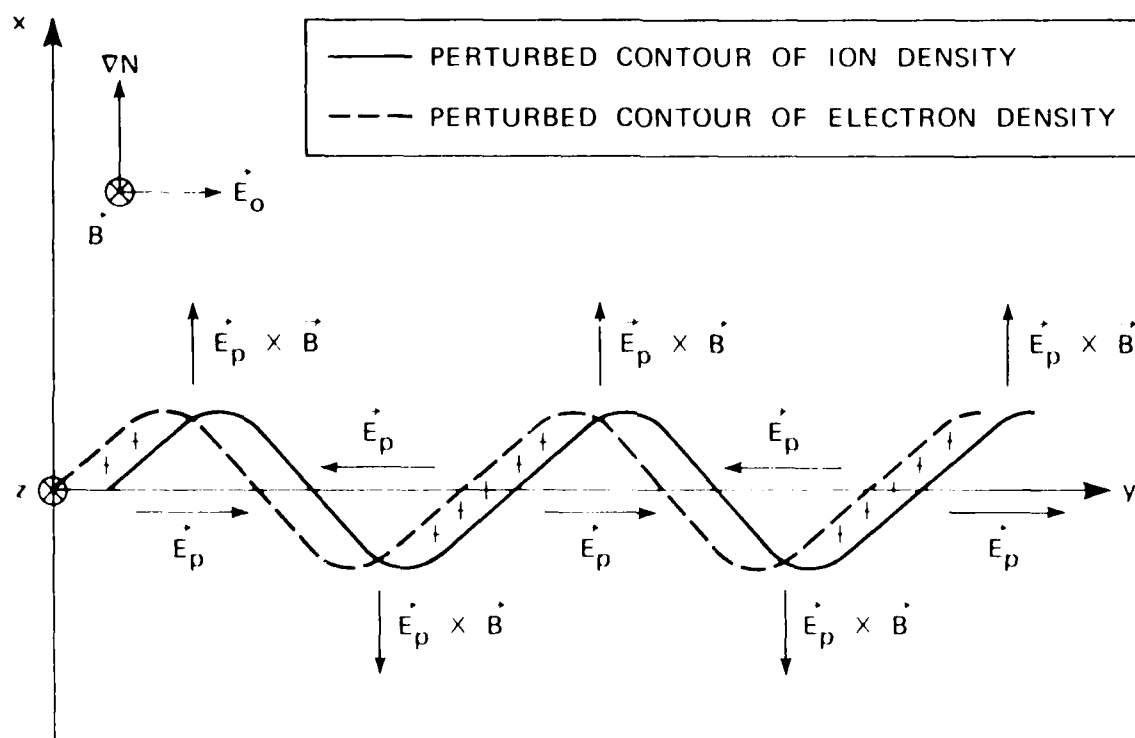


Figure 21. Simplified schematic diagram showing the basic mechanics of the $E \times B$ instability. A Pedersen ion drift (to the right) leads to charge separation and the development of polarization electric fields, E_p . The sense of E_p is to drive $E_p \times B$ motion that further enhances the original plasma perturbation.

MFTI along an existing mean gradient. (The above scenario is assumed to take place in a coordinate system drifting in the positive x direction with a speed E_0/B relative to the neutral gas.)

In the simplest one-dimensional case with $\mathbf{k} \cdot \mathbf{B} = 0$ ("flute" mode), the linear growth rate of the $\mathbf{E} \times \mathbf{B}$ instability [26] is

$$\gamma_0 = \frac{V_0}{L} \quad \omega \ll \nu_{in} \quad (1)$$

where V_0 is the "slip" velocity, i.e., ion drift relative to the neutral gas, L is the gradient scale length, ω is the wave frequency, and ν_{in} is the ion-neutral collision frequency. When there is no neutral wind, V_0 is equal to E_0/B , where E_0 is the applied electric field. The growth rate is derived using a local approximation ($kL \gg 1$), which is equivalent to ignoring the presence of any conducting background plasma. In other words, linear analysis assumes that L remains constant over distances much greater than the wave displacement amplitude; therefore, the wave is unaffected by the presence of any background plasma. Note that there is no wave number ($k = 2\pi/\lambda$) dependence, implying that all irregularity scales are amplified equally.

Ossakow et al. [166] extended collisional theory [Eq. (1)] to include ion-inertial effects. In this high-altitude (or inertial) domain, the linear growth rate is given by

$$\gamma_0 = \left(\frac{V_0 \nu_{in}}{L} \right)^{1/2} \quad \omega \gg \nu_{in}. \quad (2)$$

This form of the growth rate also is independent of k but decreases slowly with altitude through its dependence on $(\nu_{in})^{1/2}$. Equating Eqs.(1) and (2), we find that the crossover altitude occurs where $\nu_{in} = V_0/L$. Ossakow et al. [166] showed that the domains governed by Eqs.(1) and (2) require the conditions $\nu_{in} \gg 4V_0/L$ and $\nu_{in} \ll 4V_0/L$, respectively. For example, if $L = 20$ km and $V_0 = 1$ km/s, the boundary between the two

domains is around 350-km altitude. The $\underline{E} \times \underline{B}$ instability, therefore, is active at all ionospheric altitudes of interest.

In the polar ionosphere, structuring of blobs must be considered as a two-dimensional process [167]. Electric fields (or other drivers) are, in general, oriented at some arbitrary angle with respect to the blob walls; consequently, blobs are likely to have a component of the electric field that is parallel to the wall gradient (in plasma density). The linear growth rates derived using the local approximation and generalized geometry become [168, 169]

$$\gamma = \frac{k_y}{k} \frac{\underline{k} \cdot \underline{V}_o}{kL} \quad \omega \ll v_{in}, \quad (3)$$

and

$$\gamma = \frac{k_y}{k} \left(\frac{\underline{k} \cdot \underline{V}_o v_{in}}{kL} \right)^{1/2} \quad \omega \gg v_{in}. \quad (4)$$

The growth rate remains independent of k and is simply dependent on the drift component and the effective gradient-scale-length, both in the direction of the wave vector.

Huba and Zalesak [170] used nonlocal theory to derive a third form, the linear growth rate in the long wavelength limit ($kL \ll 1$). They showed that the growth rates are identical to Eqs.(1) and (2) if L^{-1} is replaced by

$$k_y \left(\frac{n' - n_b}{n' + n_b} \right) \quad (5)$$

where $n' = n_c + n_b$, and subscripts c and b refer to the cloud (blob) and background, respectively. In this limit, the growth rate is insensitive to the details of the plasma-density gradient and, instead, is proportional to the wave number and the difference in plasma density between blob and background. The appearance of a wave number dependence in the

growth rate indicates that smaller-scale irregularities grow faster than larger-scale irregularities, all other factors being equal.

Consider some of the implications of Eqs.(1) through (5). For irregularities with $\lambda = 1$ km (10 km), the local approximation is valid when $L \gg 160$ m (1.6 km) and the long wavelength approximation applies when $L \ll 160$ m (1.6 km). If we assume that initial value of L produced by auroral and aeronomical processes is typically around 20 km in the high-latitude F layer, the local approximation holds at early times for both 1- and 10-km irregularities. The growth rate, therefore, is identical for both irregularity scales. As the L associated with the walls of large-scale plasma structure decreases (a result of the $\underline{E} \times \underline{B}$ instability) to a length much shorter than 1.6 km, the growth rate of 10-km irregularities enters the $kL \ll 1$ regime while that for 1-km irregularities remains in the $kL \gg 1$ regime. Recognizing that the growth rate from the long wavelength limit is always much smaller than that from the local approximation, we conclude that the growth at 10-km scales must slow considerably (relative to that at 1-km scales) under these conditions. As L decreases to a length much shorter than 160 m, the growth rate of 1-km irregularities also enters the $kL \ll 1$ regime; however, its growth continues to be at least ten times that of 10-km irregularities because of the k dependence. Irregularity growth is predicted by Eqs.(1) through (5) to be much stronger at short wavelengths.

A nonlocal stability analysis applied to a two-dimensional geometry with an arbitrary electric field vector also reveals new effects [168, 171]. If we assume a one-level plasma-cloud model in which the current is divergence-free with no field-aligned current, the electric-field component parallel to the plasma-density gradient becomes inhomogeneous from polarization effects in the Pedersen direction. The result is a velocity shear in plasma drift perpendicular to the gradient in plasma density. The velocity shear produced by the inhomogeneous electric field acts to stabilize the $\underline{E} \times \underline{B}$ instability at short wavelengths. Stability is achieved for a modest value of the electric-field component, i.e., $E_x(x_o) \geq 2kD E_{oy}$ [171] where D is the scale width of the blob wall, and kD

is assumed to be much greater than unity. Huba et al. [168] showed that stabilization is produced by the wave Doppler shift associated with the velocity shear rather than the shear itself. Nonlinear simulations of this effect were presented by Keskinen [169].

4.1.2 Current-Convective Instability.

The current-convective instability [22, 31] is similar to the $\underline{E} \times \underline{B}$ instability in that F-region polarization electric fields are set up to maintain current continuity in the direction perpendicular to the gradient in plasma density. The current-convective instability uses a component of field-aligned current for this purpose. To do so, the wave vector must have a component parallel to the geomagnetic field. The current of interest is $\underline{j}_{\parallel} \cdot \underline{k}$. Once the polarization fields are set up, the $\underline{E}_p \times \underline{B}$ motion is identical to Figure 21.

The linear growth rate including both current-convective and $\underline{E} \times \underline{B}$ instabilities [22] is given by

$$\gamma = \frac{V_o \left(\frac{v_{in}}{\Omega_i} \right) + V_{\parallel} \left(\frac{k_{\parallel}}{k_y} \right)}{L \left[\left(\frac{\Omega_i}{v_{in}} + \frac{\Omega_e}{v_e} \right) \left(\frac{k_{\parallel}}{k_y} \right)^2 + \frac{v_{in}}{\Omega_i} \right]} \quad (6)$$

where V_{\parallel} is the field-aligned drift velocity of electrons relative to ions, and other parameters have their usual meanings. Setting $V_o = 0$, we obtain the linear growth rate for the current-convective instability. The growth rate of the current-convective instability is also independent of k .

If we set $V_{\parallel} = 0$ and $k_{\parallel} = 0$ in Eq. (6), we recover the maximum linear growth rate, γ_o , for the $\underline{E} \times \underline{B}$ instability [Eq. (1)]. From Eq. (6), we see that the effective velocities for the $\underline{E} \times \underline{B}$ and current-convective instabilities are $V_o(v_{in}/\Omega_i)$ and $V_{\parallel}(k_{\parallel}/k_y)$, with each divided by the factor enclosed by square brackets in the denominator. Maximum growth for the current-convective instability occurs when

$$\frac{k_{\parallel}}{k_y} = \left[\left(\frac{\Omega_i}{v_{in}} \right)^2 + \frac{\Omega_e \Omega_i}{v_e v_{in}} \right]^{-1/2} \quad (7)$$

At 350-to-400-km altitude, $k_{\parallel}/k_y \sim 7 \times 10^{-5}$ and $v_{in}/\Omega_i \sim 10^{-4}$. The two velocities, therefore, require comparable values for a given growth rate.

Linear theory for the current-convective instability also has been extended to include the long-wavelength limit [172] and velocity-shear stabilization [173]. Huba [172] showed that in the $kL \ll 1$ regime the growth rate is identical to Eq. (6) with Eq. (5) substituted in place of L^{-1} . Both extensions to linear theory include the collisional and inertial domains.

Although Eq. (6) states that comparable velocities are needed to drive the current-convective and $\mathbf{E} \times \mathbf{B}$ instabilities, a serious difficulty arises because V_{\parallel} refers to field-aligned current carried by the thermal plasma. (The presence of an electron precipitation current has negligible effect on the current-convective growth rate [174].) For the auroral zone, this situation is believed to occur principally in downward field-aligned current regions. The maximum value for the large-scale current density (averaged over several degrees of latitude) is about $2 \mu\text{A}/\text{m}^2$ in the morning "Region 1" sector (0700 to 0800 MLT), and about $1 \mu\text{A}/\text{m}^2$ in the premidnight "Region 2" sector (2100 to 2300 MLT) [175]. (These statistically-averaged values were obtained for Kp values between 2- and 4+.) If the field-aligned current density is $1 \mu\text{A}/\text{m}^2$, the plasma density must be about $6 \times 10^3 \text{ el}/\text{cm}^3$ or less to allow a parallel drift velocity of 1 km/s. Because plasma density in the F layer is about 100 times that value, we expect the parallel drift velocity to be smaller by the same factor, or about 10 m/s.

Larger current densities, however, have been observed in more localized regions. Bythrow et al. [176], for example, have reported an extraordinary case in which the downward current density was $94 \mu\text{A}/\text{m}^2$ in the evening sector. These results suggest that the large-scale field-aligned current systems reported by Iijima and Potemra [175] do not

contribute substantially to irregularity production by the current-convective instability. It is conceivable, however, that more localized, downward field-aligned currents (such as those associated with auroral arcs) might effectively drive the current-convective instability. However, the effect of a finite current-channel width is to reduce its growth rate [177]. To make matters worse, Huba and Chaturvedi [178] showed that the finite extent of blobs along geomagnetic field lines also acts to strongly damp the instability.

Keskinen and Ossakow [23, 24] extended earlier results [179] by using a two-sided slab model to simulate the latitudinal cross-section of an F-region blob. They ignored all inertial terms, assumed a gradient scale length of 20 km and a field-aligned current of $1 \mu\text{A}/\text{m}^2$. The two nonlinear simulations differed only in their grid size; earlier results were appropriate for the wavelength range from 3 to 100 km, and the latter for 0.1 to 1 km. In these simulations, elongated structure developed in (north-south) directions parallel to the mean gradient, indicating that the nonlinear mode coupling effects suggested by Chaturvedi and Ossakow [180] do not produce east-west (orthogonally) oriented sheets. Keskinen and Ossakow [23] suggested that east-west aligned sheets may develop from a secondary $\underline{E} \times \underline{B}$ instability acting on the walls of north-south aligned primary sheets. Keskinen and Ossakow [24] presented simulations of this cascade process using a simplified model.

4.2 EFFECTS OF BACKGROUND PLASMA.

4.2.1 Basic Considerations.

Both irregularity generation by interchange instabilities and irregularity decay through cross-field diffusion are controlled by charge separation and the development of a polarization (or ambipolar) electric field. This polarization electric field, in turn, is affected by (1) the presence of a background plasma, and (2) the effects of electron dynamics along geomagnetic field lines. When considering interchange instabilities, we cannot ignore the presence of other ionospheric layers (not to

mention the magnetosphere). The F-region blob (or cloud) may be considered as being imbedded in a background F layer, as well as being electrically coupled to the E layer (and magnetosphere) by highly conducting magnetic field lines. Coupling occurs through equipotential mapping of transverse electric fields and the high mobility of electrons along geomagnetic field lines.

The primary effects of a background plasma on interchange instabilities can be characterized in terms of two ratios involving (1) the Pedersen conductance (i.e., the field-line-integrated Pedersen conductivity, Σ_p) of the cloud and background plasma, and (2) the relative compressibility of cloud and background plasmas. By compressible, we mean that ion density can be changed on a magnetic field line as a result of transverse ion motion. (Charge neutrality is maintained by corresponding electron motion along magnetic field lines.) The ratio of the Pedersen conductances, M , is given by

$$M = \frac{\Sigma_p^b + \Sigma_p^c}{\Sigma_p^b} = 1 + (\Sigma_p^c / \Sigma_p^b) \quad (8)$$

where the superscript c refers to the plasma-density enhancement of interest (blob, cloud, striation), and the superscript b refers to the background plasma.

The relative compressibility of the background plasma, C_r , is defined by the ratio of ion-dynamical parameters

$$C_r = \left(\frac{\Omega}{v} \right)_c / \left(\frac{\Omega}{v} \right)_b \quad (9)$$

Because ion collision frequency decreases exponentially with altitude, the background plasma is considered relatively compressible ($C_r > 1$) if located below the cloud, e.g., in the E layer, and relatively incompressible ($C_r < 1$) if located above the cloud, e.g., in the F layer.

4.2.2 Incompressible Background.

The F layer is usually thought of as an incompressible, conducting background in which blobs are imbedded. In most cases, blobs appear to have a similar altitude profile as that of the background F layer and, therefore, correspond to the case, $C_r = 1$. On the other hand, barium ion clouds deposited at altitudes below the F-layer peak correspond to the case, $C_r < 1$. The primary effects (known as "end shorting") of an incompressible, finite temperature, conducting background are (1) to reduce the polarization electric field that determines the irregularity growth rate, and (2) to decrease the ambipolar electric field that keeps ions from freely diffusing across geomagnetic field lines; hence, end shorting acts to stabilize the $\underline{E} \times \underline{B}$ instability and enhance cross-field diffusion [181-186].

Analytic forms of the linear growth rate for the $\underline{E} \times \underline{B}$ instability containing explicit dependences on the M factor have been derived by various researchers. Francis and Perkins [183] derived a form applicable to patches in the dark polar cap, or to subauroral blobs (i.e., $M \sim 4$, $C_r = 1$). The linear growth rate equation for large k_y is given by

$$\gamma \approx \gamma_0 \left(1 - \frac{1}{M}\right) - \frac{D_{li}}{L^2} \left(1 - \frac{1}{M}\right)^2 + O\left(\frac{1}{k_y^2}\right) \quad (10)$$

where γ_0 is defined by Eq. (1) and

$$D_{li} = \frac{KT_i v_{in}}{\Omega_i^2 m_i}$$

is the cross-field diffusion coefficient for ions, and the last term in Eq. (10) represents the residual from a power series expansion of the more complex, but exact, analytic form. If we allow M to vary, Eq. (10) reduces to Eq. (1) when $M = \infty$ (no background plasma) and cross-field diffusion is ignored. As M approaches unity, the growth rate tends

toward zero. Völk and Haerendel [181] obtained a similar form for the case of no ion diffusion ($D_{li} = 0$). Eq. (10) is also in agreement with the numerical results of Shiau and Simon [182]. Note that $D_{li} \sim 1.5 \text{ m}^2/\text{s}$ at 350-km altitude for typical F-region parameters. This value is to be compared with the classical diffusion coefficient of $0.2 \text{ m}^2/\text{s}$.

The M dependence is also evident in the linear growth rate derived for the long wavelength limit [187]. If we allow plasma densities, n_c and n_b , in Eq. (5) to be replaced by corresponding Pedersen conductances, the linear growth rate for the $kL \ll 1$ regime of the $\underline{E} \times \underline{B}$ instability (in the absence of cross-field diffusion) takes the form

$$\gamma = V_o k_y \left(\frac{M - 1}{M + 1} \right) \quad (11)$$

which is similar to the driving terms in Eq. (10). Note that Eq. (11) is derived using a one-level model [170], and therefore corresponds to the one-dimensional, $C_r = 1$ case.

Zalesak and Huba [187] extended the results of Ossakow and Chaturvedi [188] to show that the total electric field inside a two-dimensional, elliptical cloud takes the form

$$\underline{E} = \underline{E}_o \left(\frac{R + 1}{MR + 1} \right) \quad (12)$$

where \underline{E}_o is the applied, external electric field, and R is the ratio of major to minor axes of the ellipse. The factor in parenthesis in Eq. (12) represents effects of two-dimensional shielding produced by the cloud. Substituting Eq. (12) into Eq. (11), Zalesak and Huba [187] obtained the following functional form for the linear growth rate of a two-dimensional (elliptical) cloud,

$$\gamma = V_o k_y \left(\frac{(M - 1)(R + 1)}{(M + 1)(MR + 1)} \right) \quad (13)$$

The reduction in γ for small M is due to one-dimensional, polarization-shortening effects alone [Eq. (11)], while the fall off in γ for large M is due to two-dimensional shielding alone [Eq. (12)]. Eq. (13), for $R = 1$, is similar in form to those derived by others [189, 190]. The form of Eq. (13) is historically interesting because it appeared to account for the delayed onset (and hence, small growth rates) of striations in barium ion clouds characterized by large M values [187, 189, 190]. (Whether two-dimensional shielding effects actually plays a role in striation development still remains to be investigated.) We show, however, in Section 4.4.2 that high-latitude F-region irregularities are usually characterized by small M values and, therefore, are not strongly affected by two-dimensional shielding effects.

Different characteristics appear when $C_r \ll 1$. For the case $(\Omega/v)_c \gg 1$, and $(kL)^2 \gg 1$, Francis and Perkins [183] derived the following form for the linear growth rate [see their Eq. (27)],

$$\gamma \approx \gamma_0 \left(1 - \frac{1}{M}\right) \left(\frac{k_y}{k}\right)^2 - \frac{1}{M} (D_{li})_c k^2 \quad (14)$$

The approximations used to derive Eq. (14) are most appropriate for a plasma cloud deposited in the nighttime F_1 region. The background plasma, in this case, would be the F_2 layer. Eq. (14) is similar to Eq. (10), except that the diffusive loss term now has a wave number dependence. Cross-field diffusion therefore acts to reduce the growth rate with increasing k .

Vickrey and Kelley [184] estimated the decay rate of kilometer-scale irregularities by cross-field diffusion in the presence of a conducting background. Although their problem statement is for the E layer, their formulation is for an incompressible background. (A passive, uniform background is assumed with no image formation. They argued that images would be suppressed by rapid recombination chemistry in the E layer if the plasma density there is high enough.) Their resultant decay

rate, with appropriate approximations, is identical to the last term in Eq. (14).

Zalesak et al. [186] considered the effects of relative compressibility (C_r) on the $\underline{E} \times \underline{B}$ instability. They used a two-level model, one level for the plasma cloud and the other for a relatively incompressible (i.e., virtually no image formation) background layer with finite temperature. Separate layers were introduced so that different mobilities and temperatures could be assigned to cloud and background plasmas, and hence, C_r could be varied. They showed that the total Pedersen conductance (which controls the strength of polarization electric fields) could be expressed in the form of a diffusion equation where the effective diffusion coefficient is given by

$$D_o \approx \frac{(D_{li})_c}{M} (1 - C_r) \quad (15)$$

For the case of an incompressible background ($C_r \ll 1$), Eq. (15) indicates through comparison with the last term in Eq. (14) that the total Pedersen conductance decays at a similar rate as the irregularities; therefore, the presence of an incompressible background plasma acts to stabilize the $\underline{E} \times \underline{B}$ instability. When C_r is unity, the diffusion of the total Pedersen conductance is zero.

4.2.3 Compressible Background.

The background E layer is characterized by compressibility and rapid recombination chemistry [191]. A principal effect of a plasma inhomogeneity in the F layer is to produce an image in the compressible background plasma. The image forms as a result of Pedersen ion motion in the E layer, driven by the ambipolar electric field that is mapped equipotentially down along magnetic field lines from the F layer. (The ambipolar electric field is a consequence of cross-field diffusion acting on the F-region gradient in plasma density.) The direction of ion motion acts to increase plasma density in the E layer directly beneath the

region of F-region plasma enhancement. Images formed in a compressible background therefore act to increase M . Consequently, in the one-dimensional case, the increase in M results in enhanced irregularity growth rate [183]. This destabilization produced by image formation and increased M is equivalent to having a negative value for the effective diffusion coefficient in Eq. (15) [186].

Recombination chemistry is mentioned here because it acts to suppress the formation of images in the E layer. Vickrey and Kelley [184] showed for a nondriven situation that kilometer-scale images would be suppressed by this process if the E-region plasma density is greater than $\sim 10^5$ el/cm³. Images that do form when the plasma density is lower is thought not to increase the value of M significantly. On this basis, Vickrey and Kelley [184] concluded that image effects could be neglected at kilometer scales. On the other hand, images can grow in spite of recombination at smaller wavelengths [183, 184]. But at smaller scales, there is also the question of how well electric fields map between ionospheric layers.

Heelis et al. [185] considered the time-dependent problem of F-region irregularity decay including effects of cross-field diffusion, image formation, and recombination chemistry. The formation of image structure in E-region ion concentration affects the lifetime of F-layer structure in a scale-size dependent way. At large scale sizes, the decay rate is proportional to k^2 and the ratio of the temperatures in each region. At small scale sizes, it depends on the E-region recombination rate and the temperatures of the two regions but is only very weakly dependent on k . The background E-region plasma density determines the wave number beyond which the structure amplitude decay rate is almost independent of its scale size.

4.3 OTHER CONSIDERATIONS.

The flute approximation, i.e., $\underline{k} \cdot \underline{B} = 0$ is often used in theories of interchange instabilities. Intuitively, it is apparent that the

interchange instability is not driven equally at all ionospheric altitudes. A clear example is the barium ion-cloud with its limited extent along the geomagnetic field. (In this case, the polarization electric field is generated only in the vicinity of the cloud and not at other altitudes.) The effects of instability variations with altitude are sometimes crudely accounted for by averaging the plasma parameters with altitude [185, 186]. But field-line averaging does not account for ionospheric response to a localized perturbation. The altitude variability is properly accounted for by introducing k_{\parallel} effects [192].

Sperling [192] showed that when k_{\parallel} is introduced, the associated, parallel electric fields become electromagnetic in nature. The accompanying mode magnetic fields lie in the direction of the plasma-density gradient, thus altering the basic magnetic-field geometry. The magnetic-field perturbations act to enhance diffusion across the plasma density gradient. These k_{\parallel} effects therefore act to reduce the growth of irregularities and to produce enhanced diffusion effects similar to end shorting through a conducting background plasma.

Sperling et al. [193] showed for a cold plasma cloud (i.e., zero temperature) that the finite parallel length of the cloud favors irregularity growth at short perpendicular wavelengths. Drake et al. [194], however, included finite temperature (as well as k_{\parallel}) effects and found that short wavelengths are stabilized because electrons redistribute themselves parallel to the geomagnetic field to neutralize the charge imbalance set up by the instability. Similar results were obtained numerically by Sperling and Glassman [195]. How these processes affect the spectral characteristics of high-latitude F-region irregularities (e.g., Figure 1) remains to be investigated. We note that the damping of long wavelengths by k_{\parallel} effects reported by Sperling et al. [193] is small for blobs that have parallel dimensions on the order of the F layer.

4.4 EVIDENCE FOR INTERCHANGE PROCESSES.

4.4.1 Large-Scale Plasma Structure.

In addition to patch reconfiguration at the largest scales by the global convection pattern, observations indicate that boundary blobs at least occasionally have east-west structure imposed along their poleward or equatorward walls [3, 5]. Rino et al. [3] presented preliminary results of east-west structure found along what appeared to be the equatorward wall of a longitudinally-extended blob. Using incoherent-scatter radar measurements of the westward electric field and meridional neutral wind, we concluded that the observed east-west structure was consistent with the $\underline{E} \times \underline{B}$ (gradient-drift) instability [23]. Because that data set remains as the only published evidence supporting the role of interchange instabilities operating at these large scales, some clarification seems in order. This is especially true because a more complete analysis has led to different conclusions.

We have reprocessed the same data set (to include temperature-ratio corrections to the incoherent-scatter data), and replotted them as before [3] using contour maps of constant plasma density in planes transverse to the geomagnetic field. The refined results are presented in Figure 22. The three panels display the plasma density distribution at three altitudes. All contain modulations in plasma density that clearly indicate the presence of east-west structure. A key difference between Figure 22 and that in [3] is that we can no longer state that east-west structure occurred only along the equatorward wall of a longitudinally extended blob. From Figure 22, it is possible to infer that the poleward wall was also structured, or that depleted channels extend from the equatorward wall to the poleward wall of an assumed, longitudinally extended blob.

Several additional statements can be made. The east-west structure in Figure 22 appear to be associated with the boundary blob. The boundary blob is seen in the contour plot of a full elevation scan in Figure 23. Its ground distance from the radar is similar to those for

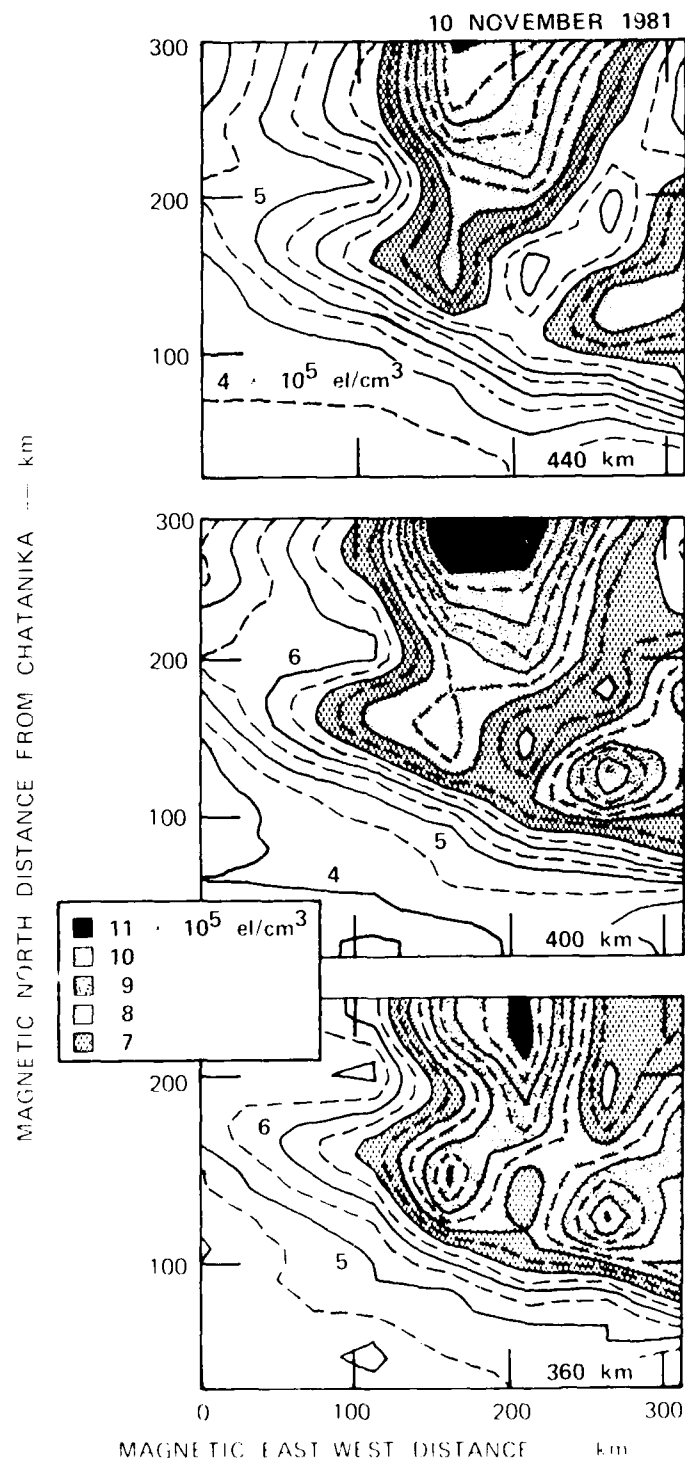


Figure 22 Contour maps of plasma-density distribution (at 360, 400, and 440 km altitudes) that reveal east-west blob structure at large-scale sizes, 10 November 1981.

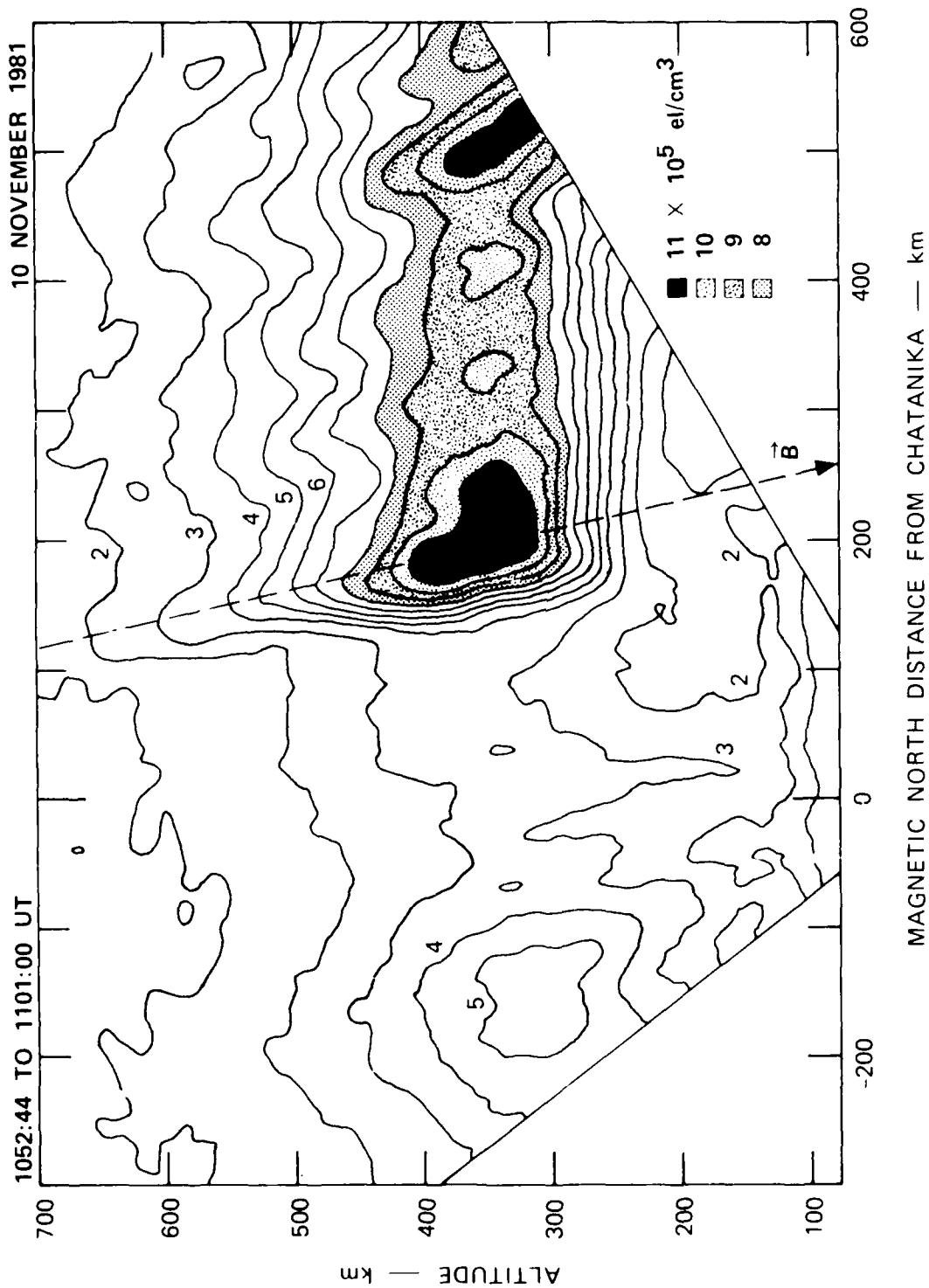


Figure 23. Latitudinal distribution of plasma density associated with east-west structure in Figure 22.

the east-west structure in Figure 22. We also have found that the pattern of meridional plasma drift associated with the plasma-density distributions in Figure 22 is not consistent with the presence of F-region polarization electric fields. A plot of the contours of northward plasma drift is presented in Figure 24, in a format similar to that in Figure 22. To facilitate comparison to the plasma-density distribution, we have superimposed a contour (dashed curve) taken from the center panel of Figure 22. The meridional drift was small in general, but relative velocities were found to be correlated with the plasma-density contour. A region of poleward drift (200 m/s) appears to be associated with a plasma-density enhancement, and a region of equatorward drift (also 200 m/s) with a channel of depleted plasma density. The sense of relative plasma drift is oppositely directed from that expected from polarization electric fields generated by the gradient-drift instability driven by an equatorward-directed neutral wind.

Similar conclusions were drawn from the analysis of another data set by Tsunoda et al. [5]. They performed an experiment similar to that described in [3], except that by using the EISCAT radar facility they were able to obtain vector electric fields (rather than only the line-of-sight velocity) associated with the plasma structure. Their results are reproduced in Figure 25. The plasma density distribution at 300-km altitude is shown in the top panel, and can be compared to corresponding spatial distributions of the ion drift velocity vector (center panel) and the slip velocity (bottom panel). The velocities are described by their magnitude which is given by the contour plots, and by their directions which are represented by arrows at the data points. (The arrows superimposed on the plasma-density contours are those of the slip velocity.) Although large ion velocities were observed in depleted regions relative to enhanced plasma density regions, indicating ongoing structuring by a MFTI process, the slip velocity pattern was not correlated with the plasma-density distribution. From these observations, Tsunoda et al. [5] concluded that while the F-region plasma was being

10 NOVEMBER 1981

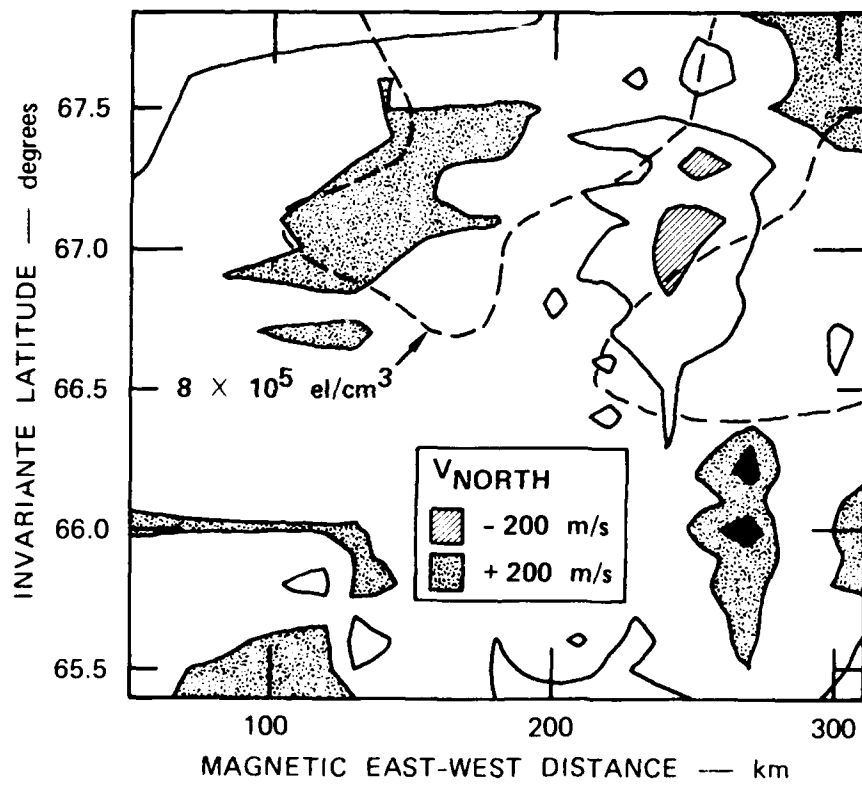


Figure 24. Contour map of the northward velocity component associated with east-west structure in Figure 22.

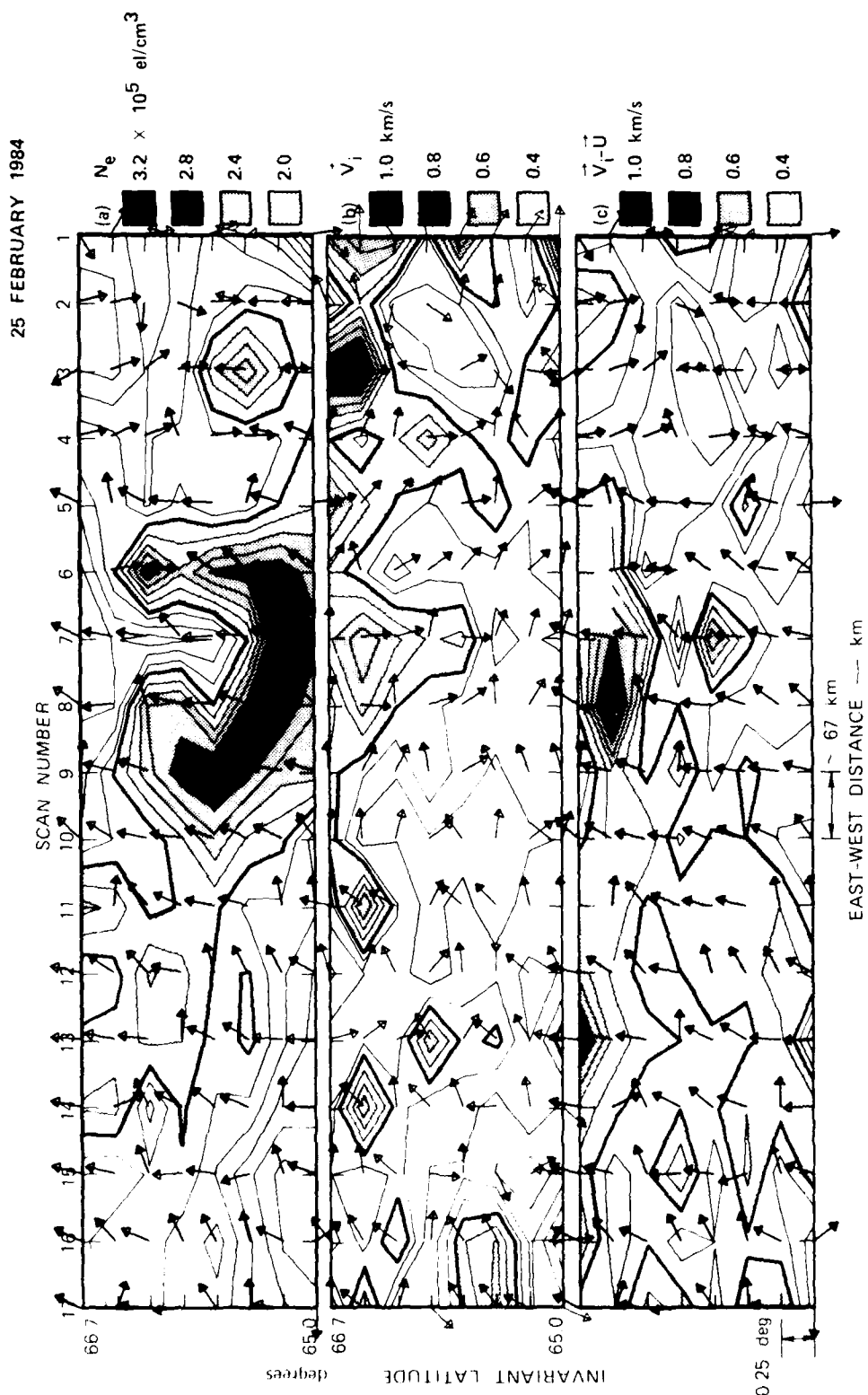


Figure 25. Contour maps of plasma density at 300-km altitude, ion velocity vector, and slip velocity vector, showing the spatial interrelationships, 25 February 1984 [5].

structured, the mechanism was not likely to be the $\underline{E} \times \underline{B}$ instability operating locally at those altitudes.

Although 100-km-scale east-west structure is predicted by $\underline{E} \times \underline{B}$ instability theory [23], observations to date do not support theory. It seems that large-scale structuring by MFTI often is driven by sources of irregular electric fields other than those produced by an F-region interchange instability. Irregular electric fields, presumably mapped from the magnetosphere, have been reported by researchers [103, 196, 197]. Burke et al. [196] presented two examples in S3-2 satellite data of 10-km-scale vortex flow patterns during substorms. The vortices are thought to be produced by the Kelvin-Helmholtz instability in regions of velocity shear and represent another source of irregular electric fields. Spatially-irregular particle precipitation, e.g., during substorms, also could produce E-region polarization electric fields that drive the MFTI process. Highly irregular patterns of E-region Pedersen conductance have been reported by Vickrey et al. [198].

4.4.2 Smaller-Scale Irregularities ($\lambda < 10$ km).

While there is no evidence as yet that large-scale plasma structure is produced by an F-region interchange instability, the evidence strongly favors this process as scale sizes less than 10 km. As discussed briefly in Section 1, observations of burstlike occurrences of scintillation, often in association with F-region blobs, led to initial considerations of interchange instabilities as the dominant irregularity-source mechanism [2, 18-20, 106]. A feature of considerable interest was a localized scintillation enhancement that occurred around midnight, in the magnetic L shell passing through the satellite receiving station (Poker Flat, Alaska). Earlier, Lizka [8] reported similar results obtained at Kiruna, Sweden, which is located at nearly the same invariant latitude as Poker Flat. Rino et al. [19], using spaced-receiver scintillation data, showed that these scintillation patches could be produced by sheetlike irregularities that were oriented along magnetic L shells. While arguing that sheetlike irregularities could produce a geometric

enhancement in scintillations (in the magnetic L shell, as observed), most researchers allowed that at least a portion of the patch amplitude could be a true geophysical enhancement. Referring back to Figure 6, we see that the scintillation patch occurred at the same latitude as the midnight maximum in kilometer-scale irregularities [105]. And, from Figures 3 and 4 we find that the scintillation patch is also collocated with the lower HF backscatter curtain [60].

With researchers noting a correlation between scintillation patches and northward-directed TEC gradients [18, 19], Ossakow and Chaturvedi [22] proposed the current-convective instability (instead of the $\underline{E} \times \underline{B}$ instability) as the source for localized growth of enhanced irregularities. And, to account for the existence of sheetlike irregularities, Chaturvedi and Ossakow [180] suggested a form of nonlinear stabilization of the current-convective instability. Rino and Owen [20] further supported that interpretation by modelling TEC data (from the Wideband satellite) to show that scintillation patches occurred along the equatorward walls of an altitude-extended slabs of enhanced plasma density (i.e., the boundary blob). Data collected from two latitudinally-separated sites were used to distinguish propagation effects from true irregularity enhancements, and to demonstrate that the slab was latitudinally narrow. Vickrey et al. [2] drew similar conclusions in which they included field-aligned currents measured by the TRIAD satellite.

The apparent importance of the current-convective instability, however, has since been questioned. For example, equatorward walls of blobs are not necessarily stable to the $\underline{E} \times \underline{B}$ instability if allowance is made for the presence of a meridional neutral wind [3, 5]. Indeed, the midnight sector is typically characterized by the presence of an equatorward directed neutral wind (see Section 4.3) and a weak westward electric field. Under these conditions, the equatorward wall of blobs can be unstable to the gradient-drift instability. As discussed in Section 4.1.2, field-aligned currents that are larger than observed are needed to produce current-convective growth rates that are competitive with $\underline{E} \times \underline{B}$ growth rates.

The most convincing evidence that the $\underline{E} \times \underline{B}$ instability is operating in the high-latitude F region is seen in data from the ISOPROBE experiment on board the AUREOL-3 satellite [49, 52, 199]. Cerisier et al. [49] showed that short wavelength fluctuations in plasma density and electric field were asymmetrically distributed along the walls of 10-km-scale plasma structure. Clear examples of this preferred distribution are presented in Figure 26. Rapid small-scale fluctuations in the top panel occur along positive (upward sloping with time) gradients in plasma density associated with a quasi-periodic wave structure; note the complete absence of similar fluctuations in negative-gradient regions. More often than not, the smooth gradients are steeper than the gradients underlying the fluctuations. A similar pattern, reversed from left to right, is also seen in the center panel. Both examples are consistent with one-dimensional structuring by the $\underline{E} \times \underline{B}$ instability, e.g., along one side of a boundary blob. Similar conclusions were drawn from Figure 8 in which enhanced scintillations were correlated with the trailing edges of polar-cap patches [42]. These characteristic signatures indicate that gradients are not the sole source of free energy that leads to the observed irregularities. In fact, it is difficult to account for these observations by physical processes other than the $\underline{E} \times \underline{B}$ instability [49].

The less-characteristic fluctuations in the bottom panel of Figure 26 seem to require interpretation either in terms of nonlinear theory or more isotropic, two-dimensional structures. The observation of short-wavelength irregularities on both sides of a 10-km-scale, plasma-density enhancement seen near the left edge of the bottom panel is consistent with measurements made transversely across the "fingers" of a structured barium ion-cloud or blob. The data also are consistent with nonlinear "jetting" through of depletions from one side of the blob to the other [23]. A second burst, seen near the center of the bottom panel, is characterized by large-amplitude fluctuations without the presence of a significant gradient. This observation seems consistent with late-time, nonlinear evolution of the $\underline{E} \times \underline{B}$ instability in which the

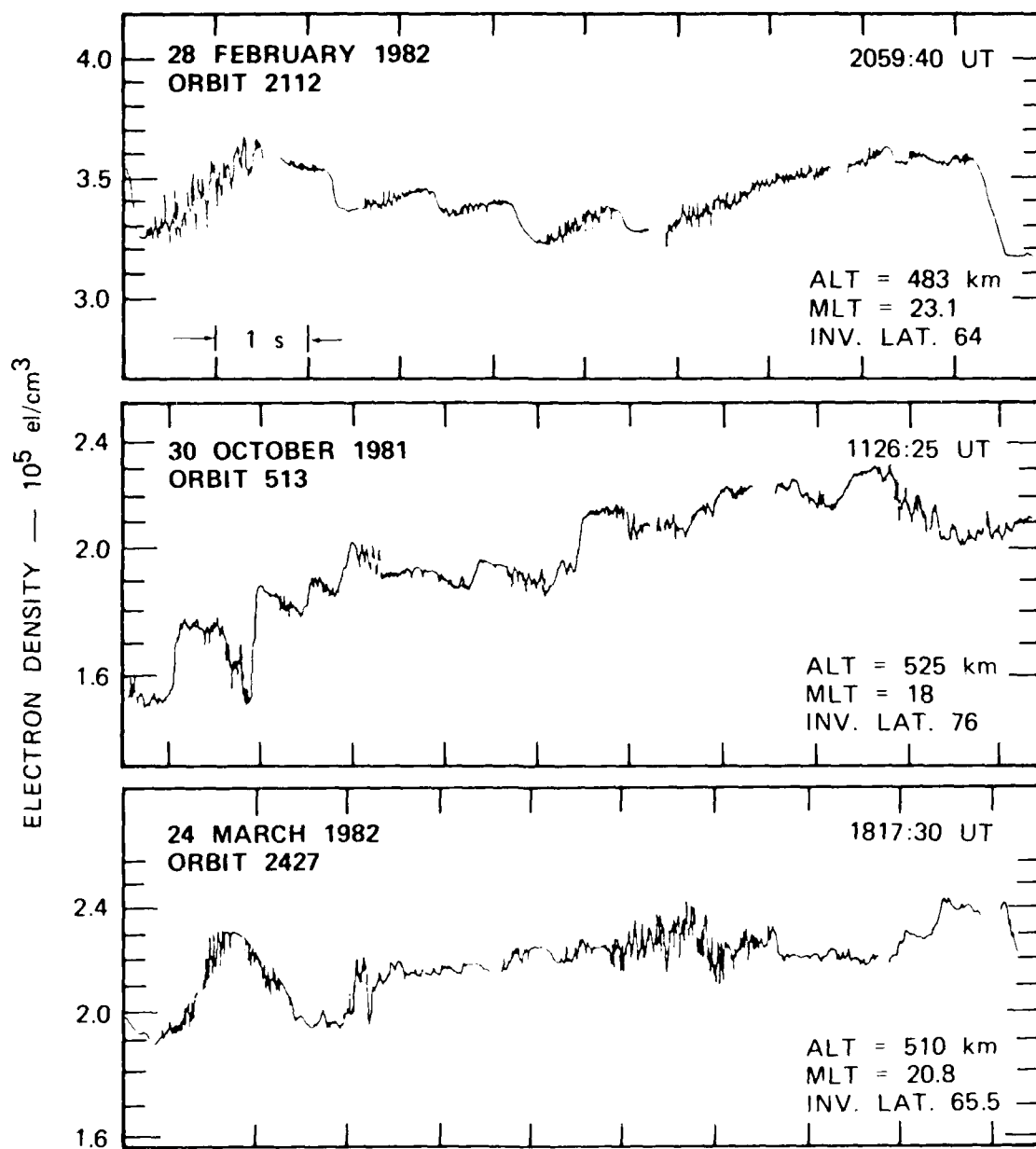


Figure 26. Examples of asymmetric irregularity distributions in relation to mean plasma-density gradients, and the occurrence of 10-km-scale wavelike structures.

original blob has become so structured that evidence of the original large-scale gradient is lost.

While the fine structure in Figure 26 appears accountable by the $\underline{E} \times \underline{B}$ instability, the quasi-periodic plasma variations ($\lambda \sim 10$ km) found in the top two panels of Figure 26 are not necessarily part of the same process unless they represent a preferred scale size. Similar wave-like variations in plasma density with a wavelength close to 15 km have been observed by Hargreaves et al. [200]. Because of its strong periodicity, they attributed the variations to some form of wave activity. Regular signal oscillations with periods from 50 to 500 ms, and lasting up to 100 periods, were reported by Lizka [10]. It is interesting to note that similar-scale vortex patterns in convective flow patterns are observed during substorms [196].

We point out that the morphology of small-scale irregularities of the type in Figure 26 is not known. Most of those reported were found in the midnight sector [49]. But it is not known whether they are distributed at any given time over many degrees of latitude, or whether they are confined to bloblike widths. In comparison, Weber et al. [41] have found strong and structured scintillations (at 250 MHz) to be distributed throughout most of the observed polar cap patches. Although scintillations (which is an integrated measure) would appear more evenly distributed than irregularities measured in situ, those observations must suggest that patches are not smooth structures as implied by a solar ionization source. Instead, there appears to be considerable granularity (perhaps in the form of 10-km-scale blobs, similar to that seen in Figure 26) imbedded within the patch, granularity produced by some kind of seed structure, e.g., particle precipitation or wave activity.

The existence of sheetlike irregularities [19, 57, 85, 201, 202] is consistent with the $\underline{E} \times \underline{B}$ instability. Livingston et al. [202] presented the morphology of irregularity anisotropy (from spaced-receiver diffraction-pattern measurements) found in the midnight sector. Their results, presented in Figure 27, indicate that sheetlike irregularities occur only at latitudes equatorward of 65° , i.e., near the equatorward

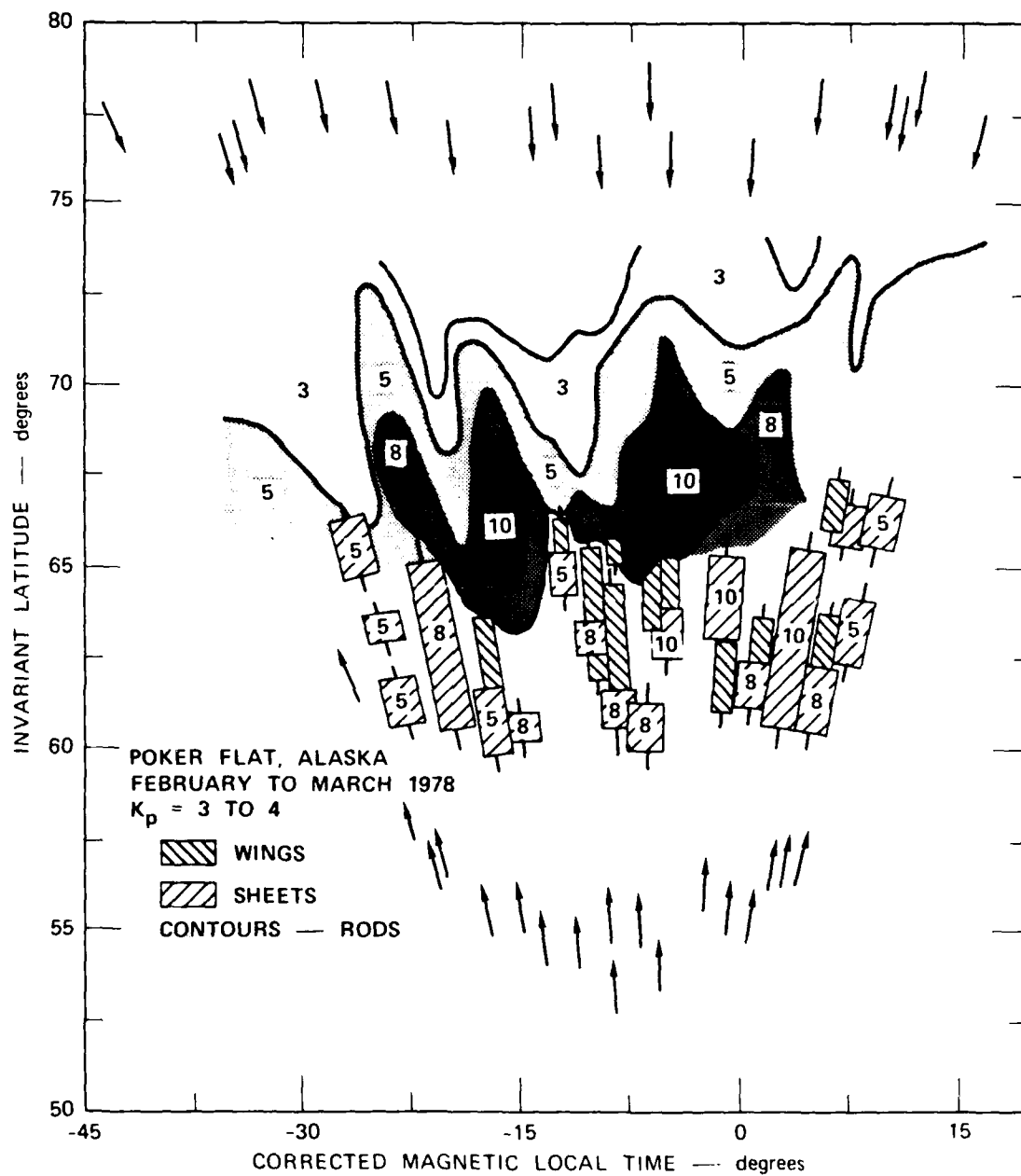


Figure 27. Morphology of irregularity anisotropy determined from spaced-receiver scintillation measurements using the Wideband-satellite-beacon transmissions [202].

boundary of the auroral oval. (Fremouw and Lansinger [85] have shown that irregularities in the trough are rodlike.) Sheet formation by the $\underline{E} \times \underline{B}$ instability in a region of strong zonal convection is consistent with nonlinear numerical simulations [23, 24]; the sheets in these simulations remain aligned with the direction of the slip velocity, as predicted by linear theory. Sheetlike anisotropy also is thought to be a natural consequence of velocity shear such as that occurring on the equatorward edge of the auroral oval [4, 46].

A more quantitative assessment of the effectiveness of the $\underline{E} \times \underline{B}$ instability is to estimate the M value. Typical Pedersen conductances for various types of ionospheric irregularities are listed in Table 1. The Pedersen conductance of blobs range from 0.1 to 1.0 mho, depending on solar activity. This range of conductances corresponds to peak plasma densities from 10^5 el/cm³ to 10^6 el/cm³. If we use the nighttime, midlatitude F layer as a typical background ionosphere (Pedersen conductance of about 0.1 mho), blobs will have M values from 2 to 11. But if we use 5 mhos for the diffuse auroral E layer and add it to the background F layer, we obtain M values ranging from 1.02 to 1.19. The M values become even closer to unity if we consider higher Pedersen conductances for the diffuse auroral E layer or that for auroral arcs. The latter can reach several tens of mhos [210]. On this basis, the irregularity growth rate determined from Eq. (11) or (15) can easily be reduced by a factor of 50 or more in the auroral zone.

The M values of blobs can be compared to those associated with barium ion-clouds, and with plasma bubbles in the nighttime equatorial F layer. A 1-kg barium ion-cloud released at 170 km altitude has a Pedersen conductance of 6 mhos. The M value is then 61 if we use a midlatitude, nighttime F layer, and 2.2 if we have an underlying auroral E layer. A 48-kg barium ion-cloud under the same conditions has M values of 470 and 10, respectively. For midlatitude twilight conditions when most barium clouds are released, the background Pedersen conductance is about 3.5 mhos [183]. Using this value, the corresponding M value is 14.4. Zaesak et al. [211] estimated equivalent M values from 9 to 10^4

Table 1

TYPICAL PEDERSEN CONDUCTANCES (Σ_p)

SOURCE/REGION	FORMULA	Σ_p (mhos)	REFERENCE
F-REGION BLOB	—	~ 0.1 0.1 TO 1.0	<u>Vickrey et al. [1980]</u> <u>Tsunoda [1986]</u> ⁽¹⁾
EQUATORIAL F LAYER (NIGHT)	—	3 TO 7 1 TO 3	<u>Anderson and Mendillo [1983]</u> <u>Hanson et al. [1983]</u>
MIDLATITUDE F LAYER (NIGHT)	—	0.15 TO 0.35	<u>Harper and Walker [1977]</u>
AURORAL E LAYER ⁽²⁾	$\left(\frac{40 E_o}{16 + E_o^2} \right) \Phi^{1/2}$	5 TO 10	<u>Robinson et al. [1986]</u>
SOLAR E LAYER ⁽³⁾	$0.88[S_a \cos \chi]^{1/2}$	8 TO 12	<u>Robinson and Vondrak [1984]</u>
NIGHT E LAYER	—	0.08 TO 0.2 0.02 TO 0.5	<u>Harper and Walker [1977]</u> <u>Hanson et al. [1983]</u>
BARIUM ION CLOUD ⁽⁴⁾ (1 kg)	—	6	<u>McDaniel [1972]</u>
BARIUM ION CLOUD ⁽⁴⁾ (48 kg)	—	47	<u>Linson and Baxter [1979]</u> <u>McDonald et al. [1981]</u>

(1) Unpublished results.

(2) E_o = average energy (keV), Φ = electron energy flux (ergs/cm²/s).

(3) S_a = 10.7-cm solar radio flux (10⁻²² W/m²/Hz adjusted to 1 AU), χ = solar zenith angle.

(4) Reference 170-km Release Altitude.

for equatorial plasma bubbles. These M values suggest that the irregularity growth rates should be much smaller for blobs in the auroral zone than for barium ion-clouds or equatorial plasma bubbles.

The question of whether images form in an auroral E layer has received some attention. Observations of enhanced auroral emissions associated with barium-ion cloud releases [212, 213] appear to be the first tangible evidence of related E-region effects. Stoffregen [212] reported the occurrence of 557.7-nm emissions in a quiet auroral E layer within seconds of barium ion-cloud releases in the F layer and interpreted them in terms of image formation although he allowed for an alternate interpretation in terms of energetic particle precipitation. Jones and Spracklen [214] pointed out that theory predicts significant image formation about a minute after ion-cloud deployment, not within seconds; therefore, the E-region optical anomalies [212] do not represent conclusive evidence for image formation. Other evidence supports this suggestion, at least in terms of enhanced electron precipitation induced by deposition of cold plasma in the F region. Köhn and Page [215] reported changes in the pitch-angle distribution of precipitating electrons in the vicinity of a barium-ion cloud. Kelley et al. [216] also reported enhanced particle precipitation and stimulated waves in association with barium-ion cloud releases. They suggested that parallel wave-electric-fields may produce significant wave-particle interaction effects in the high-latitude ionosphere.

Jones and Spracklen [214] reported phase and amplitude changes in radio signals (between 1.5 and 2.0 MHz) reflected from the E layer during barium-ion cloud releases. They concluded that these radio disturbances must be produced by image effects because their onset time was consistent with the development of ion-cloud striations. Unfortunately, physical parameters could not be extracted from these measurements. It is interesting to note, however, that they did not observe any radio effects associated with the above-described, cloud-induced particle precipitation. More convincing experimental evidence of image formation was reported by Vickrey et al. [217]. Image irregularities were observed

in the valley region (between the E and F layers) in association with equatorial F-layer irregularities. Because these images occurred above the E layer, it does not resolve the question of whether significant images do form in the auroral E layer.

4.4.3 Spectral Characteristics.

The observed spectral characteristics (Section 2.1) appear to be reasonably consistent with those derived analytically from consideration of conservation laws [218] associated with the $\underline{E} \times \underline{B}$ instability and with those obtained from nonlinear numerical computations carried to their saturated states [179, 180, 219]. The one-dimensional spectra were found to be well represented by a power law with a spectral index between unity and 3. Similar results were also obtained for the current-convective instability [23, 24].

Considerable effort has been expended towards explaining the two-component irregularity spectrum (Figure 1) in terms of the $\underline{E} \times \underline{B}$ instability. Two-component spectra (with a break around 800 m) have been observed in equatorial F-region irregularities produced by the collisional Rayleigh-Taylor instability [220]. Barium ion-clouds appear to stop their progressive bifurcation process at a scale size around 200 to 600 m [221, 222]. This so-called "freezing" scale (λ_f) is believed to be associated with the knee in the two-component spectrum. Although this feature appears to be an inherent characteristic of the above phenomena, it only appears to occur in about 25 percent of the high-latitude irregularity spectra. The fact that the knee appears only occasionally and with values around several hundred meters would seem to suggest that it is not a finite gyroradius effect. Although it is tempting to argue on the basis of association alone that this feature is a manifestation of the $\underline{E} \times \underline{B}$ instability, Kelley and Kintner [57] have argued that two-dimensional plasma turbulence also is likely to produce a two-component spectrum with similar spectral indices. In their case, the knee corresponds to the "stirring" scale size.

Besides the two-component spectra described in Section 2.1 [52, 58], there also are other examples of "freezing-type" scales found in high-latitude in situ data. An enlarged portion of the top panel in Figure 26 is reproduced in Figure 28. As noted before, the rapid fluctuations are confined to regions of positive gradients associated with large-amplitude 10-km-scale structure. If we estimate the wavelength of the largest-amplitude fluctuations along the gradient by counting the peaks, we obtain a value close to 350 m. The apparent absence of stronger fluctuations at wavelengths between 350 m and those approaching the 10-km blob size suggests that the fluctuation strength peaks around 350 meters. Although a proper spectral analysis should be performed on the data in Figure 28 to verify this conclusion, it seems apparent that there is a change in spectral form between the 10-km input scale (that associated with the mean gradient) and the dominant small-scale fluctuations with a 350-m wavelength. For the example shown, it seems that the "freezing" scale might correspond to a sharp maximum in irregularity growth rate. On the other hand, the presence of the 10-km-scale blobs (or structure) suggests that they are produced by an independent process.

If the 10-km-scale periodic structure were included in a spectral representation, we envision the appearance of a resonant peak near $\lambda \sim 10$ km with a two-component power-law form at shorter wavelengths. If wavelengths longer than 10 km are not included, the spectral form would be similar to a three-component power law. This form would not be unlike that obtained from scintillation data by Fremouw et al. [57]. (The second break at larger scale sizes reported by Fremouw et al. [57], however, is now believed to represent propagation effects rather than an actual change in the spectral character at long wavelengths [E. J. Fremouw, personal communication].)

A number of researchers have pursued the existence of a preferred k value associated with the maximum irregularity growth rate. The most popular view is that the k dependence imposed on the irregularity growth rate by background plasma effects may contribute to the formation

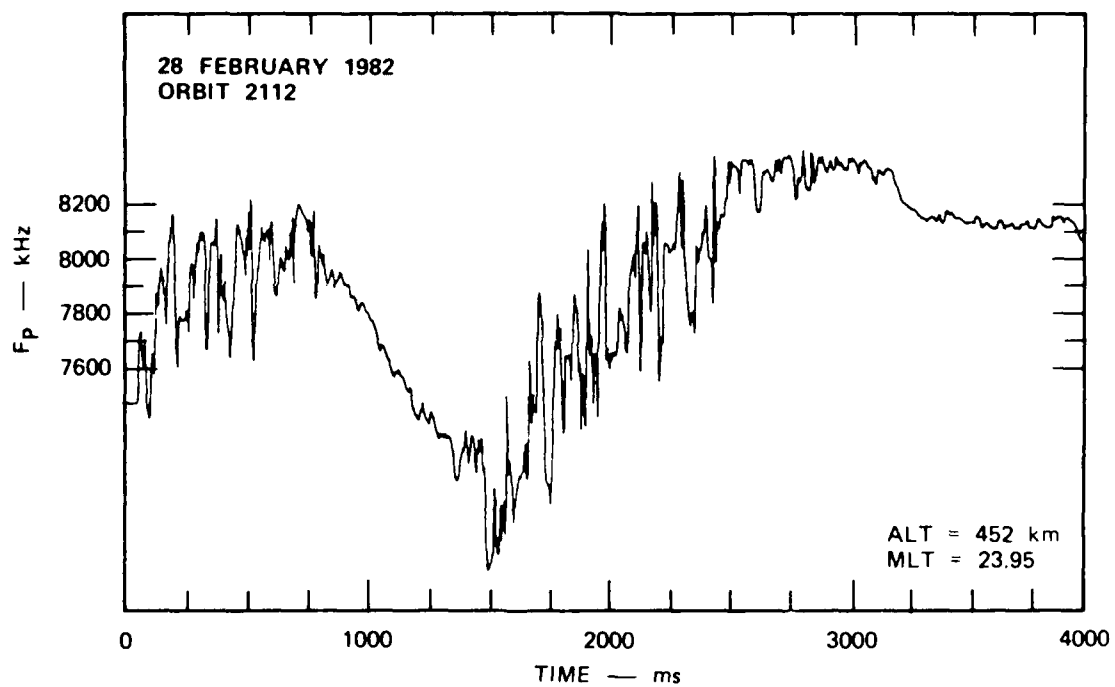


Figure 28. Enlarged illustration of asymmetric irregularity distribution.

a two-component spectrum [182, 183, 186]. Because the growth rate increases with k for small k [see Eqs. (3) or (12)] and decreases rapidly at large k values [see Eq. (15)], a maximum in growth rate occurs at some finite k value [182, 183]; that maximum may be related to the freezing scale seen in barium ion clouds (and presumably, F-region blobs).

Zalesak et al. [186] have argued that the M dependence in Eq. (15) indicates that diffusion is more rapid in outer (less dense) portions of the ion cloud than in the central (more dense) portions of the ion cloud. They, then, postulated that if structuring (bifurcation) always starts at the outer edges of blobs and works its way inward, rapid diffusion (small M) will stop bifurcation before it starts. On this basis, striations of a few hundred meters might be long lived, while striations with smaller scales dissipate rapidly. The effectiveness of this mechanism remains to be evaluated, particularly in the high-latitude F region. It seems likely to be most effective under conditions when M is large and not when M is close to unity. (We have shown in the previous section that the M value associated with F-region blobs is near unity.) A perhaps more promising mechanism that might account for the existence of a freezing scale is the magnetic viscosity effects [223], a process that seems to allow both sharp plasma density gradients and long irregularity lifetimes (L. Wittwer, personal communication).

Finally, we find that spectral results from HF backscatter radars also appear to support the role of interchange instabilities. Doppler spectra associated with meter-scale irregularities indicate that they are part of a low-frequency process, such as the $\underline{E} \times \underline{B}$ instability. That is, the phase velocity has been found to be small compared to convection velocities [74, 76, 77, 224-226], with the small-scale irregularities drifting virtually with bulk plasma motion. The narrow spectral widths also indicate that the phase velocities associated with small-scale irregularities are small.

4.5 ROLE OF NEUTRAL DYNAMICS.

The irregularity growth rate of the $\underline{E} \times \underline{B}$ instability is directly proportional to the slip velocity. Although acceleration of the neutral gas by large electric fields is expected through ion drag [227], neutral gas dynamics has been virtually ignored in the interpretation of observations in terms of the $\underline{E} \times \underline{B}$ instability. It is important to realize that regions of large slip velocity are not necessarily the same as those for large electric fields. If convection is spatially uniform or stationary with time, the slip velocity can be very small or even zero. On the other hand, the slip velocity will be large in regions in which convection is nonuniform, i.e., spatially varying in either magnitude or direction; or where convection is nonstationary, e.g., during substorm activity or pulsation events. Variations in the neutral wind (e.g., produced by atmospheric gravity waves) about their mean velocity also must be considered because they could represent a source of electric-field perturbations through dynamo action. These perturbations (in the E or F regions) are, in fact, likely as sources of seed perturbations that ultimately contribute to the observed k spectrum of irregularities.

Wickwar et al. [228] computed the mean meridional neutral wind (U_N) measured over Chatanika, Alaska over a 7-year period (1972 to 1978) by incoherent-scatter radar. Their results presented in Figure 29 (circles connected by line segments) reveal a small poleward wind (< 100 m/s) from 1000 to 1800 AST (Alaskan Standard time) and a larger equatorward wind (> 200 m/s) from 2000 to 0800 AST. The presence of a meridional neutral wind of significant magnitude in the midnight sector suggests that the north-south component of the slip velocity may differ from the bulk plasma drift. To estimate the slip velocity, we have included the mean plasma-drift velocity deduced from another data set, also obtained over Chatanika [V. B. Wickwar, unpublished results]. We see that the meridional component of plasma drift (V_N) tracks the neutral wind component very closely throughout the premidnight hours. This near coincidence

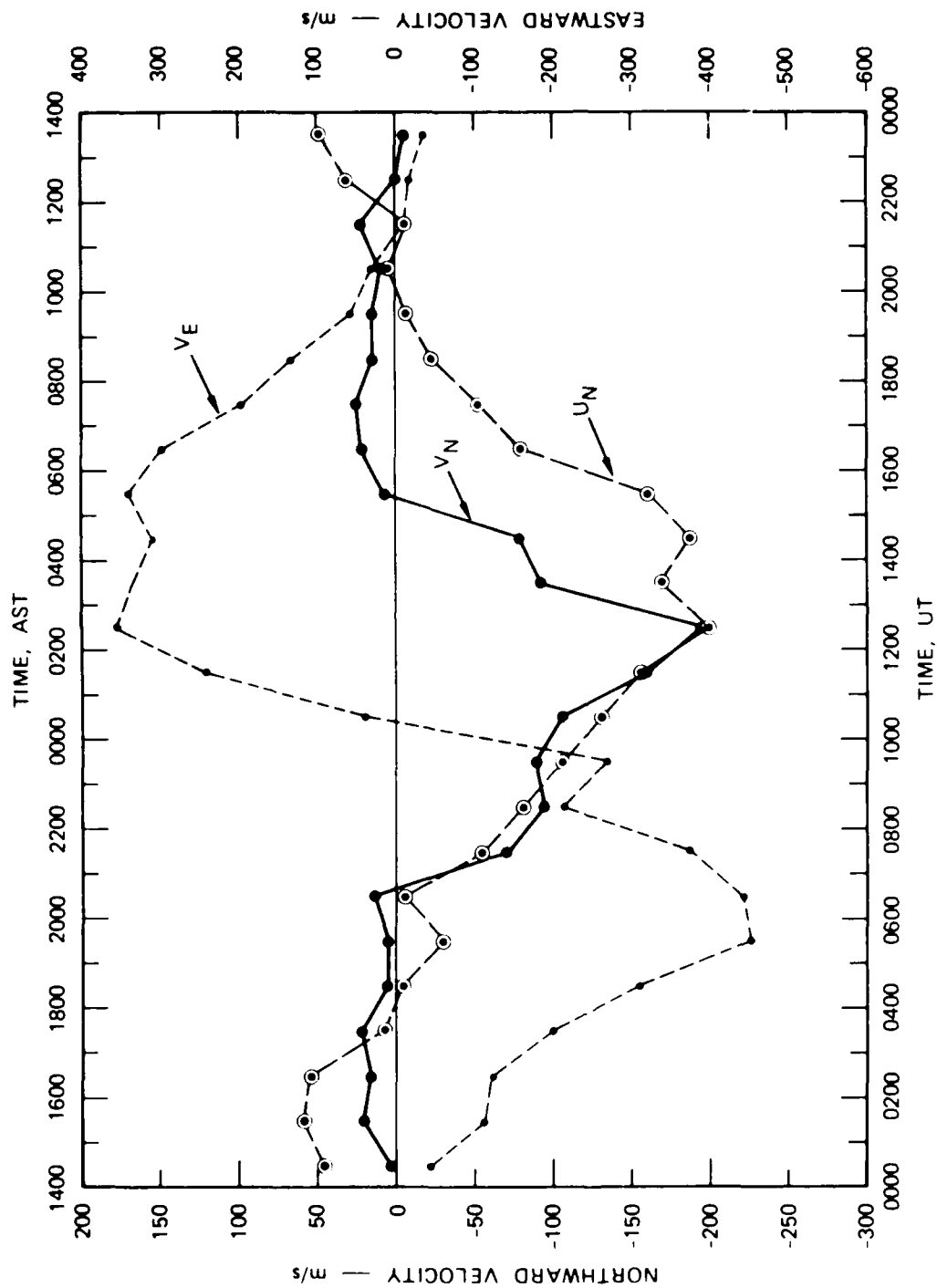


Figure 29. Diurnal variation in the meridional neutral wind determined from Chatanika incoherent-scatter measurements and associated convection velocity components.

suggests that the meridional component of the average slip velocity is very small during this period. On the other hand, the meridional component of the average slip velocity reaches a maximum value of 170 m/s in the postmidnight sector. The asymmetry is apparently produced by the presence of drivers of the meridional neutral wind other than ion drag [229].

The zonal component of the average slip velocity can be estimated by comparing the average neutral-wind vector derived from 630.0-nm Fabry-Perot interferometer measurements by Sica et al. [230] to the zonal plasma drift curve in Figure 29. The components of the average neutral wind, computed from 44 nights of data (1981 to 1983), are presented in Figure 30 [230]. If we assume that magnetic midnight is around 0130 UT, we can compare the meridional components of the neutral wind in Figures 29 and 30. We see that both have very similar curves, giving us some confidence in comparing the zonal components. We see that the two curves are similar in shape but differ in amplitude. The maximum zonal plasma drift in the premidnight sector is about 450 m/s while the corresponding zonal neutral wind is no more than 350 m/s. In the postmidnight sector, the maximum zonal plasma drift is about 350 m/s while that for the neutral wind is no more than 150 m/s. With these numbers, the magnitudes of the average slip velocity are 100 m/s and 200 m/s in the pre- and post-midnight sectors, respectively. The directions of the average slip velocity is strictly zonal (westward) in the premidnight sector and northeastward in the postmidnight sector.

Although the average slip velocity is moderate in magnitude, we find that the slip velocity can vary substantially on any given night, particularly during periods of high geomagnetic activity. Nagy et al. [229] presented measurements of the slip velocity during a night when the Kp index remained above 4+ throughout the period of observations. The plasma drift exceeded 1 km/s on occasions while the neutral wind remained less than 200 m/s. On this basis, we conclude that slip velocity appears significant but small on the average, at least in the auroral zone, but

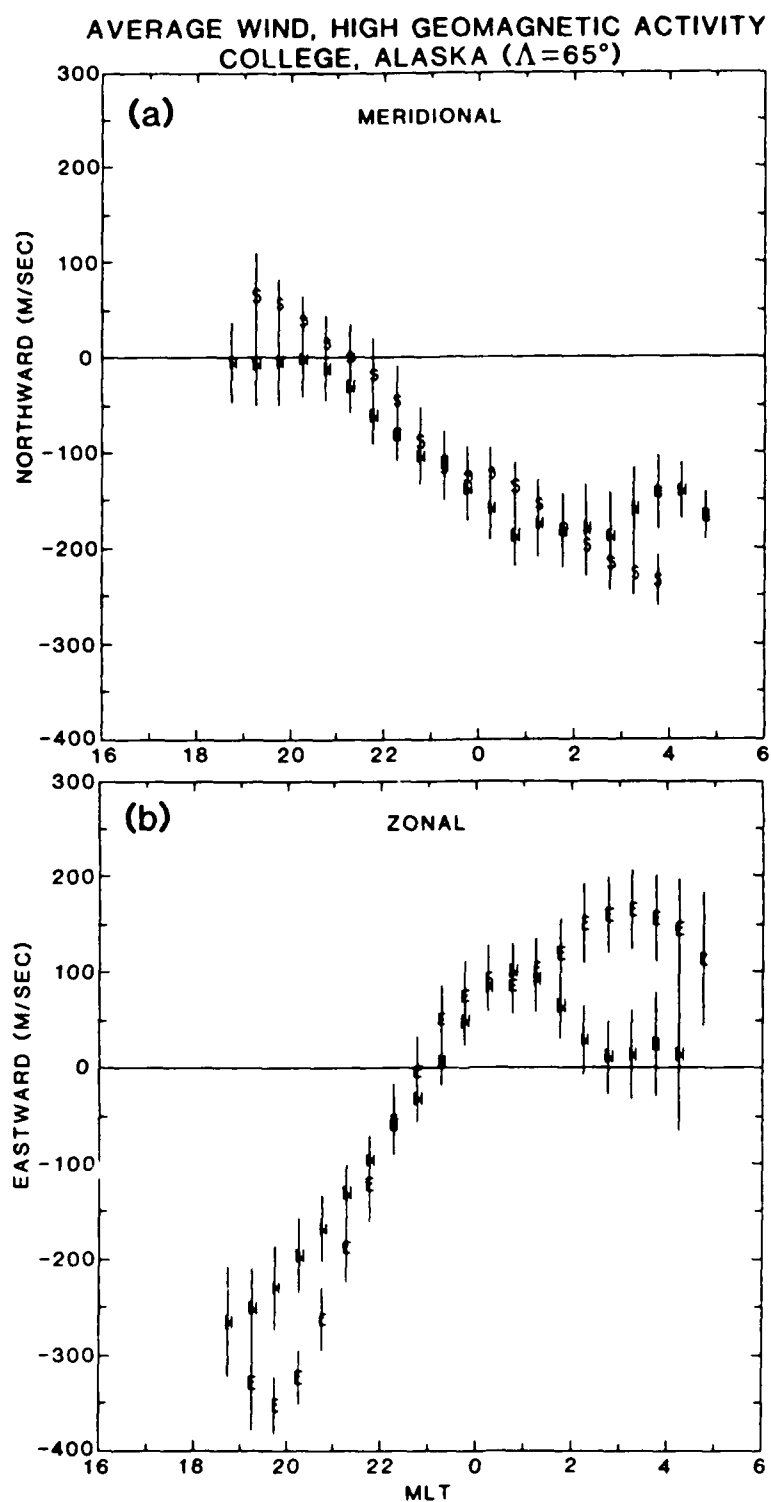


Figure 30. Average neutral-wind components (in geomagnetic coordinates) for high geomagnetic activity [229].

can become very large during periods of strong geomagnetic activity. Because slip velocities depend on the slow response of the neutral gas to sudden changes in plasma drift, we also expect large slip velocities in regions where the convective plasma flow is not uniform, e.g., along the poleward auroral boundary. Enhanced ion temperatures, evidence of correspondingly-large slip velocities, have been reported to occur along this boundary [59, 153].

The asymmetry in slip velocity about the midnight sector was also reported by Baron and Wand [231] who found that ion-temperature enhancements are larger and longer lasting in the postmidnight sector relative to the premidnight sector, for a given electric field enhancement. Because ion temperature is directly proportional to the square of the slip velocity, these results indicate that larger slip velocities are indeed found in the morning sector rather than the evening sector. A scatter plot showing this effect is presented in Figure 31, where we have combined two data sets reported by Baron and Wand [231]. Note that ion temperature is plotted versus V_E . Referring back to Figure 29, we see that V_N is half as large as V_E in the midnight sector. The error introduced by neglecting the V_N , therefore, is 56 percent. The sense of this error is to reduce the slopes of the lines in Figure 31. But, because the slopes of the lines in the morning sector are about three times steeper than those in the evening sector, the qualitative behavior displayed in Figure 31 is probably correct. Baron and Wand [231] proposed that the asymmetry in frictional heating may be produced by higher F-region plasma densities in the evening sector which would result in closer coupling between plasma and neutral gas. If this interpretation is correct, larger slip velocities in the morning sector will increase the growth rate of the $\underline{E} \times \underline{B}$ instability, assuming no changes in the gradient scale length.

The discovery of larger slip velocities in the morning sector compared to the evening sector, when combined with the morphological results reported by Clark and Raitt [105] (Figure 6), seem to contradict predictions of the $\underline{E} \times \underline{B}$ instability. Clark and Raitt [105] reported enhanced

irregularity strengths in the evening sector, whereas the $\underline{E} \times \underline{B}$ instability predicts larger growth rates in the morning sector because of larger slip velocities.

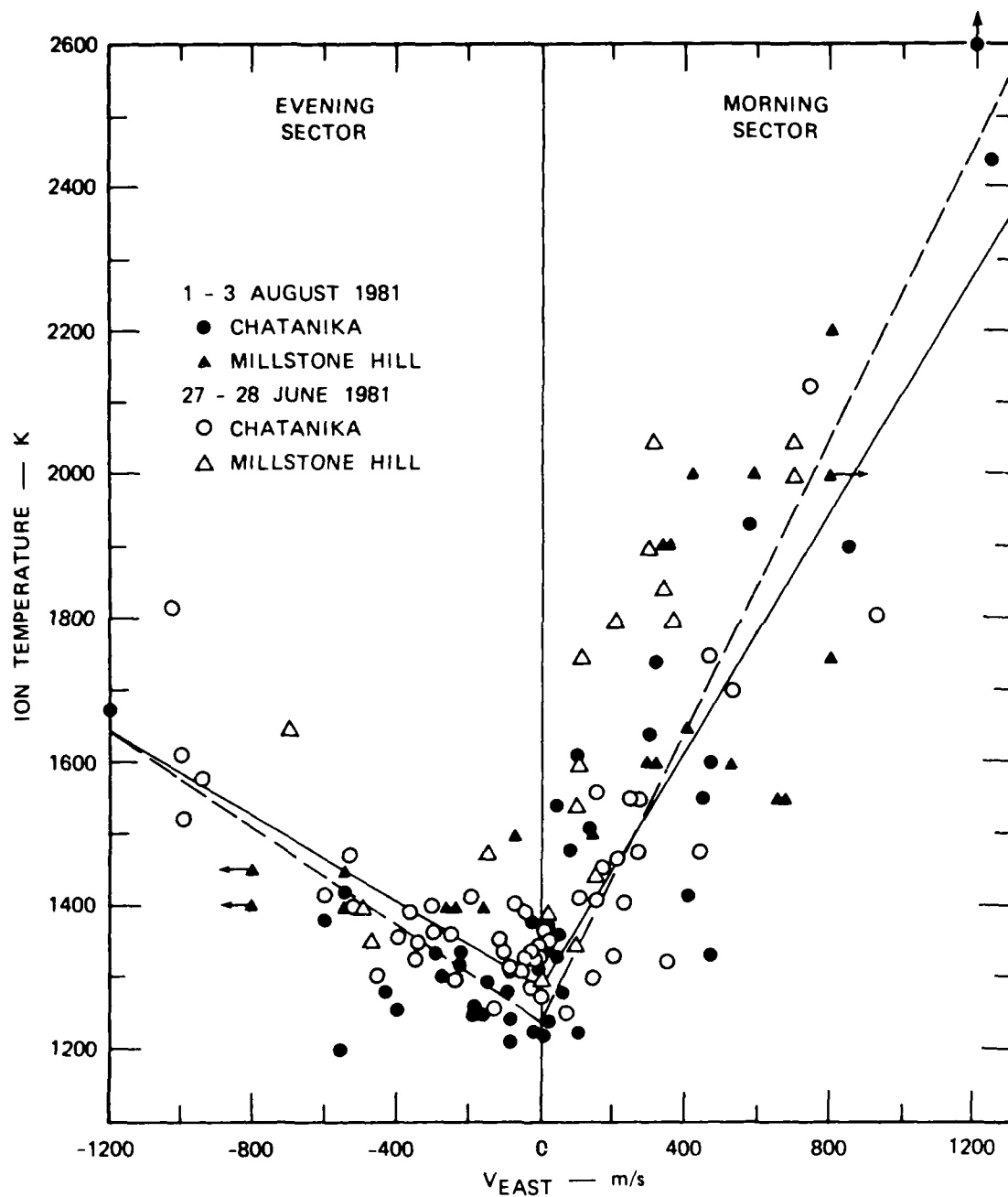


Figure 31. Asymmetry in ion temperatures in the evening and morning sectors as a function of zonal convection velocity [230].

SECTION 5

DESCRIPTIVE WORKING MODEL

We have found that most of the prominent plasma structure in the polar ionosphere can be accounted for by MFTI processes acting on plasma produced by solar radiation and particle precipitation. At the largest scales, structure in solar-produced plasma (patches, boundary and sub-auroral blobs) is produced by MFTI driven by magnetospheric convection. Particle precipitation and some kind of wave activity contribute additional plasma structure at scales down to 10 km. Strong irregularities at $\lambda < 10$ km (but greater than the ion gyroradius) appear to be controlled by the $\underline{E} \times \underline{B}$ instability. This control is evident when observations are properly interpreted; i.e., when neutral gas dynamics and background plasma effects are included in assessing the effectiveness of the $\underline{E} \times \underline{B}$ instability. When this is done, we find that observations are consistent with an irregularity model in which (1) irregularities are produced primarily within patches and sun-aligned arcs that are situated in the dark polar cap, and (2) auroral irregularities are produced near auroral boundaries where spatially varying convection allows significant slip velocities to develop and where the E-region Pedersen conductance is low. Irregularities also may be generated under conditions when the electric field is time-varying with periods less than an hour (e.g., substorms and pulsation events), provided that the underlying E layer is not highly conducting. The salient features of this unified model and underlying processes are discussed in more detail in the following subsections.

5.1 PHENOMENOLOGY.

5.1.1 Large-Scale Plasma Structure ($\lambda > 10$ km).

The largest-scale plasma structures that participate in the phenomenology of high-latitude, F-region irregularities are polar-cap patches that are observed primarily under southward B_z conditions. Patches are large parcels (1000 km in diameter) of solar-produced plasma that have become detached from the dayside subauroral ionosphere. Although details are not known, patches presumably form during variations in the B_z (and possibly B_y) component of the IMF. The most likely scenario is a southward turning of B_z , which leads to application of a large eastward electric field at lower latitudes and rapid poleward movement of subauroral plasma. Another change, such as a northward turning of B_z , then retracts the eastward electric field that had been applied at lower latitudes and thus prevents transport of any more subauroral plasma into the polar cap. A patch is thereby formed by shutting off the flow of subauroral plasma to the polar cap. Once formed, patches convect antisunward over the polar cap and into the midnight auroral zone. There patches enter sunward convective flow and are thought to be reconfigured into boundary and subauroral blobs as they flow toward (and along) the equatorward auroral boundary. Reconfiguration leaves blobs highly elongated in longitude (extending as much as 12 hours in local time) and as narrow as 100 km in latitudinal width.

Because solar radiation is a well-behaved ionization source, it seems that the characteristics of patches and boundary (subauroral) blobs could be made more predictable. For example, Baron et al. [232] analyzed 11 years of Chatanika incoherent-scatter data and found that the solar-produced F layer can be reliably estimated from 10.7-cm solar flux (S_a). They found that the peak plasma density in the dayside winter F-layer can be estimated from the following formula,

$$n_m^F = \left(\frac{S_a}{100}\right) \left(2.5 + \frac{(S_a - 60)}{20}\right) \times 10^5 \text{ el/cm}^3$$

We note that dayside measurements made at Chatanika are those for the subauroral ionosphere, as already shown in Figure 9. Using the above formula to determine the initial, peak plasma density in patches, modeling studies similar to that conducted by Robinson et al. [4] could be pursued to determine the decay in plasma density as a patch convected over the polar cap and evolved into a boundary (or subauroral) blob.

Besides solar-produced plasma, localized soft-particle precipitation also contributes to F-region plasma densities along the equatorward auroral boundary. The present impression is that electron precipitation there is time varying, being most intense under substorm conditions. When the flux is intense enough, the peak plasma density could reach a few times 10^5 el/cm³. When it is not, plasma-density buildup along the auroral boundary is possible through spatial resonance; i.e., boundary blobs might remain under the ionization source long enough to accumulate significant ionization.

Under northward B_z conditions, the polar cap is populated by sun-aligned arcs that appear to drift slowly in dawn-dusk directions. The peak plasma density within these F-region arcs can be as high as 2×10^5 el/cm³, and are produced by "polar shower" precipitation in the central polar cap. It seems that the F-region plasma arcs that form remain in the polar cap during northward B_z conditions (because of weak antisunward convection) may actually enter the nightside auroral region when B_z turns southward. Appearance of plasma arcs (produced by precipitation along sun-aligned arcs) in the auroral zone has not been confirmed; it is possible that they cannot be differentiated from auroral blobs. (Patches are also occasionally observed in the polar cap together with sun-aligned arcs, under northward B_z conditions.)

Another important category of large-scale plasma structures includes auroral blobs and localized depletions along the poleward boundary of the auroral oval. Although little is yet known about these structures, they appear to be produced either by intense soft-particle precipitation or by enhanced plasma loss rates associated with large electric fields. (Auroral blobs have been observed intermittently throughout

the auroral zone. Their intermittent nature might be suggesting a relationship to substorms; the existence of such a relationship has not yet been explored.) Because velocity shears appear to be relatively persistent along the poleward auroral boundary, it is possible that localized depletions and plasma-density enhancements characterize that boundary.

Finally, there exists in the auroral zone, quasi-periodic plasma-density variations with a wavelength close to 10 km. The plasma-density fluctuations associated with the wavelike structures are much larger than expected from simple power-law extrapolation of those associated with smaller-scale irregularities. On this basis, we conclude that the wavelike structures are not produced by the same processes responsible for smaller-scale irregularities. The source of these quasi-periodic structures are not yet known but it is tempting to attribute them to some kind of wave activity.

5.1.2 Smaller-Scale Irregularities ($\lambda < 10$ km).

The phenomenology of smaller-scale irregularities resembles that for large-scale plasma structure. During solar maximum conditions, the polar cap is the most disturbed region in the polar ionosphere (more so than the auroral ionosphere). Scintillations (e.g., at 250 MHz) are observed continuously, with considerable modulation in scintillation intensity. On the average, irregularity intensity is strongest in the nightside, winter polar cap. Enhanced scintillations are correlated with patches during southward B_z conditions and sun-aligned arcs during northward B_z conditions. Irregularities are distributed throughout the patches with maximum intensity along their trailing edges. During solar minimum conditions, irregularity intensity in the polar cap decreases dramatically, becoming virtually nonexistent except within patches (again, with some preference for trailing edges); none appear to be associated with sun-aligned arcs.

Unlike kilometer-scale irregularities in the polar cap, auroral irregularities appear relatively independent of solar activity

(although some variation is seen). There is, however, a seasonal dependence that appears to be a function of longitude. Auroral irregularities are most intense and believed to be generated in two spatially deterministic source regions: (1) along the poleward auroral boundary, and (2) near the equatorward, diffuse auroral boundary. Irregularities are found along the poleward boundary at all times, while those near the equatorward auroral boundary favor the night sector. As in the polar cap the auroral irregularity-source regions appear to be spatially collocated with large-scale plasma structure. Auroral blobs and localized depletions are thought to occur along the poleward auroral boundary, while boundary and subauroral blobs are known to occur along the equatorward boundary. Weaker irregularities are often observed between these boundaries. Enhancements, at least at kilometer scales, also appear to occur in the Harang discontinuity region, near sunset, and in the postnoon sector.

5.2 IRREGULARITY GENERATION AND DECAY.

5.2.1 MFTI Processes.

Interchange processes appear to play a major role in irregularity production, but different drivers act at different scale sizes. At scales greater than 10 km, MFTI seems to be produced by irregular electric fields mapped to the F layer from other regions. At the largest scales, patches are reconfigured into boundary and subauroral blobs by the magnetospheric convection pattern. Boundary (and subauroral) blobs also appear subject to structuring by MFTI produced by smaller-scale, irregular electric fields. Sources of irregular electric fields include magnetospheric turbulence, and E-region polarization and dynamo effects. At smaller scale sizes (say less than a kilometer), electric fields do not map as readily as at larger scale sizes, and therefore those generated in regions other than the F layer become less of a factor.

5.2.2 Interchange Instabilities.

The $\underline{E} \times \underline{B}$ instability is clearly operating at $\lambda < 10$ km (but greater than the ion gyroradius), and in fact, appears to control irregularity characteristics at those scale sizes. (The current-convective instability is not nearly as effective as the $\underline{E} \times \underline{B}$ instability in the polar ionosphere, at least not in a large-scale sense.) Most observations of strong irregularity characteristics appear to be consistent with interpretation in terms of the $\underline{E} \times \underline{B}$ instability if we account for neutral gas dynamics and background plasma effects.

The average slip velocity in the auroral oval is nearly zero in the evening sector, and small ($V_o < 150$ m/s) in the midnight and morning sectors. Small ambient slip velocities in spite of the presence of large electric fields are expected in the evening and morning sectors because those sectors are characterized by near-uniform zonal flows where the neutral gas has time to accelerate to ion speeds. Large slip velocities are most likely to occur along the poleward boundary of the auroral oval where sharp reversals (both rotational and shear) in plasma drift are almost always present. Similar conditions, however, do not exist along the equatorward irregularity-source region. There the electric field (under ambient conditions) is more or less uniform with latitude. But because of large differences in plasma density between the boundary blob and the trough, we expect differential ion drag to produce a neutral-wind shear in the vicinity of the boundary blob. A shear in neutral wind is, therefore, produced with a corresponding variation in slip velocity. Finally, large slip velocities might be expected in the Harang discontinuity region in which convective flow reverses from westward to eastward. Basu et al. [82], for example, found in a case study that the observed patch of scintillations occurred in a region of large velocity structure. Although they proposed a different mechanism, those observations are consistent with the $\underline{E} \times \underline{B}$ instability, at least in terms of having a large slip velocity.

The slip velocity in the polar cap is expected to depend strongly on the existing convection pattern. In the case of a simple

two-cell convection pattern (that might exist under $B_z < 0$ conditions), the slip velocity is likely to be largest near auroral boundaries where the convection pattern is spatially nonuniform, and smallest in the central polar cap where the flow is purely antisunward. Variations in B_y are expected to alter the symmetry in slip velocity about the noon-midnight meridian. Under $B_z > 0$ conditions, the convection pattern is likely to be more complicated with a correspondingly complicated slip velocity distribution. Slip velocities are expected to be large in the vicinity of velocity shear regions, such as found near sun-aligned arcs.

We note that virtually all slip velocities of any significance are directed orthogonally to the plasma-density gradient associated with the large-scale plasma structure. This is certainly true for boundary and subauroral blobs and sun-aligned arcs. The plasma features along the poleward auroral boundary also seem to fall into this category. The only large-scale plasma structures with expected east-west gradients are those produced by particle precipitation. Further information, therefore, is needed regarding existing east-west gradients in large-scale plasma structure.

Large slip velocities also are likely under time-varying conditions (with periods less than an hour), such as during auroral substorms and geomagnetic pulsation events. For example, Aarons [233] reported rapid scintillation onset following magnetic storm sudden commencement. One interpretation is the development of a large slip velocity. Tsunoda et al. [234] found that large, oscillating electric fields with a period of minutes (or longer) can occur even under extremely quiet geomagnetic conditions. Corresponding variations in the slip velocity would be produced because of the slow response of the neutral gas.

Background plasma effects, evaluated in terms of parameters M and C_r , have also been found to strongly affect irregularity growth rate. During solar minimum conditions, F-region blobs found in the central auroral zone are usually associated with M values very close to unity. Under these conditions, the $\underline{E} \times \underline{B}$ growth rate is nearly zero. During

solar maximum conditions, the blob Pedersen conductance increases tenfold over that found during solar minimum conditions. But because the auroral E layer remains highly conducting (regardless of solar activity), the M value is still no more than about 1.2. On this basis, irregularity growth is strongly suppressed (through polarization shorting and enhanced cross-field diffusion) by the presence of an auroral E layer. The two irregularity-source regions found along the auroral boundaries again seem consistent with M variations in latitude. The energy of precipitating particles softens near the poleward auroral boundary, presumably resulting in lower E-region Pedersen conductances, and hence, larger M values. Near the equatorward auroral boundary, subauroral blobs (by definition) are found equatorward of the auroral E layer, and therefore, have large M values. Boundary blobs probably have varying M values depending on their exact location relative to the auroral E layer. Similar tendencies are found in the polar cap where irregularities favor the nightside, winter ionosphere under solar maximum conditions.

One way of developing strong $\underline{E} \times \underline{B}$ growth rates in the presence of a highly-conducting E layer is through image formation allowed by background plasma compressibility ($C_r > 1$). Despite high compressibility, significant images do not appear to form at kilometer scales in the auroral E layer because of rapid recombination chemistry and high plasma densities. The findings, therefore, suggest that the effects of images cannot offset the polarization shorting effects of a highly-conducting E layer. The conclusion is that $\underline{E} \times \underline{B}$ growth rates are controlled primarily by the slip velocity and the Pedersen conductance of the auroral E layer.

It is important to point out that the discussion in the above two paragraphs assumed perfect electrical coupling between the E and F layers. As mentioned at the beginning of this section, this assumption appears to break down at scale sizes less than a kilometer when considering the E and F layers. Coupling effects therefore affect irregularity growth rates by making M wave number dependent. The wave number dependence appears through reduction in both end-shortening effects and in the formation of images.

5.3 SPECTRAL CHARACTERISTICS.

The spectral characteristics appear to reflect different contributions as a function of spatial wavelength. At patch-size scales, irregularity amplitudes are controlled by global electrodynamics and aeronomic processes. Irregularity strengths at blob-size scales (~ 100 km) are likely to be determined by the number flux of soft electrons and the time a magnetic flux tube spends under the particle-source region. A third contributor appears to be some kind of wave source operating around 10-km scale size. The spectral range associated with scale sizes less than 10 km appears to be controlled by interchange instability processes. The irregularity strengths associated with interchange processes appear significantly weaker than those contributed at the larger scale sizes. At the very shortest scales (not considered in this review), we expect finite ion gyroradius effects and contributions from kinetic instabilities.

If a power-law form is used to fit spectral characteristics at $\lambda < 10$ km, it seems that a segmented fit using three different spectral indices is needed. The spectral index for irregularities $10 \text{ km} > \lambda > 300 \text{ m}$ appear to be durable with a value ≤ 2 . (A more accurate estimate of the spectral slope can be obtained by careful partitioning of wavelength regimes before performing power-law fits.) This index is consistent with spectral indices estimated from nonlinear simulations of interchange instabilities. The spectral slope is expected to be steeper at wavelengths greater than a few kilometers because of the presence of significantly larger amplitudes at wavelengths around 10 km and beyond. The spectral slope associated with these large wavelengths is perhaps not as important as the recognition that a spectral discontinuity is introduced by large-amplitude quasi-periodic structure around 10 km. The spectral form for $\lambda > 10$ km depends on processes associated with patches, blobs, and depletions. At wavelengths less than 300 m, the spectral index is found in 25 percent of the cases to increase to a value around 3.

There currently exists two interpretations for the spectral break found around 300 m. One is that it is produced by a wavelength dependence in $\underline{E} \times \underline{B}$ growth rate associated with background plasma effects. The

growth rate increases linearly with k at long wavelengths and decreases more rapidly with k at short wavelengths, thus producing a preferred wavelength for maximum growth rate. It is tempting to consider the spectral break as an intrinsic characteristic of the convective interchange instability because the knee also has appeared in irregularity spectra associated with equatorial spread F and barium ion clouds (see Section 4.4.3). In both cases, the irregularities are thought to be produced by the same instability with different drivers. The other interpretation is that the knee in the spectrum represents the stirring wavelength found in two-dimensional plasma turbulence. The limited occurrence (≤ 25 percent of time) of two-component spectra is puzzling because that feature should be present most of the time according to both interpretations. It is conceivable that the two-component spectrum is actually more common but is perhaps masked by other effects such as spectral contributions from steep gradients associated with larger-scale plasma structure (L. Wittwer, personal communication).

5.4 OTHER PROCESSES.

Although this review has focused only on MFTI processes as a means of irregularity generation, we must keep in mind that other promising source mechanisms have been proposed. Even if most of the irregularity characteristics can be interpreted in terms of interchange instabilities, it is important to determine whether those characteristics are also predicted by other competing mechanisms, and which ones dominate or contribute under given geophysical conditions. For example, Das and Das [235] and Lee [236] proposed a thermal instability in which the ohmic dissipation of the Pedersen current in the electron gas leads to the production of plasma-density irregularities. Irregularities are presumably produced within a few minutes by electric fields greater than 25 mV/m. From our review, we have not found clear-cut relationship between irregularities and large electric fields. A more careful evaluation, however, is necessary. Another topic that has received considerable

attention is the dissipation of irregularities through enhanced cross-field diffusion produced by drift-wave instabilities [237-244]. These effects must be considered if we are to determine the nature of the spectral break that occurs around 300 m.

5.5 OUTSTANDING QUESTIONS.

In the formulation of the descriptive working model, we have raised several important issues.

- (1) What is the mechanics of patch formation? Do changes in the IMF control it? Demonstrating patch formation by appropriate computer models is desirable.
- (2) What is the nature of large-scale plasma structure along the poleward boundary of the auroral oval? Does particle precipitation produce blobs? What is the role of suprathermal electron bursts in auroral-blob formation, if any? Do localized depletions provide a significant source of plasma-density gradients? Is there sufficient softening in particle energy along the polar-cap boundary to produce a measurable decrease in Pedersen conductance?
- (3) What mechanism produces distributed irregularities within polar cap patches? Is the plasma density distribution in patches smooth (as expected from solar illumination) or granular? What is the source of granularity? Does soft-particle precipitation in the cusp region or by some sort of wave activity produce the granularity?
- (4) What is the morphology of the slip velocity? Does it maximize in the vicinity of the irregularity-source regions?
- (5) Do E-region images significantly alter production and decay rates of F-region irregularities?
- (6) What are the underlying physical processes that control the development of two-component spectra (i.e., spectral break at

300 m)? Why is the spectral break seen less than 25 percent of the time? How variable is the wavelength associated with the spectral break?

- (7) Do E-region polarization and dynamo effects contribute to the generation of irregular electric fields and MFTI effects in the F region?

SECTION 6

LIST OF REFERENCES

- Aarons, J., J. Geophys. Res., 78, 7441 (1973).
- Aarons, J., J. Geophys. Res., 81, 661 (1976).
- Aarons, J., and R. S. Allen, J. Geophys. Res., 76, 170 (1971).
- Aarons, J., E. MacKenzie, and K. Bhavnani, Radio Sci., 15, 115 (1980).
- Aarons, J., J. P. Mullen, and S. Basu, J. Geophys. Res., 68, 3159 (1963).
- Aarons, J., H. M. Silverman, and B. A. Ramsey, Ann. Geophys., 22, 349
(1966).
- Aarons, J., J. P. Mullen, and H. E. Whitney, J. Geophys. Res., 74, 884
(1969).
- Aarons, J., J. P. Mullen, H. E. Whitney, A. L. Johnson, and E. J. Weber,
Geophys. Res. Lett., 8, 277 (1981).
- Anderson, D. N., and M. Mendillo, Geophys. Res. Lett., 10, 541 (1983).
- Baker, K. B., R. A. Greenwald, and R. T. Tsunoda, Geophys. Res. Lett., 10,
904 (1983).
- Baker, K. B., R. A. Greenwald, A. D. M. Walker, P. F. Bythrow,
L. J. Zanetti, T. A. Potemra, D. A. Hardy, F. J. Rich, and C. L. Rino,
J. Geophys. Res., 91, 3130 (1986).

- Balsley, B. B., G. Haerendel, and R. A. Greenwald, J. Geophys. Res., 77, 5625 (1972).
- Banks, P. M., C. L. Rino, and V. B. Wickwar, J. Geophys. Res., 79, 187 (1974a).
- Banks, P. M., C. R. Chappell, and A. F. Nagy, J. Geophys. Res., 79, 1459 (1974b).
- Baron, M. J., and R. H. Wand, J. Geophys. Res., 88, 4114 (1983).
- Baron, M. J., C. J. Heinselman, and J. Petriceks, Radio Sci., 18, 895 (1983).
- Basu, S., J. Geophys. Res., 83, 182 (1978).
- Basu, S., and J. Aarons, Radio Sci., 15, 59 (1980).
- Basu, S., R. L. Vesprini, and J. Aarons, Radio Sci., 9, 355 (1974).
- Basu, S., E. MacKenzie, S. Basu, H. C. Carlson, D. Hardy, F. J. Rich, and R. C. Livingston, Radio Sci., 18, 1151 (1983).
- Basu, S., S. Basu, E. MacKenzie, W. R. Coley, W. B. Hanson, and C. S. Lin, J. Geophys. Res., 89, 5554 (1984).
- Basu, S., S. Basu, E. MacKenzie, and H. E. Whitney, Radio Sci., 20, 347 (1985).
- Basu, S., S. Basu, C. Senior, D. Weimer, E. Nielsen, E., and P. F. Fougere, Geophys. Res. Lett., 13, 101 (1986).
- Bates, H. F., J. Geophys. Res., 65, 1993 (1960).
- Bates, H. F., J. Atmos. Terr. Phys., 28, 903 (1966).
- Bates, H. F., S.-I. Akasofu, D. S. Kimball, and J. C. Hodges, J. Geophys. Res., 78, 3857 (1973a).

- Bates, H. F., A. E. Belon, and R. D. Hunsucker, J. Geophys. Res., 78, 648 (1973b).
- Beghin, C., J. F. Karczewski, B. Poirier, R. Debie, and N. Massewitch, Ann. Geophys., 38, 615 (1982).
- Bernhardt, P. A., M. B. Pongratz, S. P. Gary, and M. F. Thomsen, J. Geophys. Res., 87, 2356 (1982).
- Bernhardt, P. A., M. F. Thomsen, and S. P. Gary, J. Geophys. Res., 88, 938 (1983).
- Bhattacharyya, A., and G. S. Lakhina, Planet. Space Sci., 30, 581 (1982).
- Bourdillon, A., M. Nicollet, and J. Parent, Geophys. Res. Lett., 9, 696 (1982).
- Buchau, J., B. W. Reinisch, E. J. Weber, and J. G. Moore, Radio Sci., 18, 995 (1983).
- Buchau, J., E. J. Weber, D. N. Anderson, H. C. Carlson, Jr., J. G. Moore, B. W. Reinisch, and R. C. Livingston, Radio Sci., 20, 325 (1985).
- Burch, J. L., W. Lennartsson, W. B. Hanson, R. A. Heelis, J. H. Hoffman, and R. A. Hoffman, J. Geophys. Res., 81, 3886 (1976).
- Burke, W. J., M. S. Gussenhoven, M. C. Kelley, D. A. Hardy, and F. J. Rich, J. Geophys. Res., 87, 2431 (1982).
- Burke, W. J., M. Silevitch, and D. A. Hardy, J. Geophys. Res., 88, 3127 (1983).
- Bythrow, P. F., T. A. Potemra, W. B. Hanson, L. J. Zanetti, C.-I. Meng, R. E. Huffman, F. J. Rich, and D. A. Hardy, J. Geophys. Res., 89, 9114 (1984).

- Cahill, L. J., Jr., R. L. Arnoldy, and W. W. L. Taylor, J. Geophys. Res., 85, 3407 (1980).
- Candidi, M., H. W. Kroehl, and C.-I. Meng, Planet. Space Sci., 31, 489 (1983).
- Carlson, H. C., Jr., V. B. Wickwar, E. J. Weber, J. Buchau, J. G. Moore, and W. Whiting, Geophys. Res. Lett., 11, 895 (1984).
- Cauffman, D. P., and D. A. Gurnett, Space Sci. Rev., 13, 369 (1972).
- Cerisier, J. C., J. J. Berthelier, and C. Beghin, Radio Sci., 20, 755 (1985).
- Chaturvedi, P. K., and S. L. Ossakow, Geophys. Res. Lett., 6, 957 (1979).
- Chaturvedi, P. K., and S. L. Ossakow, J. Geophys. Res., 86, 4811 (1981).
- Chaturvedi, P. K., and S. L. Ossakow, J. Geophys. Res., 88, 4119 (1983).
- Clark, D. H., and W. J. Raitt, Planet. Space Sci., 23, 1643 (1975).
- Clark, D. H., and W. J. Raitt, Planet. Space Sci., 24, 873 (1976).
- Cronyn, W. M., Astrophys. J., 161, 755 (1970).
- Das, U. N., and A. C. Das, Planet. Space Sci., 31, 311 (1983).
- Davis, T. N., G. J. Romick, E. M. Wescott, R. A. Jeffries, D. Kerr, and H. M. Peek, Planet. Space Sci., 22, 67 (1974).
- de la Beaujardiere, O., and R. A. Heelis, J. Geophys. Res., 89, 1627 (1984).
- de la Beaujardiere, O., V. B. Wickwar, G. Caudal, J. M. Holt, J. D. Craven, L. A. Frank, L. H. Brace, D. S. Evans, J. D. Winningham, and R. A. Heelis, J. Geophys. Res., 90, 4319 (1985).
- de la Beaujardiere, O., V. B. Wickwar, and J. H. King, Proc. AGU Chapman Conf. Solar Wind-Magnetosphere Coupling, 1986.

- Doles, J. H., III, N. J. Zabusky, and F. W. Perkins, J. Geophys. Res., 81, 5987 (1976).
- Drake, J. F., J. D. Huba, and S. T. Zalesak, J. Geophys. Res., 90, 5227 (1985).
- Dyson, P. L., J. Geophys. Res., 74, 6291 (1969).
- Dyson, P. L., J. P. McClure, and W. B. Hanson, J. Geophys. Res., 79, 1497 (1974).
- Evans, D. S., and T. E. Moore, J. Geophys. Res., 84, 6451 (1979).
- Evans, J. V., J. M. Holt, W. L. Oliver and R. H. Wand, J. Geophys. Res., 88, 7769 (1983).
- Fedder, J. A., and P. M. Banks, J. Geophys. Res., 77, 2328 (1972).
- Fejer, B. G., and M. C. Kelley, Rev. Geophys. Space Phys., 18, 401 (1980).
- Foster, J. C., J. Geophys. Res., 89, 855 (1984).
- Foster, J. C., and J. R. Doupnik, J. Geophys. Res., 89, 9107 (1984).
- Foster, J. C., G. S. Stiles, and J. R. Doupnik, J. Geophys. Res., 85, 3453 (1980).
- Francis, S. H., and F. W. Perkins, J. Geophys. Res., 80, 3111 (1975).
- Fremouw, E. J., and H. F. Bates, Radio Sci., 6, 863 (1971).
- Fremouw, E. J., and J. M. Lansinger, J. Geophys. Res., 86, 10087 (1981).
- Fremouw, E. J., C. L. Rino, R. C. Livingston, and M. D. Cousins, Geophys. Res. Lett., 4, 539 (1977).
- Fremouw, E. J., J. A. Secan, and J. M. Lansinger, Radio Sci., 20, 923 (1985).
- Frihagen, J., J. Atmos. Terr. Phys., 31, 81 (1969).
- Frihagen, J., and T. Jacobsen, J. Atmos. Terr. Phys., 33, 519 (1971).

- Frihagen, J., and J. Tröim, NDRE Report No. 38 (1961).
- Gary, S. P., J. Geophys. Res., 89, 179 (1984).
- Gary, S. P., and T. E. Cole, J. Geophys. Res., 88, 10104 (1983).
- Gary, S. P., and M. F. Thomsen, J. Geophys. Res., 87, 73 (1982).
- Gary, S. P., P. A. Berhardt, and T. E. Cole, T. E., J. Geophys. Res., 88, 2103 (1983).
- Goldman, S. R., and J. L. Sperling, J. Geophys. Res., 87, 254 (1982).
- Greenwald, R. A., K. B. Baker, and J. P. Villain, Radio Sci., 18, 1122 (1983).
- Greenwald, R. A., K. B. Baker, R. A. Hutchins, and C. Hanuise, Radio Sci., 20, 63 (1985).
- Gurnett, D. A., and S.-I. Akasofu, J. Geophys. Res., 79, 3197 (1974).
- Gussenhoven, M. S., D. A. Hardy, and N. J. Heinemann, J. Geophys. Res., 88, 5692 (1983).
- Hanson, W. B., S. Sanatani, and T. N. L. Patterson, J. Geophys. Res., 88, 3169 (1983).
- Hanuise, C., Radio Sci., 18, 1093 (1983).
- Hanuise, C., J.-P. Villain, and M. Crochet, Geophys. Res. Lett., 8, 1083 (1981).
- Hanuise, C., R. A. Greenwald, and K. B. Baker, J. Geophys. Res., 90, 9717 (1985).
- Hardy, D. A., J. Geophys. Res., 89, 3883 (1984).
- Hardy, D. A., W. J. Burke, and M. S. Gussenhoven, J. Geophys. Res., 87, 2413 (1982).

- Hargreaves, J. K., C. J. Burns, and S. C. Kirkwood, Radio Sci., 20, 745 (1985).
- Harper, R. W., and Walker, Planet. Space Sci., 25, 197 (1977).
- Heelis, R. A., J. Geophys. Res., 89, 2873 (1984).
- Heelis, R. A., J. K. Lowell, and R. W. Spiro, J. Geophys. Res., 87, 6339 (1982).
- Heelis, R. A., J. F. Vickrey, and N. B. Walker, J. Geophys. Res., 90, 437 (1985).
- Herman, J. R., Spread F and its effects upon radiowave propagation and communication, (ed. P. Newman), Agardograph 95, 567, Technivision, Maidenhead, England, 1966.
- Hill, G. E., J. Atmos. Sci., 20, 492 (1963).
- Hoch, R. J., L. L. Smith, H. B. Liemohn, and J. Murray, J. Geophys. Res., 79, 3859 (1974).
- Holzworth, R. H., and C.-I. Meng, Geophys. Res. Lett., 2, 377 (1975).
- Hones, E. W., Jr., J. R. Asbridge, S. J. Bame, and S. Singer, J. Geophys. Res., 76, 63 (1971).
- Houminer, Z., J. Aarons, and F. Rich, J. Geophys. Res., 86, 9939 (1981).
- Hower, G. L., and A. B. Makhijani, J. Geophys. Res., 74, 3723 (1969).
- Hower, G. L., D. M. Ranz, and C. L. Allison, J. Geophys. Res., 71, 3215 (1966).
- Huba, J. D., J. Geophys. Res., 89, 2931 (1984).
- Huba, J. D., and P. J. Chaturvedi, J. Geophys. Res., 91, 7125 (1986).
- Huba, J. D., and S. T. Zalesak, J. Geophys. Res., 88, 10263 (1983).

- Huba, J. D., S. L. Ossakow, P. Satyanarayana, and P. N. Guzdar,
J. Geophys. Res., 88, 425 (1983).
- Iijima, T., and T. A. Potemra, J. Geophys. Res., 81, 2165 (1976).
- Johnstone, A. D., and J. D. Winningham, J. Geophys. Res., 87, 2321 (1982).
- Jones, T. B., and C. T. Spracklen, J. Atmos. Terr. Phys., 40, 409 (1978).
- Kelley, M. C., J. Geophys. Res., 77, 1327 (1972).
- Kelley, M. C., and P. M. Kintner, Astrophys. J., 220, 339 (1978).
- Kelley, M. C., and F. S. Mozer, J. Geophys. Res., 77, 4158 (1972).
- Kelley, M. C., A. Pedersen, U. V. Fahlson, D. Jones, and D. Kohn,
J. Geophys. Res., 79, 2859 (1974).
- Kelley, M. C., K. D. Baker, J. C. Ulwick, C. L. Rino, and M. J. Baron,
Radio Sci., 15, 491 (1980).
- Kelley, M. C., J. F. Vickrey, C. W. Carlson, and R. Torbert.
J. Geophys. Res., 87, 4469 (1982).
- Kelly, J. D., and J. F. Vickrey, Geophys. Res. Lett., 11, 907 (1984).
- Keskinen, M. J., J. Geophys. Res., 89, 3913 (1984).
- Keskinen, M. J., and S. L. Ossakow, J. Geophys. Res., 86, 6947 (1981).
- Keskinen, M. J., and S. L. Ossakow, J. Geophys. Res., 87, 144 (1982).
- Keskinen, M. J., and S. L. Ossakow, J. Geophys. Res., 88, 474 (1983a).
- Keskinen, M. J., and S. L. Ossakow, Radio Sci., 18, 1077 (1983b).
- Keskinen, M. J., S. L. Ossakow, and B. E. McDonald, Geophys. Res. Lett., 7,
573 (1980).
- Knudsen, W. C., J. Geophys. Res., 79, 1046 (1974).
- Knudsen, W. C., P. M. Banks, J. D. Winningham, and D. M. Klumpar,
J. Geophys. Res., 82, 4784 (1977).

- Kofman, W., and V. B. Wickwar, Geophys. Res. Lett., 11, 919 (1984).
- Köhn, D., and D. E. Page, J. Geophys. Res., 77, 4888 (1972).
- Lassen, K., J. R. Sharber, and J. D. Winningham, J. Geophys. Res., 82, 5031 (1977).
- Lee, M. C., J. Geophys. Res., 89, 7482 (1984).
- Leitinger, R., G. K. Hartmann, W. Degenhardt, A. Hedberg, and P. Tanskanen, J. Atmos. Terr. Phys., 44, 369 (1982).
- Linson, L. M., and D. C. Baxter, Final Report, Contract No. NAS5-24121, Science Applications, Inc., La Jolla, California (1979).
- Linson, L. M., and J. B. Workman, J. Geophys. Res., 75, 3211 (1970).
- Livingston, R. C., C. L. Rino, J. Owen, and R. T. Tsunoda, J. Geophys. Res., 87, 10519 (1982).
- Lizka, L., Nature, 183, 1383 (1959).
- Lizka, L., J. Geophys. Res., 66, 1573 (1961).
- Lizka, L., Arkiv für Geofysik, 4, 227 (1963).
- Lizka, L., Spread F and its effects upon radiowave propagation and communication, (ed. P. Newman), Agardograph 95, 409, Technivision, Maidenhead, England, 1966.
- Lizka, L., and B. Hultqvist, Arkiv för geofysik, 4, 25 (1961).
- Maehlum, B. N., J. Atmos. Terr. Phys., 34, 513 (1972).
- Maude, A. D., and M. A. H. Pramanik, J. Atmos. Terr. Phys., 29, 1311 (1967).
- Maynard, N. C., Geophys. Res. Lett., 5, 617 (1978).
- Maynard, N. C., J. P. Heppner, and A. Egeland, Geophys. Res. Lett., 9, 981 (1982).

- McDaniel, D. R. (compiler), Proc. Secede Final Program Rev., vol. 2,
Contract F30602-72-C-0237, Stanford Research Institute, Menlo Park,
Ca., October 1972.
- McDonald, B. E., S. L. Ossakow, S. T. Zalesak, and N. J. Zabusky,
J. Geophys. Res., 86, 5775 (1981).
- Meek, J. H., J. Geophys. Res., 54, 339 (1949).
- Meng, C.-I., R. H. Holzworth, S.-I. and Akasofu, J. Geophys. Res., 82, 164
(1977).
- Mikkelsen, I. S., Planet. Space Sci., 23, 619 (1975).
- Mikkelsen, I. S., J. Aarons, and E. Martin, J. Atmos. Terr. Phys., 40, 479
(1978).
- Möller, H. G., J. Atmos. Terr. Phys., 36, 1487 (1974).
- Möller, H. G., and A. Tauriainen, J. Atmos. Terr. Phys., 37, 161 (1975).
- Mozer, F. S., J. Geophys. Res., 76, 7595 (1971).
- Mozer, F. S., J. Geophys. Res., 78, 1719 (1973).
- Muldrew, D. B., and J. F. Vickrey, J. Geophys. Res., 87, 8263 (1982).
- Nagy, A. F., R. J. Cicerone, P. B. Hays, K. D. McWatters, J. W. Meriwether,
A. E. Belon, and C. L. Rino, Radio Sci., 9, 315 (1974).
- Nekrasov, Y., A. V. Shirochkov, and I. A. Shumilov, J. Atmos. Terr. Phys.,
44, 769 (1982).
- Oksman, J., and A. Tauriainen, J. Atmos. Terr. Phys., 33, 1727 (1971).
- Oksman, J., and A. Tauriainen, COSPAR Proc., 12, 1978.
- Ossakow, S. L., and P. K. Chaturvedi, J. Geophys. Res., 83, 2085 (1978).
- Ossakow, S. L., and P. K. Chaturvedi, Geophys. Res. Lett., 6, 332 (1979).

- Ossakow, S. L., P. K. Chaturvedi, and J. B. Workman, J. Geophys. Res., 83, 2691 (1978).
- Overman, E. A., II, and N. J. Zabusky, Phys. Rev. Lett., 45, 1693 (1980).
- Perkins, F. W., and J. H. Doles, III, J. Geophys. Res., 80, 211 (1975).
- Perkins, F. W., N. J. Zabusky, and J. H. Doles, III, J. Geophys. Res., 78, 697 (1973).
- Petrie, L. E., Spread F and Its Effects upon Radiowave Propagation and Communications, (ed. P. Newman), 67, Agardograph 95, Technivision, Maidenhead, England, 1966.
- Phelps, A. D. R., and R. C. Sagalyn, J. Geophys. Res., 81, 515 (1976).
- Pike, C. P., J. Geophys. Res., 76, 7745 (1971).
- Pike, C. P., J. Geophys. Res., 77, 6911 (1972).
- Pilkington, G. R., J. W. Munch, H. J. Braun, and H. G. Möller, J. Atmos. Terr. Phys., 37, 337 (1975).
- Reasoner, D. L., and C. R. Chappell, J. Geophys. Res., 78, 2176 (1973).
- Rich, F. J., W. Burke, M. Kelley, and M. Smiddy, M., J. Geophys. Res., 85, 2340 (1980).
- Rino, C. L., Radio Sci., 14, 1135 (1979).
- Rino, C. L., and S. J. Matthews, J. Geophys. Res., 85, 4139 (1980).
- Rino, C. L., and J. Owen, J. Geophys. Res., 85, 2941 (1980).
- Rino, C. L., and J. F. Vickrey, J. Atmos. Terr. Phys., 44, 875 (1982).
- Rino, C. L., V. B. Wickwar, P. M. Banks, S.-I. Akasofu, and E. Rieger, J. Geophys. Res., 79, 4669 (1974).
- Rino, C. L., R. C. Livingston, and S. J. Matthews, Geophys. Res. Lett., 5, 1039 (1978).

- Rino, C. L., R. T. Tsunoda, J. Petriceks, R. C. Livingston, M. C. Kelley,
and K. D. Baker, J. Geophys. Res., 86, 2411 (1981).
- Rino, C. L., R. C. Livingston, R. T. Tsunoda, R. M. Robinson,
J. F. Vickrey, C. Senior, M. D. Cousins, J. Owen, and J. A. Klobuchar,
Radio Sci., 18, 1167 (1983).
- Robinson, R. M., and R. R. Vondrak, J. Geophys. Res., 89, 3951 (1984).
- Robinson, R. M., D. S. Evans, T. A. Potemra, and J. D. Kelly,
Geophys. Res. Lett., 11, 899 (1984).
- Robinson, R. M., R. T. Tsunoda, J. F. Vickrey, and L. Guerin,
J. Geophys. Res., 90, 7533 (1985).
- Robinson, R. M., R. R. Vondrak, K. Miller, T. Dabbs, and D. Hardy,
J. Geophys. Res., 92, 2565 (1987).
- Roble, R. G., and M. H. Rees, Planet. Space Sci., 25, 991 (1977).
- Rodriguez, P., and E. P. Szuszczewicz, J. Geophys. Res., 89, 5575 (1984).
- Rosenberg, N. W., J. Geophys. Res., 76, 6856 (1971).
- Rycroft, M. J., and S. J. Burnell, J. Geophys. Res., 75, 5600 (1970).
- Saflekos, N. A., W. J. Burke, and P. F. Fougere, Radio Sci., 20, 463
(1985).
- Sagalyn, R. C., M. Smiddy, and M. Ahmed, J. Geophys. Res., 79, 4252 (1974).
- Sato, T., Rep. Ionos. Res. Space Res. Jap., 13, 91 (1959).
- Sato, T., and G. F. Rourke, J. Geophys. Res., 69, 4591 (1964).
- Satyanarayana, P., and S. L. Ossakow, J. Geophys. Res., 89, 3019 (1984).
- Satyanarayana, P., J. Chen, and M. J. Keskinen, J. Geophys. Res., 90, 4311
(1985).
- Scannapieco, A. J., and S. L. Ossakow, Geophys. Res. Lett., 3, 451 (1976).

- Scannapieco, A. J., S. L. Ossakow, S. R. Goldman, and J. M. Pierre,
J. Geophys. Res., 81, 6037 (1976).
- Senior, C., J. R. Sharber, O. de la Beaujardiere, R. A. Heelis,
D. S. Evans, J. D. Winningham, M. Sugiura, and W. R. Hoegy,
J. Geophys. Res., 92, 2477 (1987).
- Shiau, J. N., and A. Simon, J. Geophys. Res., 79, 1895 (1974).
- Sica, R. J., M. H. Rees, G. J. Romick, G. Hernandez, and R. G. Roble,
J. Geophys. Res., 91, 3231 (1986).
- Simon, A., Phys. Fluids., 6, 382 (1963).
- Singh, M., P. Rodriguez, and E. P. Szuszczewicz, J. Geophys. Res., 90, 6525
(1985).
- Slater, D. W., L. L. Smith, and E. W. Kleckner, J. Geophys. Res., 85, 531
(1980).
- Smiddy, M., M. C. Kelley, W. Burke, F. Rich, R. Sagalyn, B. Shuman,
R. Hays, and S. Lai, Geophys. Res. Lett., 4, 543 (1977).
- Snyder, A. L., S.-I. Akasofu, and C. P. Pike, Planet. Space Sci., 21, 399
(1973).
- Sojka, J. J., and R. W. Schunk, J. Geophys. Res., 91, 3245 (1986).
- Sojka, J. J., W. J. Raitt, and R. W. Schunk, J. Geophys. Res., 84, 5943
(1979).
- Sojka, J. J., R. W. Schunk, J. V. Evans, J. M. Holt, and R. H. Wand,
J. Geophys. Res., 88, 7783 (1983).
- Sperling, J. L., J. Geophys. Res., 88, 4075 (1983).
- Sperling, J. L., and A. J. Glassman, J. Geophys. Res., 90, 2819 (1985a).
- Sperling, J. L., and A. J. Glassman, J. Geophys. Res., 90, 8507 (1985b).

- Sperling, J. L., J. F. Drake, S. T. Zalesak, and J. D. Huba,
J. Geophys. Res., 89, 10913 (1984).
- Spiro, R. W., R. A. Heelis, and W. B. Hanson, Geophys. Res. Lett., 6, 657
(1979).
- Stoffregen, W., J. Atmos. Terr. Phys., 32, 171 (1970).
- Stuart, G. F., and J. E. Titheridge, J. Atmos. Terr. Phys., 31, 905 (1969).
- Szuszczewicz, E. P., Radio Sci., 21, 351 (1986).
- Tanskanen, P. J., D. A. Hardy, and W. J. Burke, J. Geophys. Res., 86, 1379
(1981).
- Taylor, G. N., J. Atmos. Terr. Phys., 35, 647 (1973).
- Tsunoda, R. T., J. Geophys. Res., 86, 139 (1981).
- Tsunoda, R. T., I. Häggström, A. Pellinen-Wannberg, Å. Steen, and
G. Wannberg, Radio Sci., 20, 762 (1985).
- Tsunoda, R. T., I. Häggström, A. Pellinen-Wannberg, Å. Steen, G. Wannberg,
and J. F. Vickrey, J. Atmos. Terr. Phys., 48, 905 (1986).
- Tulunay, Y. K., O. Demir, and A. Tauriainen, J. Atmos. Terr. Phys., 38, 217
(1976).
- Turunen, T., and J. Oksman, J. Atmos. Terr. Phys., 41, 345 (1979).
- Vickrey, J. F., and M. C. Kelley, J. Geophys. Res., 87, 4461 (1982).
- Vickrey, J. F., and M. C. Kelley, High-latitude Space Plasma Physics, (eds.
B. Hultqvist and T. Hagfors), 95, Plenum Publ. Corp., New York, 1983.
- Vickrey, J. F., C. L. Rino, and T. A. Potemra, Geophys. Res. Lett., 7, 789
(1980).
- Vickrey, J. F., R. R. Vondrak, and S. J. Matthews, J. Geophys. Res., 86, 65
(1981).

- Vickrey, J. F., M. C. Kelley, R. Pfaff, and S. R. Goldman,
J. Geophys. Res., 89, 2955 (1984).
- Vickrey, J. F., R. C. Livingston, N. B. Walker, T. A. Potemra,
 R. A. Heelis, and F. J. Rich, Geophys. Res. Lett., 13, 495 (1986).
- Villain, J. P., R. A. Greenwald, and J. F. Vickrey, Radio Sci., 19, 359
 (1984).
- Villain, J. P., G. Caudal, and C. Hanuise, J. Geophys. Res., 90, 8433
 (1985).
- Villain, J. P., C. Beghin, and C. Hanuise, Ann. Geophys., 4, 61 (1986).
- Volk, H. J., and G. Haerendel, J. Geophys. Res., 76, 4541 (1971).
- Watkins, B. J., Planet. Space Sci., 26, 559 (1978).
- Watkins, B. J., and P. G. Richards, J. Atmos. Terr. Phys., 41, 179 (1979).
- Weber, E. J., and J. Buchau, Geophys. Res. Lett., 8, 125 (1981).
- Weber, E. J., and J. Buchau, The Polar Cusp, (eds. J. A. Holtet and
 A. Egeland), Reidel Publ. Co., 279, 1985.
- Weber, E. J., J. Buchau, J. G. Moore, J. R. Sharber, R. C. Livingston,
 J. D. Winningham, and B. W. Reinisch, J. Geophys. Res., 89, 1683
 (1984).
- Weber, E. J., R. T. Tsunoda, J. Buchau, R. E. Sheehan, D. J. Strickland,
 W. Whiting, and J. G. Moore, J. Geophys. Res., 90, 6497 (1985).
- Weber, E. J., J. A. Klobuchar, J. Buchau, H. C. Carlson, Jr.,
 R. C. Livingston, O. de la Beaujardiere, M. McCready, J. G. Moore,
 G. J. Bishop, J. Geophys. Res., 91, 12121 (1986).
- Wickwar, V. B., J. W. Meriwether, Jr., P. B. Hays, and A. F. Nagy,
J. Geophys. Res., 89, 10987 (1984).

- Wild, J. P., and J. A. Roberts, J. Atmos. Terr. Phys., 8, 55 (1956).
- Winningham J. D., and W. J. Heikkila, J. Geophys. Res., 79, 949 (1974).
- Woodman, R. F., and C. La Hoz, J. Geophys. Res., 81, 5447 (1976).
- Yasuhara, F., S.-I. Akasofu, J. D. Winningham, and W. J. Heikkila,
J. Geophys. Res., 78, 7286 (1973).
- Yevlashina, L. M., and L. S. Yevlashin, J. Atmos. Terr. Phys., 33, 403
(1971).
- Zalesak, S. T., and J. D. Huba, NRL Memo Rept. 5312, Naval Research
Laboratory, Washington, D. C., 1984.
- Zalesak, S. T., S. L. Ossakow, and P. K. Chaturvedi, J. Geophys. Res., 87,
151 (1982).
- Zalesak, S. T., P. K. Chaturvedi, S. L. Ossakow, and J. A. Fedder,
J. Geophys. Res., 90, 4299 (1985).

DISTRIBUTION LIST

DEPARTMENT OF DEFENSE

DEFENSE ADV RSCH PROJ AGENCY
ATTN: R ALEWINE

DEFENSE COMMUNICATIONS AGENCY
ATTN: J DIETZ

DEFENSE COMMUNICATIONS AGENCY
ATTN: A320
ATTN: J HOFF

DEFENSE INTELLIGENCE AGENCY
2 CYS ATTN: RTS-2B

DEFENSE NUCLEAR AGENCY
ATTN: NANF
ATTN: NAWF
ATTN: OPNA
3 CYS ATTN: RAAE
ATTN: A MARDIGUIAN
ATTN: K SCHWARTZ
ATTN: L SCHROCK
ATTN: RAEE
4 CYS ATTN: TITL

DEFENSE NUCLEAR AGENCY
ATTN: TDNM-CF
ATTN: TDTT W SUMMA

DEFENSE TECH INFO CENTER
12CYS ATTN: DD

LAWRENCE LIVERMORE NATIONAL LAB
ATTN: DNA-LL

DEPARTMENT OF THE ARMY

HARRY DIAMOND LABORATORIES
2 CYS ATTN: J BRAND

U S ARMY COMM R&D COMMAND
ATTN: AMSEL-RD-ESA

U S ARMY FOREIGN SCI & TECH CTR
ATTN: DRXST-SD

U S ARMY NUCLEAR & CHEM AGENCY
ATTN: MONA-NU

U S ARMY NUCLEAR EFFECTS LAB
ATTN: ATAA-PL
ATTN: ATAA-TDC
ATTN: ATRC-WCC

U S ARMY STRATEGIC DEFENSE CMD
ATTN: DASD-H-SAV

U S ARMY STRATEGIC DEFENSE COMMAND
ATTN: W DAVIES
ATTN: R BRADSHAW

U S ARMY WHITE SANDS MISSILE RANGE
ATTN: K CUMMINGS

DEPARTMENT OF THE NAVY

NAVAL AIR SYSTEMS COMMAND
ATTN: PMA 271

NAVAL OCEAN SYSTEMS CENTER
ATTN: CODE 54
ATTN: J FERGUSON

NAVAL RESEARCH LABORATORY
ATTN: J GOODMAN
ATTN: S OSSAKOW
ATTN: J DAVIS
ATTN: B RIPIN
ATTN: P RODRIGUEZ
ATTN: J HUBA

NAVAL UNDERWATER SYSTEMS CENTER
ATTN: J KATAN

SPACE & NAVAL WARFARE SYSTEMS CMD
ATTN: T HUGHES
ATTN: PD 50TD
ATTN: B KRUGER
ATTN: G BRUNHART
ATTN: S KEARNEY
ATTN: F W DIEDERICH

DEPARTMENT OF THE AIR FORCE

AIR FORCE GEOPHYSICS LABORATORY
ATTN: J RAMUSSEN
ATTN: J BUCHAU
ATTN: LS
ATTN: R O'NIEL
ATTN: H GARDINER
ATTN: K CHAMPION

AIR FORCE SPACE DIVISION
ATTN: CWF
ATTN: YA
ATTN: YG
2 CYS ATTN: YN

AIR FORCE TECH APPLICATIONS CTR
ATTN: TN

AIR FORCE WEAPONS LABORATORY
ATTN: NTN
ATTN: SUL

AIR FORCE WRIGHT AERONAUTICAL LAB/AAAD
ATTN: W HUNT

AIR UNIVERSITY LIBRARY
ATTN: AUL-LSE

STRATEGIC AIR COMMAND/XPQ
ATTN: XPQ

DEPARTMENT OF ENERGY

LOS ALAMOS NATIONAL LABORATORY
ATTN: D SAPPENFIELD
ATTN: D SIMONS

DNA-TR-88-44 (DL CONTINUED)

ATTN: D WINSKE
ATTN: J WOLCOTT
ATTN: J ZINN
ATTN: R JEFFRIES
ATTN: R W WHITAKER
ATTN: T KUNKLE

SANDIA NATIONAL LABORATORIES
ATTN: D HARTLEY

SANDIA NATIONAL LABORATORIES
ATTN: A D THORNBROUGH
ATTN: R BACKSTROM
ATTN: D DAHLGREN
ATTN: T P WRIGHT
ATTN: W D BROWN
ATTN: SPACE PROJECT DIV
ATTN: TECH LIB 3141

OTHER GOVERNMENT

CENTRAL INTELLIGENCE AGENCY
ATTN: OSWR/NED
ATTN: L BERG

DEPARTMENT OF DEFENSE CONTRACTORS

AEROSPACE CORP
ATTN: A LIGHTLY
ATTN: C RICE
ATTN: G LIGHT
ATTN: M ROLENZ

AUSTIN RESEARCH ASSOCIATES
ATTN: J THOMPSON

BDM CORP
ATTN: A VITELLO
ATTN: L JACOBS

BERKELEY RSCH ASSOCIATES, INC
ATTN: C PRETTIE
ATTN: J WORKMAN
ATTN: S BRECHT

CHARLES STARK DRAPER LAB, INC
ATTN: A TETEWSKI

COMMUNICATIONS SATELLITE CORP
ATTN: G HYDE

EOS TECHNOLOGIES, INC
ATTN: B GABBARD
ATTN: W LELEVIER

GRUMMAN AEROSPACE CORP
ATTN: J DIGLIO

GTE GOVERNMENT SYSTEMS CORPORATION
ATTN: W I THOMPSON

HARRIS CORPORATION
ATTN: E KNICK

HSS, INC
ATTN: D HANSEN

IIT RESEARCH INSTITUTE
ATTN: A VALENTINO

INSTITUTE FOR DEFENSE ANALYSES
ATTN: E BAUER
ATTN: H WOLFHARD

JOHNS HOPKINS UNIVERSITY
ATTN: C MENG
ATTN: J D PHILLIPS
ATTN: R STOKES
ATTN: T EVANS

KAMAN SCIENCES CORP
ATTN: E CONRAD

KAMAN SCIENCES CORPORATION
ATTN: DASIA

KAMAN TEMPO
ATTN: B GAMBILL
ATTN: DASIA
ATTN: R RUTHERFORD
ATTN: W MCNAMARA

LOCKHEED MISSILES & SPACE CO, INC
ATTN: J HENLEY
ATTN: J KUMER
ATTN: R SEARS

LOCKHEED MISSILES & SPACE CO, INC
2 CYS ATTN: D CHURCHILL
ATTN: D KREJCI

M I T LINCOLN LAB
ATTN: D TOWLE
ATTN: I KUPIEC

MARTIN MARIETTA DENVER AEROSPACE
ATTN: H VON STRUVE III

MAXIM TECHNOLOGIES, INC
ATTN: J SO

MCDONNELL DOUGLAS CORP
ATTN: T CRANOR

MCDONNELL DOUGLAS CORP
ATTN: R HALPRIN

METATECH CORPORATION
ATTN: R SCHAEFER
ATTN: W RADASKY

METEOR COMMUNICATIONS CORP
ATTN: R LEADER

MISSION RESEARCH CORP
ATTN: B R MILNER
ATTN: C LAUER
ATTN: D ARCHER
ATTN: D KNEPP
ATTN: F FAJEN
ATTN: F GUIGLIANO
ATTN: G MCCARTOR
ATTN: K COSNER

ATTN: M FIRESTONE
ATTN: R BIGONI
ATTN: R BOGUSCH
ATTN: R DANA
ATTN: R HENDRICK
ATTN: R KILB
ATTN: S GUTSCHE
ATTN: TECH LIBRARY

MITRE CORPORATION
ATTN: C CALLAHAN
ATTN: D RAMPTON
ATTN: M R DRESP
ATTN: R DRESP

MITRE CORPORATION
ATTN: J WHEELER
ATTN: M HORROCKS
ATTN: R C PESCI
ATTN: W FOSTER

NORTHWEST RESEARCH ASSOC, INC
ATTN: E FREMOUW

PACIFIC-SIERRA RESEARCH CORP
ATTN: E FIELD JR
ATTN: F THOMAS
ATTN: H BRODE

PHOTOMETRICS, INC
ATTN: I L KOFSKY

PHYSICAL RESEARCH INC
ATTN: W. SHIH

PHYSICAL RESEARCH INC
ATTN: H FITZ
ATTN: J JORDANO

PHYSICAL RESEARCH INC
ATTN: P LUNN

PHYSICAL RESEARCH, INC
ATTN: R DELIBERIS
ATTN: T STEPHENS

PHYSICAL RESEARCH, INC
ATTN: J DEVORE
ATTN: J THOMPSON
ATTN: W SCHLUETER

R & D ASSOCIATES
ATTN: C GREIFINGER
ATTN: F GILMORE
ATTN: G HOYT
ATTN: M GANTSWEG
ATTN: M GROVER
ATTN: R TURCO

R & D ASSOCIATES
ATTN: G GANONG

RAND CORP
ATTN: B BENNETT

SCIENCE APPLICATIONS INTL CORP
ATTN: C SMITH
ATTN: D HAMLIN
ATTN: D SACHS
ATTN: E STRAKER
ATTN: L LINSON

SCIENCE APPLICATIONS INTL CORP
ATTN: R LEADABRAND

SCIENCE APPLICATIONS INTL CORP
ATTN: J COCKAYNE

SCIENCE APPLICATIONS INTL CORP
ATTN: D TELAGE
ATTN: M CROSS

SRI INTERNATIONAL
ATTN: D MCDANIEL
2 CYS ATTN: R TSUNODA
ATTN: W CHESNUT
ATTN: W JAYE

TELECOMMUNICATION SCI ASSOCIATES
ATTN: R BUCKNER

TELECOMMUNICATION SCI ASSOCIATES, INC
ATTN: D MIDDLESTEAD

TOYON RESEARCH CORP
ATTN: J GARBARINO
ATTN: J ISE

TRW INC
ATTN: D GRYBOS
ATTN: R PLEBUCH
ATTN: H CULVER

TRW SYSTEMS
ATTN: D M LAYTON

UTAH STATE UNIVERSITY
ATTN: A STEED
ATTN: D BURT
ATTN: K BAKER
ATTN: L JENSEN

VISIDYNE, INC
ATTN: J CARPENTER

FOREIGN

FOA 2
ATTN: B SJOHOLM

FOA 3
ATTN: T KARLSSON